Online ISSN 2716-9650
Print ISSN 2676-5837

Volume 2, Sept. 30, 2020

Journal of Composites and Compounds

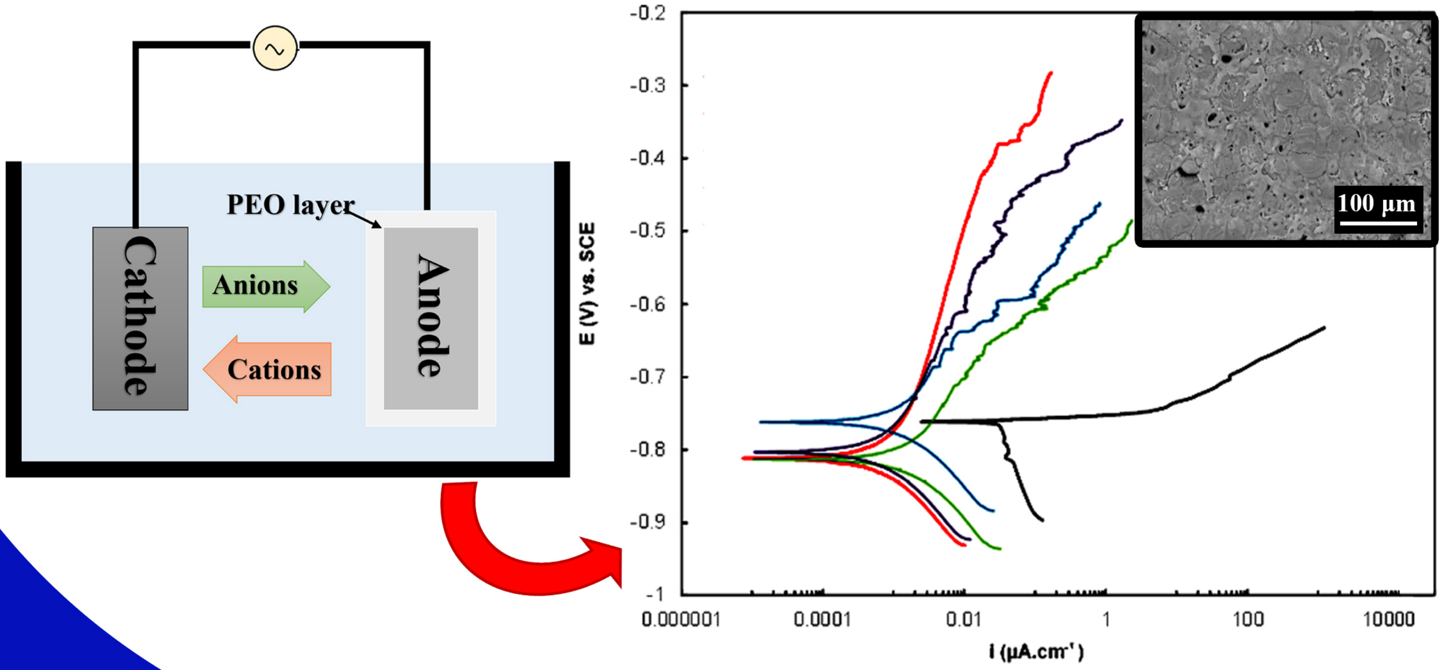

Editor in Chief: F. Sharifianjazi

www.JOURCC.com

Journal of
Composites and Compounds

Online ISSN 2716-9650
Print ISSN 2676-5837
Sept. 30, 2020
Volume 2
No. 4

Available online at www.jourcc.com

📍 **Janatabad St., Tehran, Iran**

☎ **+982144437782**

Journal of
Composites and Compounds

Online ISSN 2716-9650
Print ISSN 2676-5837
Sept. 30, 2020
Volume 2
No. 4

Table of contents

Available online at www.jourcc.com

Janatabad St., Tehran, Iran
+982144437782

Journal of Composites and Compounds 2 (2020) 110-114

Available online at www.jourcc.com

Journal homepage: www.JOURCC.com

Journal of Composites and Compounds

Synthesis and characterization of the novel 80S bioactive glass: bioactivity, biocompatibility, cytotoxicity

Ameneh Bakhtiari[a], Amir Cheshmi[b], Maryam Naeimi[c], Sobhan Mohammadi Fathabad[d], Maryam Aliasghari[e], Amir Modarresi Chahardehi[f]*, Sahar Hassani[g], Vahideh Elhami[h]

[a]Department of Biology, Shahid Chamran University, Ahvaz, Iran
[b] Department of Materials Engineering, Babol Noshirvani University of Technology, Shariati Avenue, Babol, Iran
[c] School of Nursing and Midwifery, Tehran University of Medical Science, Tehran, Iran
[d] Department of Engineering and High-Tech, Iran University of Industries and Mines, Tehran, Iran
[e] Young Researchers and Elite Club, Yadegar-e-Imam Khomeini (RAH) Shahr-e-Rey Branch, Islamic Azad University, Tehran, Iran
[f] Integrative Medicine Cluster, Advanced Medical and Dental Institute, Universiti Sains Malaysia, Bertam, 13200, Kepala Batas, Penang, Malaysia
[g] Department of Cellular and Molecular Biology, Facaulty of Advanced Science and Technology, Tehran Medical Sciences, Islamic Azad University, Tehran, Iran
[h] Sustainable Process Technology Group, Faculty of Science and Technology, University of Twente, Drienerlolaan 5, Enschede 7522 NB, The Netherlands

ABSTRACT

In this research, the 80S bioactive glass with different Ca/P ratios was prepared by the sol-gel route. Scanning electron microscopy (SEM), transmission electron microscopy (TEM), energy dispersive spectroscopy (EDS), X-ray diffraction (XRD), and Fourier transforms infrared spectroscopy (FTIR) were used to study the apatite structure and shape. According to the results, the $78SiO_2–17P_2O_5–5CaO$ bioglass showed a higher rate of crystalline hydroxyapatite (HA) on its surface in comparison with the other bioglasses. After 3 days of immersion in the SBF solution, spherical apatite was formed on the $78SiO_2–17P_2O_5–5CaO$ surface, which demonstrated high bioactivity. A statistically significant promotion in proliferation and differentiation of G292 osteoblastic cells was also observed. Regarding its optimal cell viability and bioactivity, the $78SiO_2–17P_2O_5–5CaO$ bioactive glass could be offered as a promising candidate for bone tissue applications.

ARTICLE INFORMATION

Article history:
Received 25 August 2020
Received in revised form 09 September 2020
Accepted 14 September 2020

Keywords:
Bioactive glass
80S
Ca/P ratio
Hydroxyapatite

1. Introduction

As a result of bone infections, cancer removal, an injury, or other disease, millions of people suffer from bone failure or loss annually. Bone is able to repair itself when damages are minor, however, in the case of pathological fractures or massive defects, it fails to regenerate [1, 2]. In these cases, most common therapy techniques are permanent implants or implantation of bone grafts. The main drawbacks of the commonly applied methods in bone surgery include corrosion and cytotoxicity of metallic objects, shortage of donors, wearing of synthetic materials, and risk of infection in transplantation cases [3-6].

Glass materials play a significant role in permanent and biodegradable implants [7, 8]. Due to their ability to form HA as the main mineral of bone, BGs are suitable materials to be used for bone regeneration [9, 10]. They also can create a strong bond with both soft tissues and bone, and hence their osteoconductivity has been proven [11-13]. BGs are particularly advantageous for repair and replacement of damaged bone in tissue engineering, owing to their high bioactivity and biocompatibility [14, 15].

BGs mainly contain P_2O_5, SiO_2, and CaO enabling a HA layer formation on their surfaces. This layer improves the binding of BGs with bones. SiO_2 is an important network forming constituent in the glass structures [16]. Furthermore, it is able to promote the cell functions by releasing Si ions into cell culture media, and nucleation of calcium phosphate phase is facilitated by P_2O_5 on the glass surface [5, 6].

Since 1991 when a sol-gel method was developed for the synthesis of bioactive glasses, various compositions of glass samples have been produced by this technique at low temperatures [17-19]. Various bioactive compositions can be prepared to achieve great degradation/resorption behavior and bone-bonding rates because of the high porosity and surface area of the prepared sol-gel glasses_[20-22]. Using the sol-gel processing routes for the production of BGs has been suggested by previous investigations and it has been reported that the production of novel BGs with a variety of chemical compositions is possible [11, 23, 24].

Lin et al. [20] prepared $80SiO_2–15CaO–5P_2O_5$ glass powders by the

---

* Corresponding author: Amir Modarresi Chahardehi; E-mail: amirmch@gmail.com

https://doi.org/10.29252/jcc.2.3.1

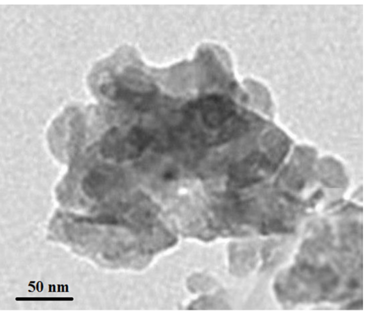

Fig. 1. TEM image the powders after the preparation by the sol-gel route.

sol-gel method. They found that mixing phosphoric acid (PA) with the glass powders exhibited positive effects on the decrease of the dentin penetration and occlusion of the dentinal tubule. Mixing 80S-BG with appropriate PA demonstrated good operability and short reaction time, which makes it feasible to occlude dentinal tubules.

This research aims to prepare 80S BGs with different Ca/P ratios via a sol-gel method. Subsequently, the formation of the hydroxyapatite on the surfaces of the bioactive glass is evaluated using the XRD, FTIR, SEM, and EDX analyses. The potential of the samples in cell proliferation is also studied.

2. Materials and Methods

2.1. Materials

To synthesize the bioactive glasses, calcium nitrate tetrahydrate ($Ca(NO_3)_2 \cdot 4\ H_2O$), Triethyl phosphate (TEP, $(C_2H_5)_3PO_4$), and Tetraethyl orthosilicate (TEOS, $Si(OCH_2CH_3)_4$) with high analytical grades were used. All materials were obtained from Merck Company.

2.2. Synthesis of bioactive glass

The composition of the studied 80S-BGs were 78% SiO_2-17% CaO-5%P_2O_5 (BG-5P), 78% SiO_2-16% CaO-6%P_2O_5 (BG-6P), and 78% SiO_2-18% CaO-4%P_2O_5 (BG-4P) in mol.%. To synthesize the samples, TEP, $Ca(NO_3)_2.4H_2O$, and TEOS were dissolved at room temperature. TEOS was first mixed with nitric acid to obtain a diluted and clear solution. Under constant stirring, calcium nitrate and TEP were then added to the solution. The addition of reagents was carried out sequentially and the time for the complete reaction of each reagent was 40 min. To form the gel, the mixture was stored at room temperature for 9 days in closed containers. Drying of the formed gel was conducted in two stages at 80 °C for 72 h and 130 °C for 24 h. In order to eliminate residual nitrate and all organic substances, the dried material was heated to 750 °C for 2 h.

2.3. Bioactive glass Characterizations

2.3.1. TEM analysis

One of the applicable tools for the analysis of the nanomaterial microstructure is TEM. In this research, to study the obtained glass particles, TEM (CM200-FEG-Philips) with the acceleration voltage of 200 kV was employed. To observe the glass particles, the particles were deposited on Cu support grids from a dilute suspension in ethanol.

2.3.2. XRD analysis

The determination of the formed phases in BG and HA structures was carried out by X-ray diffraction (INEL Equinox 3000) in 2θ between 20° to 90° using the CuKα radiation. The characteristics of the analysis were tube electric current=30 mA, tube voltage=40 kV, scanning speed = 2°/min, and wavelength λ=1.540510 Å.

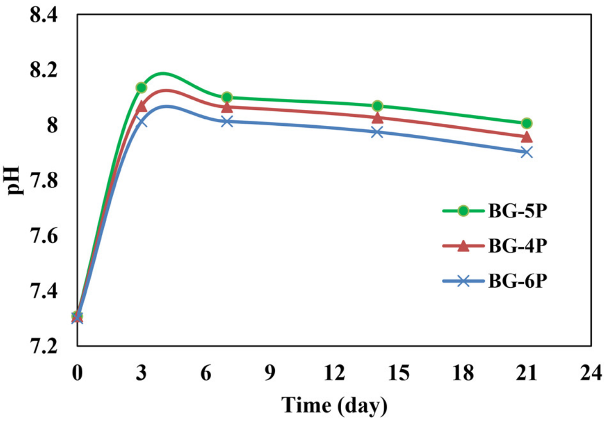

Fig. 2. Change of pH during 21 days of soaking in SBF.

2.3.3. FTIR analysis

To evaluate the formation of hydroxyapatite, FTIR spectrometer (Bomem MB 100) was employed to determine the functional groups present in glass powders. The powders were blended with potassium bromide (KBr) while the blending ration was 1:9. Using a hand press, discs with the diameters less than 6 mm were produced from the blended powders. Recording of FTIR wave numbers was performed in the range of 4000 to 400 cm^{-1}.

2.3.4. MTT assay

To study the biocompatibility of BGs, the proliferation of G292 osteoblastic cells on the samples was studied by 3-(4, 5-dimethylthiazol-2-yl)-2, 5-diphenyltetrazolium bromide (MMT) assay. The cell line was obtained from Pasteur Institute (the National Cell Bank of Iran). Cell culture was performed under standard culturing conditions and the cultured cells were maintained in 90% moisture for 24 h at 37 °C. A 96-well plate was used for seeding the cells. The cultured osteoblastic cells were seeded at a density of 6×10^3 cells/well and maintained for 1 day for attachment. The related absorbance measurements were carried out at a wavelength of 570 nm with a multi-well microplate reader (BioTek Instruments). Three readings were done for each specimen.

2.3.5. Simulated body fluid (SBF)

One of the easiest methods for the biomineralization study of BGs is the SBF test. It is also quick and cost-effective. This test can appropriately simulate the osteo-production conditions, which exist in osseous tissue. Also, it is suitable for bioactivity investigation of materials and the contributing bone-bonding mechanisms [5]. The ionic concentration and composition of SBF are similar to human body plasma (Na_2HPO_4, Na_2SO_4, $CaCl_2$, HCl, $MgCl_2$, KCl, $NaHCO_3$, NaCl, and $(CH_2OH)_3(CNH)_2$ as the buffering agent). The prepared solution buffered at 37 ˚C with 1 N HCl solution and TRIS (trishydroxymethylaminomethane) at pH = 7.25. The 80S bioactive glass powders were immersed in the prepared SBF at 37˚C for 3, 7, and 14 days. The concentration of the immersed powders was 1.5 mg of powder per milliliter of the solution. The powders were filtered and dried after the determined time.

2.3.6. SEM-EDS

SEM and EDS were employed for the evaluation of the composition and morphology of the bioactive glasses before and after the bioactivity tests. The reaction between the solution and bioglass powders resulting in the surface evolution was studied. The acceleration voltage was 15 kV and the samples were gold-coated before the analysis.

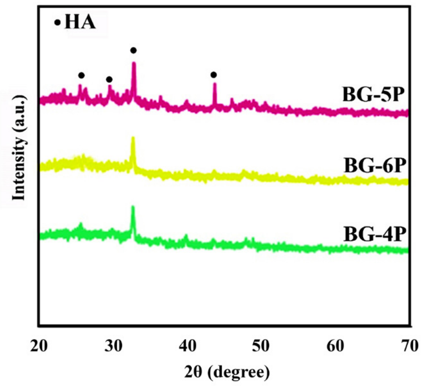

Fig. 3. XRD patterns of BGs after soaking in SBF for 21 days.

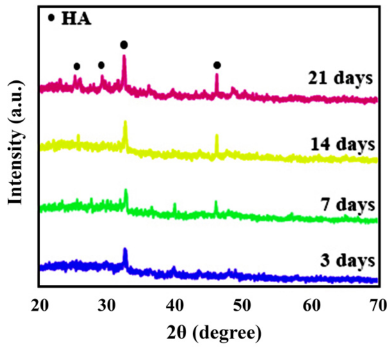

Fig. 4. XRD patterns of BG-5P after soaking in SBF for 3, 7, 14, and 21 days.

3. Result and discussion

3.1. TEM analysis of as-prepared samples

Fig. 1 depicts the TEM image of the as-prepared powder of BG-5P. The TEM image shows the formation of bioactive glass nanoparticles with the irregular-round shape. The diameter of the nanoparticles is between 40 to 60 nm.

3.2. pH analysis

Fig. 2 illustrates the changes in the pH value of SBF during 21 days of soaking. According to the literature, the pH evaluation of the SBF solution after the immersion can determine the process of HA formation. A similar trend was observed for all the samples. As seen, a remarkable increase in pH occurred for the BG-5P after 7 days. It indicated that cationic ions dissolved in the solution from the surface of BG. The silica network of the glass was attacked by the solution at high pH. After 7 days of immersion, the pH started to decrease revealing the absorption of calcium and phosphate ions from SBF. Therefore, it demonstrates the increase in hydroxyapatite formation on the surface of BGs.

3.3. XRD analysis

After 21 days of soaking, the structure of BGs was studied by XRD and the results are presented in Fig. 3. As illustrated, the peaks attributed to the presence of crystalline HA were observed. The diffraction peaks at 2θ of 32° are related to the (211) plane of crystalline hydroxyapatite confirming the formation of HA on the samples after 21 days of soaking in SBF. Moreover, the intensity of this peak is higher in BG-5P in comparison with other samples indicating the higher tendency of BG-5P to form hydroxyapatite on the glass surface. This might be due to the Ca/P ration. In this bioglass, this ratio is 1.7, which is close to the Ca to P ratio in the structure of human bone. The similar intensity was observed for BG-4P and BG-6P. Fig. 4 demonstrates the XRD patterns of BG-5P after soaking in SBF for 3, 7, 14, and 21 days of immersion in the SBF solution. As seen, the intensity of the peaks related to the formation of crystalline HA increased with the soaking time showing that more hydroxyapatite crystals were formed on the samples' surface.

3.4. FTIR analysis

Figs. 5 and 6 illustrate the FTIR spectra of the bioactive glasses after 14 days of immersion and Fig. 5 depicts the FTIR spectra of BG-5P during 14 days. As shown, two peaks appeared at 1455 and 870 cm^{-1} after 3 days. These peaks are related to carbonate (C–O stretching) groups. The spectra of BG-4P, BG-5P, and BG-6P showed Si-O bending vibration band at 476 cm^{-1}, Si-O symmetric stretching band at 798 cm^{-1}, Si-O-Si asymmetric stretching band at 1000–1250 cm^{-1}, C-O group asymmetric bending vibration band at 874 cm$^{-1,}$ and C=O asymmetric stretching bands at 1652 cm^{-1}. Peaks appeared at 568 and 602 cm^{-1} show the bending vibrations of P–O bonds related to the crystalline hydroxyapatite in all glass samples. The wavenumbers of 1056, 605, and 565 cm^{-1} reveal P–O bending vibrations. Amorphous hydroxyapatite is presented by the broad bands around 1056 cm^{-1} attributed to P–O bending vibrations. The obtained results exhibit the HA growth on the surfaces of the bioactive glasses. The intensity of the peaks is higher in BG-5P revealing the higher amount of HA formation on the surface of the glass. The spectra obtained from the glass in Fig. 6 exhibits that the amount of HA increased by increasing the soaking time.

3.5. Morphology of HA

Fig. 7 illustrates SEM micrographs of the bioglass samples after 21 days of immersion. Full coverage of the surfaces with HA crystals can be observed for all the samples after 21 days. The formation of HA on the bioglasses was also confirmed by the FTIR and XRD analyses. Fig. 7a shows the irregular shape of HA phase, while the hydroxyapatite crystals on BG-5P had both irregular and spherical shapes. The HA layer on BG-6P has mostly spherical shapes. The HA crystals show smaller size and

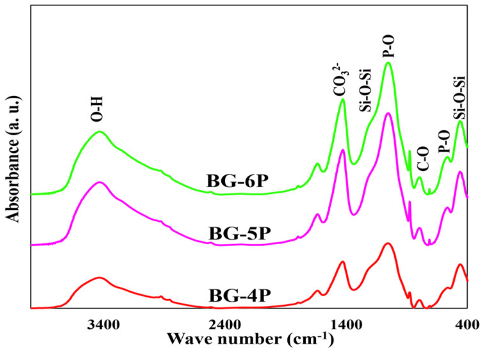

Fig. 5. FTIR spectra for bioactive glass powders after immersion in SBF.

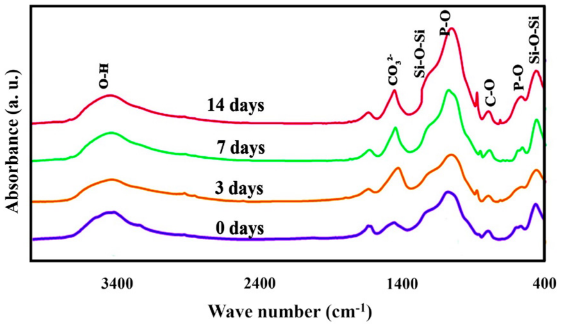

Fig. 6. FTIR spectra of BG-5P after immersion in SBF.

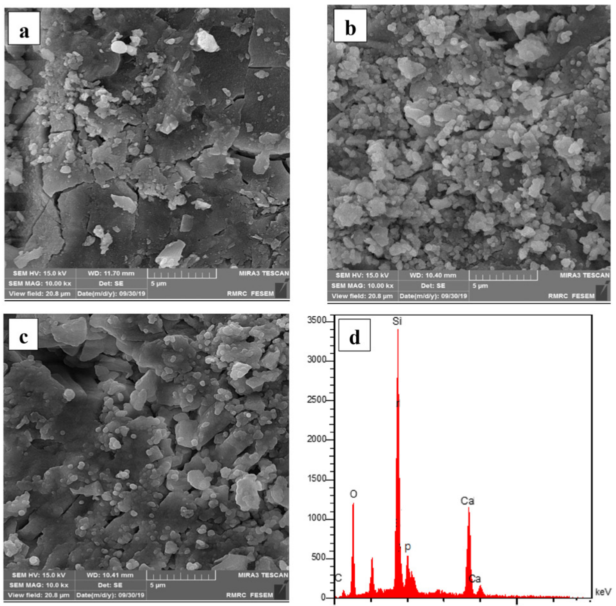

Fig. 7. FSEM images of the glass samples after immersion for 21 days; a) BG-4P, b) BG-5P, c) BG-6P, and d) EDX analysis of BG-5P.

higher dispersity compared to other samples.

EDX analysis of BG-5P after immersion in SBF for 21 days is demonstrated in Fig. 7d. It is confirmed that hydroxyapatite has been successfully formed on the surface of BG-5P.

3.6. Cell viability

Fig. 8 shows the results of the viability test during 7 days. The results indicated that not only the bioactive glass samples were not toxic but also enhanced the cell growth. The cell growth increases by the culturing time for all the samples. However, the BG-5P exhibited higher cell growth compared to the other BGs. This could be due to the optimal Ca/P the sample close to the ratio of human bone. Various biological processes, such as cellular chemotaxis, apoptosis, and differentiation are regulated by extracellular calcium and a calcium-sensing receptor (CaSR). Several studies have indicated that the stimulation of collagen synthesis and proliferation is mostly related to Si contact. Thus, it could be assumed that Si plays a significant role in stimulating angiogenesis, while Ca just helps this process [25].

4. Conclusions

In this research, 80S bioactive glasses with different Ca/P ratios were synthesized using the sol-gel route. The formation of the hydroxyapatite layer was confirmed by the FTIR and XRD analyses after soaking in SBF for all the samples. The results showed that the HA formation rate of BG-5P was higher in comparison with the other two samples. This might be due to the optimum Ca to P ratio close to the Ca to P ratio in human bone composition. The SEM images illustrated the formation of the hydroxyapatite layer on the surfaces of all bioglass samples after immersion for 21 days. The results showed a denser layer with smaller size crystals for BG-5P. Significant cell growth was observed in the MTT in vitro test, while the highest cell viability was related to BG-5P. The results offer this bioactive glass as a promising material for repairing bone defects.

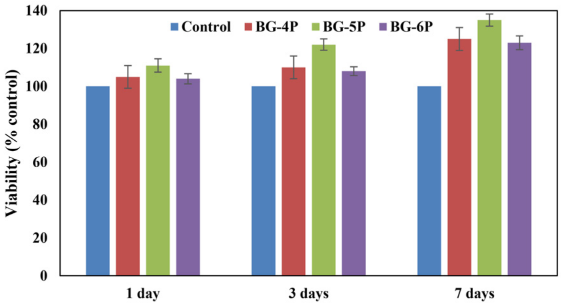

Fig. 8. Cell viability of the bioactive glasses during 7 days.

REFERENCES

[1] L. Bazli, H. Nargesi khoramabadi, A. Modarresi Chahardehi, H. Arsad, B. Malekpouri, M. Asgari Jazi, N. Azizabadi, Factors influencing the failure of dental implants: A Systematic Review, Composites and Compounds 2(1) (2020).

[2] A. Esmaeilkhanian, F. Sharifianjazi, A. Abouchenari, A. Rouhani, N. Parvin, M. Irani, Synthesis and characterization of natural nano-hydroxyapatite derived from turkey femur-bone waste, Applied biochemistry and biotechnology 189(3) (2019) 919-932.

[3] A. Chlanda, P. Oberbek, M. Heljak, E. Kijeńska-Gawrońska, T. Bolek, M. Gloc, Ł. John, M. Janeta, M.J. Woźniak, Fabrication, multi-scale characterization and in-vitro evaluation of porous hybrid bioactive glass polymer-coated scaffolds for bone tissue engineering, Materials Science and Engineering: C 94 (2019) 516-523.

[4] E. Sharifi Sedeh, S. Mirdamadi, F. Sharifianjazi, M. Tahriri, Synthesis and evaluation of mechanical and biological properties of scaffold prepared from Ti and Mg with different volume percent, Synthesis and Reactivity in Inorganic, Metal-Organic, and Nano-Metal Chemistry 45(7) (2015) 1087-1091.

[5] S. Rahimi, F. SharifianJazi, A. Esmaeilkhanian, M. Moradi, A.H.S. Samghabadi, Effect of SiO2 content on Y-TZP/Al_2O_3 ceramic-nanocomposite properties as potential dental applications, Ceramics International (2020).

[6] S. Nasibi, K. Alimohammadi, L. Bazli, S. Eskandarinezhad, A. Mohammadi, N. Sheysi, TZNT alloy for surgical implant applications: A Systematic Review, Journal of Composites and Compounds 2(3) (2020) 61-67.

[7] L. Bazli, B. Eftekhari Yekta, A. Khavandi, Preparation and Characterization of Sn-Containing Glasses for Brachytherapy Applications, Transactions of the Indian Ceramic Society 76(4) (2017) 242-246.

[8] F. Sharifianjazi, A.H. Pakseresht, M.S. Asl, A. Esmaeilkhanian, H.W. Jang, M. Shokouhimehr, Hydroxyapatite consolidated by zirconia: applications for dental implant, Journal of Composites and Compounds 2(1) (2020) 26-34.

[9] Z. Goudarzi, A. Ijadi, A. Bakhriari, S. Eskandarinezhad, N. Azizabadi, M.A. Jazi, Sr-doped bioactive glasses for biological applications, Journal of Composites and Compounds 2(3) (2020) 105-109.

[10] J. Daraei, Production and characterization of PCL (Polycaprolactone) coated TCP/nanoBG composite scaffolds by sponge foam method for orthopedic applications, Journal of Composites and Compounds 2(1) (2020) 45-50.

[11] Z. Goudarzi, N. Parvin, F. Sharifianjazi, Formation of hydroxyapatite on surface of SiO_2– P_2O_5–CaO–SrO–ZnO bioactive glass synthesized through sol-gel route, Ceramics International 45(15) (2019) 19323-19330.

[12] F. Sharifianjazi, N. Parvin, M. Tahriri, Formation of apatite nano-needles on novel gel derived SiO_2-P_2O_5-CaO-SrO-Ag_2O bioactive glasses, Ceramics International 43(17) (2017) 15214-15220.

[13] K. Zhang, Q. Van Le, Bioactive glass coated zirconia for dental implants: a review, Journal of Composites and Compounds 2(1) (2020) 10-17.

[14] F. Sharifianjazi, N. Parvin, M. Tahriri, Synthesis and characteristics of sol-gel bioactive SiO_2-P_2O_5-CaO-Ag_2O glasses, Journal of Non-Crystalline Solids 476 (2017) 108-113.

[15] M.S.N. Shahrbabak, F. Sharifianjazi, D. Rahban, A. Salimi, A comparative investigation on bioactivity and antibacterial properties of sol-gel derived 58S bioactive glass substituted by Ag and Zn, Silicon 11(6) (2019) 2741-2751.

[16] F. Sharifianjazi, M. Moradi, A. Abouchenari, A.H. Pakseresht, A. Esmaeilkhanian, M. Shokouhimehr, M.S. Asl, Effects of Sr and Mg dopants on biological and mechanical properties of SiO_2–CaO–P_2O_5 bioactive glass, Ceramics International (2020).

[17] F. Sharifianjazi, A.H. Pakseresht, M. Shahedi Asl, A. Esmaeilkhanian, H. Nargesi khoramabadi, H.W. Jang, M. Shokouhimehr, Hydroxyapatite Consolidated by Zirconia: Applications for Dental Implant, Composites and Compounds 2(1) (2020).

[18] A. Moghanian, A. Ghorbanoghli, M. Kazem-Rostami, A. Pazhouheshgar, E. Salari, M. Saghafi Yazdi, T. Alimardani, H. Jahani, F. Sharifian Jazi, M. Tahriri, Novel antibacterial Cu/Mg-substituted 58S-bioglass: Synthesis, characterization and investigation of in vitro bioactivity, International Journal of Applied Glass Science (2019) 1-14.

[19] L. Bazli, M. Siavashi, A. Shiravi, A Review of Carbon nanotube/TiO_2 Composite prepared via Sol-Gel method, Journal of Composites and Compounds 1(1) (2019) 1-12.

[20] W.-T. Lin, J.-C. Chen, Y.-C. Hsiao, C.-J. Shih, Re-crystallization of silica-based calcium phosphate glass prepared by sol–gel technique, Ceramics International 43(16) (2017) 13388-13393.

[21] J.R. Jones, Reprint of: Review of bioactive glass: From Hench to hybrids, Acta Biomaterialia 23 (2015) S53-S82.

[22] J. Pawlik, M. Widziołek, K. Cholewa-Kowalska, M. Łączka, A.M. Osyczka, New sol-gel bioactive glass and titania composites with enhanced physico-chemical and biological properties, Journal of Biomedical Materials Research Part A 102(7) (2014) 2383-2394.

[23] J.P. Fan, P. Kalia, L. Di Silvio, J. Huang, In vitro response of human osteoblasts to multi-step sol–gel derived bioactive glass nanoparticles for bone tissue engineering, Materials Science and Engineering: C 36 (2014) 206-214.

[24] R.C. Bielby, I.S. Christodoulou, R.S. Pryce, W.J.P. Radford, L.L. Hench, J.M. Polak, Time- and Concentration-Dependent Effects of Dissolution Products of 58S Sol–Gel Bioactive Glass on Proliferation and Differentiation of Murine and Human Osteoblasts, Tissue Engineering 10(7-8) (2004) 1018-1026.

[25] C. Mao, X. Chen, G. Miao, C. Lin, Angiogenesis stimulated by novel nanoscale bioactive glasses, Biomedical materials 10(2) (2015) 025005.

Journal of Composites and Compounds 2 (2020) 115-122

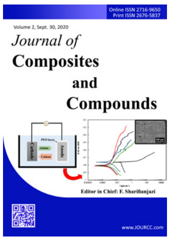

Available online at www.jourcc.com

Journal homepage: www.JOURCC.com

Journal of Composites and Compounds

Investigation of aluminum oxide coatings created by electrolytic plasma method in different potential regimes

Mahsa Amiri[a], Saman Padervand[a], Vahid Tavakoli Targhi[a], Seyed Mohammad Mousavi khoei[a]*

[a] Material and Metallurgical Engineering Department, Amirkabir University of Technology, Hafez Street, Tehran, Iran

ABSTRACT

One of the most important coating methods on aluminum surfaces is the electrolytic plasma method. The main objective of the present study is to investigate the potential of aluminum oxide coatings created by electrolytic plasma method. Aluminum series 2 and the electrolyte of sodium silicate, sodium tetraphosphate, sodium aluminate, and potassium hydroxide were used. The results showed that the appropriate voltage to achieve uniform coating with ideal thickness and morphology is 500 V. Adding sodium silicate to the electrolyte solution will create porosity and non-adhesion to the substrate. On the other hand, the use of tetra sodium pyrophosphate increases the adhesion of the coating by penetrating phosphorus into the metal/coating interface. The optimum solution for plasma electrolytic oxidation coatings composed of 10, 3, and 3 g/l of tetra sodium pyrophosphate, sodium aluminate, and KOH, respectively. DC pulsed coating was shown to control the coating process and coating uniformity. Also the appropriate frequency to apply coating was DC pulse potential at 1000 Hz frequency under the 30% duty cycle.

ARTICLE INFORMATION

Article history:
Received 31 August 2020
Received in revised form 10 September 2020
Accepted 15 September 2020

Keywords:
Electrolyte plasma method
Aluminum oxide coatings
Potential applied regime

1. Introduction

Nowadays, many efforts have been made to expand the application of aluminum, its alloys and its composites [1-4]. In this regard, surface optimization of Al and its alloys by using easy, low-cost, and environmentally friendly methods is one of the most important fields of research [5-7]. Most surface engineering methods used in this regard are either costly (such as CVD methods, gas plasma, hot-dipping, and all vacuum-based methods) or they cause environmental problems (viz. anodizing methods or surface conversion coatings like chromate coatings) [8-11]. The oxidation method, unlike anodizing methods, is an eco-friendly method due to the use of alkaline solutions. In addition, by using the plasma electrolytic oxidation (PEO) method, creating thicker and more continuous coatings on the aluminum surface is possible [12-15]. PEO is a low-cost method among surface engineering techniques due to the creation of plasma in the electrolyte environment without requiring special conditions such as a vacuum or high temperature, and the use of simple and inexpensive salts [16]. By using the electric discharge and an electric arc generation at the metal/solution interface, it is possible to apply coatings with various properties and structures by controlling the electrical and electrolytic parameters. These advantages have attracted attention in industrial applications [17]. Coating of aluminum as well as its composites, and the deposition of hybrid and composite coatings on aluminum can be conducted by the PEO method.

PEO is a process for the chemical conversion of a metal surface into a hard oxide coating [18]. Aluminum is widely used in the aerospace and automotive industries due to its properties such as high corrosion resistance and high strength to weight ratio. However, the short-comings such as low hardness, low wear resistance and also high friction coefficient, have limited the use of aluminum alloys [19]. When the PEO layer is applied on the surface of aluminum, Al_2O_3 coating is formed on the surface of the sample, which causes good performance [20], high thermal resistance [21] , and good dielectric properties in the sample [22, 23]

Al_2O_3 compound is chemically stable and its melting temperature is as high as 2054 °C [24-27]. Therefore, it can be used in high temperature applications. Due to high hardness, strength and abrasion resistance of Al_2O_3, this material is offered as a promising material for catalysts and biological implantation [28, 29].

Recent research in the field of PEO coatings has focused on controlling the structure and morphology, stress level control, and the reduction of crack networks. In this research, the coating defects including porosity and crack networks are controlled by adjusting the electrical parameters to obtain improved properties for PEO aluminum coatings.

2. Materials and methods

2.1. Materials

In this research, 2025 aluminum sheet with a thickness of 4 mm, made by Arak Rolling Co, Iran, was used. The Al alloy contained 0.23% Si, 0.6% Fe, 0.22% Mg, 0.11% St, and 0.03 % Sn. Aluminum specimens with dimensions of 4×20×20 mm were cut. The surfaces of the samples were sanded with silicon carbide sandpapers up to the grit number of

---

* Corresponding author: Seyed Mohammad Mousavi khoei; E-mail: Mmousavi@aut.ac.ir

https://doi.org/10.29252/jcc.2.3.2

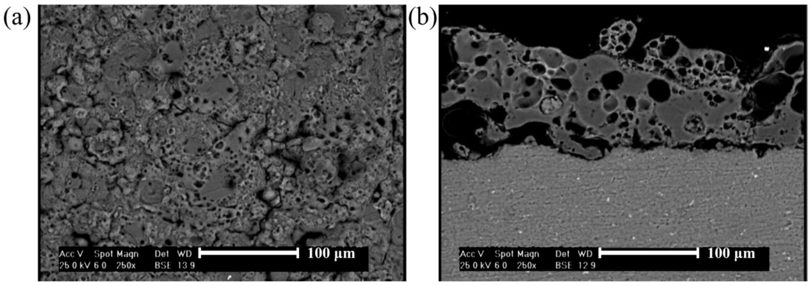

Fig. 1. SEM image of (a) surface and (b) cross-sectional area of sample 1 coated in electrolyte solution containing 2.5 g/l potash, 10 g/l sodium silicate under 500 V and 10 min.

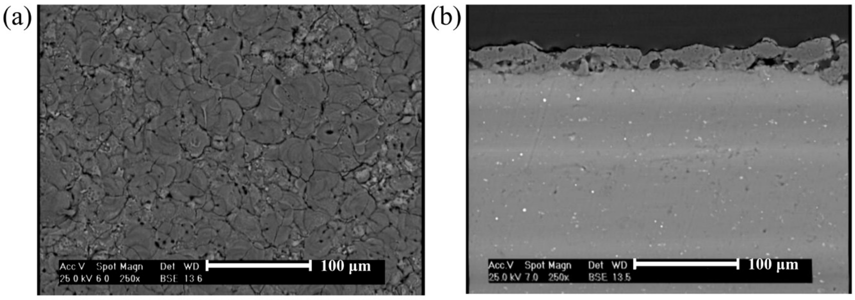

Fig. 2. SEM image of (a) surface and (b) cross-sectional area of sample 2 coated in electrolyte solution containing 2.5 g/l potash, 10 g/l sodium silicate and 8 g/l tetra sodium pyrophosphate under 500 V and duration of 10 min.

1800. Then, the samples were washed by ultrasonic method in pure ethanol and distilled water, dried in air before the PEO process.

2.2. POE process

First, the PEO coating was applied to the aluminum surface for 10 minutes at a potential of 500 V. After reaching the potential of 500 V, the current density was about 2.5 A/m^2. Then, the electric current gradually decreases during the process due to the formation of coating and its thickening.

In the pulse method, the ignition voltage is lower than the constant DC method, and due to the high intensity of the electric arcs, it is practically impossible to reach the potential of 500 V in the pulse method. Therefore, the value of electric current was considered as a controlling parameter instead of the potential value. In other words, the potential increased until the current reaches 7 A. Once this current was reached, the potential increase was stopped and kept constant during the PEO process. The electrical parameters measured during the PEO coating on the aluminum surface.

2.3. Morphological and structural studies

The phase composition of the coatings was studied by X-ray diffraction (XRD, Digaku D, max-2500) using Cu Kα radiation at 40 and 100 mA and a value of 2θ between 20° and 90°. The data was analyzed using the HighScore (Plus) v.4.7 software. For further evaluation of the morphology of the coatings and their thickness, a scanning electron microscope (Philips Model XL 30) was used. A 60-EC conductivity meter was used to measure the conductivity of the electrolyte solution. The thicknesses of the samples were measured using SEM images. Measurements were made at three points of the cross section that have the highest, lowest, and average thickness, and the average of the three values was reported. The thickness measurements were carried out using a QNix 7500 thickness gauge.

3. Results and discussion

Plasma electrolytic oxidation was performed in various electrolyte solutions and then all coated samples were cut with a micro cutter and

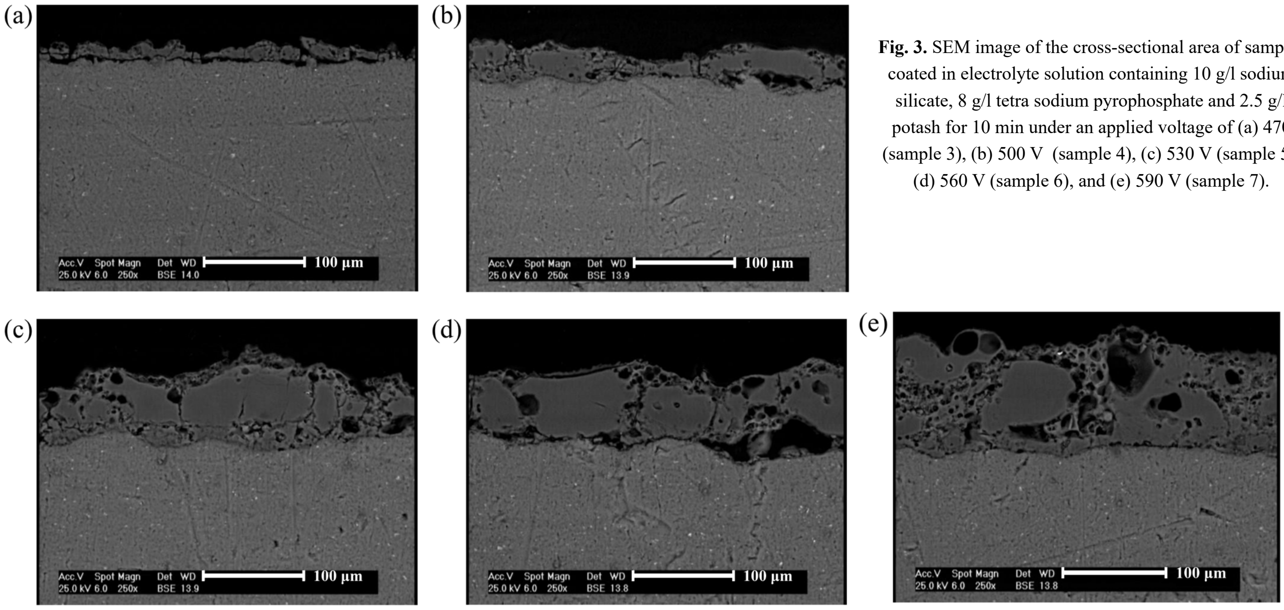

Fig. 3. SEM image of the cross-sectional area of samples coated in electrolyte solution containing 10 g/l sodium silicate, 8 g/l tetra sodium pyrophosphate and 2.5 g/l potash for 10 min under an applied voltage of (a) 470 (sample 3), (b) 500 V (sample 4), (c) 530 V (sample 5), (d) 560 V (sample 6), and (e) 590 V (sample 7).

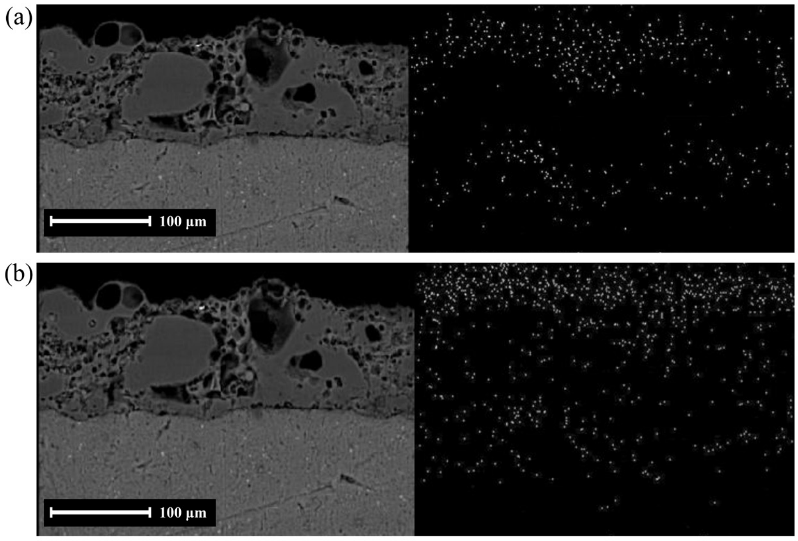

Fig. 4. Accumulation of (a) phosphorus and (b) silicon element in sample 7 coated in electrolyte solution including 10 g/l sodium silicate, 8 g/l tetra sodium pyrophosphate and 2.5 g/l potash for 10 min at an applied voltage of 590 V.

mounted to observe the surface morphology of the samples by SEM. Coated specimens generally consist of two dense layers and an outer porous layer, the structure of which is described below. At each stage, the sample with better surface properties was subjected to corrosion testing to facilitate the choice of the optimal solution.

3.1. Effect of sodium silicate on the morphology of the coating

In many studies, sodium silicate salt was used [19, 24, 27]. Therefore, to investigate the effect of this salt on the coating properties (Table 1), a sample was coated in the sodium silicate salt solution. In sample 1 that contains sodium silicate salt, the surface of the coating was so rough that it could be easily observed. As seen in Fig. 1(a), there is high volume of pores in the coating with the high thickness (about 40 mm). In addition, the volcanic structure is widely present on the surface. As seen in the cross-sectional area of the sample in Fig. 1(b), there are many holes in the interface of the coating and the substrate and consequently the coating does not adhere well to the substrate.

Because the selected solutions did not provide coating with appropriate properties, the composition of the salt solution was changed. Previous studies have suggested that tetra sodium pyrophosphate salts can be used to eliminate pores in the coatings and substrates interface, sodium aluminate to thicken coatings, and potassium hydroxide to increase solution conductivity and facilitate ion movement [19, 24]. By changing the concentration as shown in Table 3, the optimal solution is selected. Taking into account the morphology of the coating, surface properties, and the corrosion resistance, the optimal solution was sample 11. Therefore, this electrolyte composition was selected for coating.

The coating process was performed on sample 2, according to Table 1, in an electrolyte consisting of 10 g/l sodium silicate, 8 g/l tetra sodium pyrophosphate, and 2.5 g/l potassium hydroxide. The SEM images of sample 2 are seen in Fig. 2. According to SEM images, the coating surface was improved in terms of the amount and the size of micro-cavities and the structure has changed from volcanic to smooth surface. In Fig. 2(b), the cross section of the coating indicates that the sample 2 is much better than sample 1 in terms of surface morphology and the porosities were almost completely removed from the surface to the depth, but there are still cavities at the interface of the coating and the substrate that adversely affect the corrosion behavior. Fig. 2(a) clearly shows the boundaries between volcanic structures probably reduces the corrosion resistance of the coating layer.

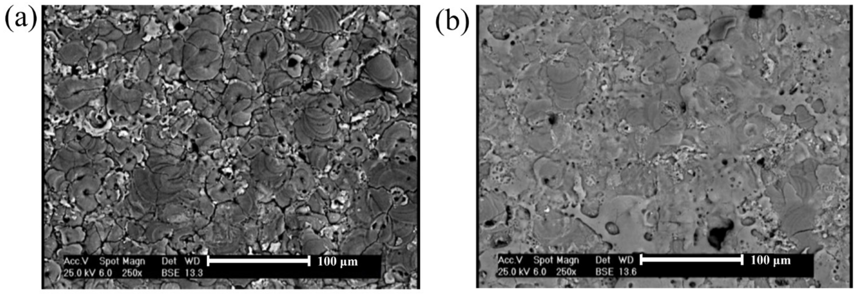

Fig. 5. SEM image of (a) sample 8 and (b) sample 9 coated in electrolyte solution including 8 g/l tetra sodium pyrophosphate 4 g/l sodium aluminate and 5 g/l potash for 10 min at an applied voltage of 500 V.

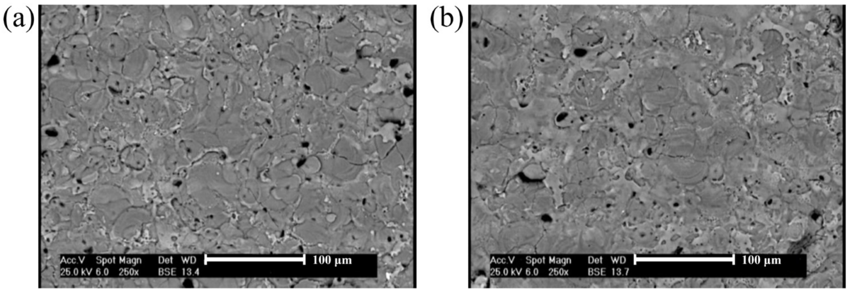

Fig. 6. SEM image of (a) sample 10 and (b) sample 11 coated in electrolyte solution consisting of 10 g/l tetra sodium pyrophosphate 3 g/l sodium aluminate and 5 g/l potash for 10 min at an applied voltage of 500 V.

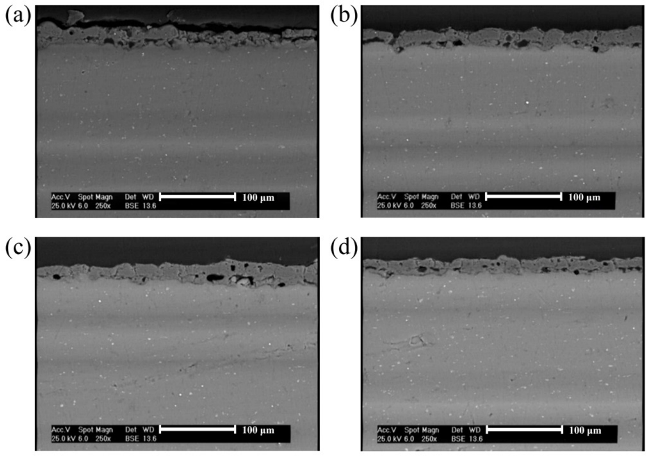

Fig. 7. SEM image of the cross section of (a) sample 8 (c) sample 10 coated in electrolyte solution including 8 g/l tetra sodium pyrophosphate 4 g/l sodium aluminate and 5 g/l potash for 10 min under an applied voltage 500 V and (b) sample 9 (d) sample 11 coated in electrolyte solution including 8 g/l tetra sodium pyrophosphate 4 g/l sodium aluminate and 3 g/l potash for 10 min at an applied voltage of 500 V.

Table 1.
Concentration of different additive electrolytes in silicate solution for coating at 500 V and 10 min at ambient temperature

Sample	KOH (g/l)	Sodium silicate (g/l)	Tetra sodium pyrophosphate (g/l)	Electrical conductivity (mS.cm^{-1})	pH
1	2.5	10	-	4.98	9.55
2	2.5	10	8	6.68	10.4

3.2. Investigation of the effect of voltage changes on the morphology of the coating prepared in silicate solution

As mentioned, the addition of tetra sodium pyrophosphate improved the surface properties; however, it was not satisfactory to be considered as an ideal coating. Thus, the effect of voltage increase on the morphology of coatings was studied. For this purpose, the coating process was performed under the conditions described in Table 2. The surface morphology of the coating was almost the same in all samples (3 to 7) and the differences were observed in the cross-sectional area. Fig. 3 corresponds to the cross-sectional area of the coated specimens under applied voltages of 470, 500, 530, 560, and 590 V. The electrolyte solution for all coated samples was the solution used for sample 2, which contains 10 g/l sodium silicate, 8g /l tetra sodium pyrophosphate, and 5 g/l potassium hydroxide. Coating process time is 10 minutes as shown in Table 2.

According to Fig. 3(a), which is related to the applied voltage of 470 V, the thickness of the coating is very low (about 18 µm). It seems that stable electric arcs have not yet been stabilized under this voltage. Also, the adhesion of the coating to the substrate is weak. In Fig. 3(b), in which the applied voltage is equal to 500 V, the coating is dense and looks uniform in terms of thickness (thickness is about 28 µm) and it has good adhesion to the substrate. The micro-cavities observed in the coating are part of the nature of plasma oxidation electrolytic coatings. In Fig. 3(c), which is related to the applied voltage of 530 V, the density of pores increased and the transverse cracks are obvious in the coating. Also, in Fig. 3(d), which is related to the voltage of 560 V, a gap was created between the coating and the substrate, and the cavities were transferred to the interface of the coating and the substrate, indicating that the coating is not suitable. In Fig. 3(e), at 590 V, the gap between the coating and the substrate is eliminated.

Table 2.
Different voltages applied to test the sample coated in electrolyte solution including 10 g/l sodium silicate, 8 g/l tetra sodium pyrophosphate, and 2.5 g/l potash with electrical conductivity equal to 6.68 mS.cm^{-1}and pH 10.4 in 10 min

Sample No.	3	4	5	6	7
Applied voltage (V)	470	500	530	560	590

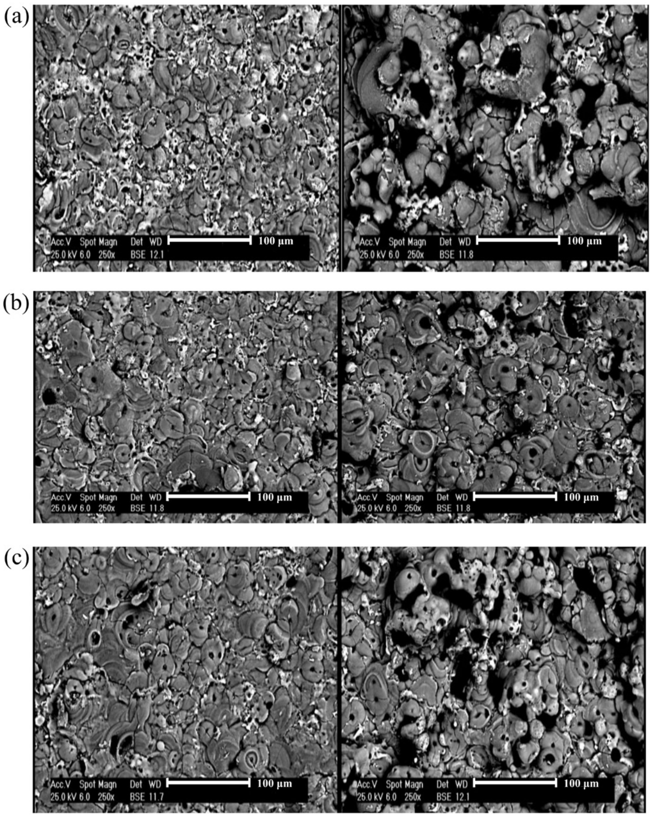

Fig. 8. Aluminum sample coated by applying a one-way pulse potential for 10 min in an electrolyte solution consisting of 10 g/l tetra sodium pyrophosphate 3 g/l sodium aluminate and 3 g/l potash at a frequency of (a) 1000Hz, (b) 2000 Hz, and (c) 3000 Hz with a working cycle of (left) 30% and (right) 70%.

3.3. Dispersion map of phosphorus and silicon elements in a sample coated with silicate solution

For a more detailed study, elemental analysis was taken from sample 7 to observe the accumulation of elements on the coating as shown in Fig. 4. According to the figures, silicate has accumulated mainly on the surface, while phosphate has accumulated on the inner and outer surfaces and has low levels of phosphorus in the middle of the coating. Therefore, the use of phosphate-based compounds seems to be appropriate. On the other hand, one of the major problems of coatings is the existence of a gap between the substrate and the coating, which might be due to the supply of aluminum ions from the substrate to create the coating, which causes the transfer of this ion from the substrate/coating interface

Table 3.
Concentrations of different species to find the optimal solution under the applied voltage of 500 V in 10 minutes at ambient temperature

Sample	KOH (g/l)	sodium aluminate (g/l)	Tetra sodium pyrophosphate (g/l)	Electrical conductivity (mS.cm^{-1})	pH
8	5	4	8	11.4	10.9
9	3	4	8	10.4	10.8
10	5	3	10	13.9	10.4
11	3	3	10	12.4	10.9

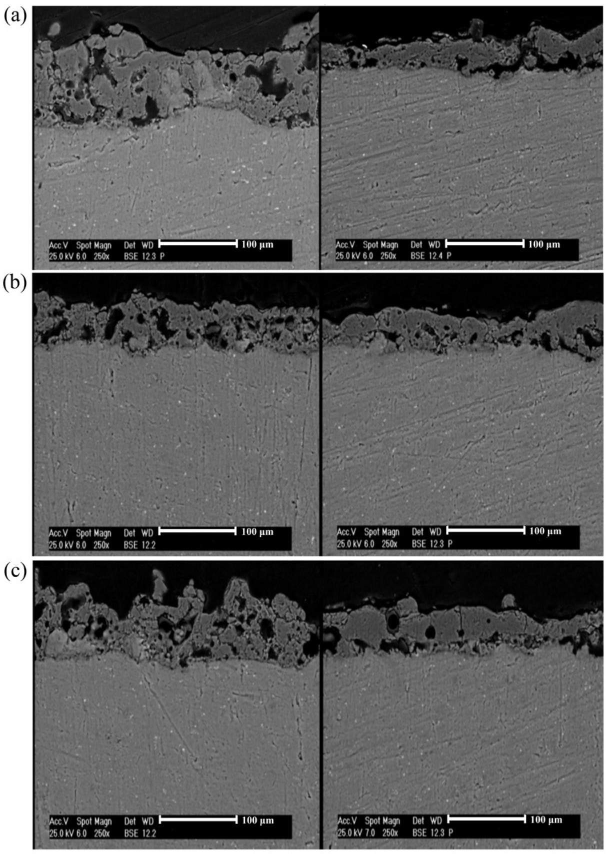

Fig. 9. Aluminum sample coated by applying a one-way pulse potential for 10 min in an electrolyte solution consisting of 10 g/l tetra sodium pyrophosphate 3 g/l sodium aluminate and 3 g/l potash at a frequency of (a) 1000 Hz, (b) 2000 Hz and (c) 3000 Hz with a working cycle of (left) 30 % and (right) 70%.

to the coating/electrolyte interface. The supply of aluminum ions in the electrolyte solution could alleviate this problem. In this way, the penetration of aluminum from the substrate is reduced and the aluminum ions in the electrolyte solution act as a contributing factor in the supply of aluminum coating and the amount of pores resulting from high transfer of aluminum from the substrate to the coating is reduced. Therefore, sodium aluminate was used in the electrolyte. In the following, different concentrations of these salts were used in order to achieve the optimal composition. It should be noted that the measured thicknesses are not real thickness values due to the porous structure of the PEO coatings.

3.4. Evaluation of the coating provided in the phosphate and silicate base electrolyte solution

As mentioned above, the use of the silicate electrolyte solution did not provide a coating with good properties; i.e. the surface generally had large pores and the coating did not adhere well to the substrate. Voltage also had little effect on coating improvement, and although the morphology appeared to be somewhat modified, it did not exhibit good corrosion resistance. However, in the case of current application regimes, the use of this electrolyte provides excellent coatings [20]. Based on previous studies [19, 24], sodium aluminate along with sodium pyrophosphate was used in the electrolyte. Fig. 5 shows the SEM images of the surface of the coating samples in the different electrolyte salts described in Table 6. The applied voltage for all cases was 500 V, which is lower than the ignition voltage and it does not enter the intense arc zone. On the other hand, the possibility of damage to the electrolytic plasma device

Table 4.
Frequency and operating cycles applied in pulse regime and with electrolyte solution electrolyte solution 10 g/l tetra sodium pyrophosphate, 3 g/l sodium aluminate, and 3 g/l potash with electrical conductivity equal to 12.45 mS.cm-1 and pH 10.9 in 10 min.

Sample	12	13	14	15	16	17
Frequency (Hz)	1000	1000	2000	2000	3000	3000
Working cycle	30%	70%	30%	70%	30%	70%

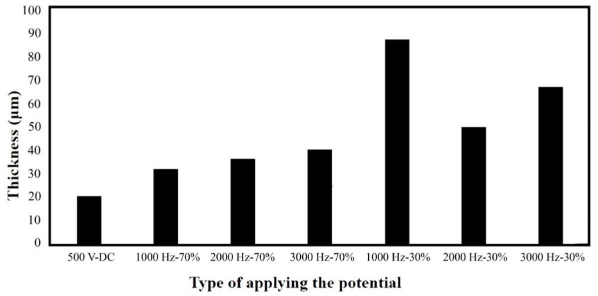

Fig. 10. The average value of coating thickness according to SEM observations under electrolyte solution including 10 g/l tetra sodium pyrophosphate 3 g/l sodium aluminate and 3 g/l potash for DC-500 V sample and Pulse samples at 1000, 2000 and 3000 frequencies in 30% and 70% duty cycle.

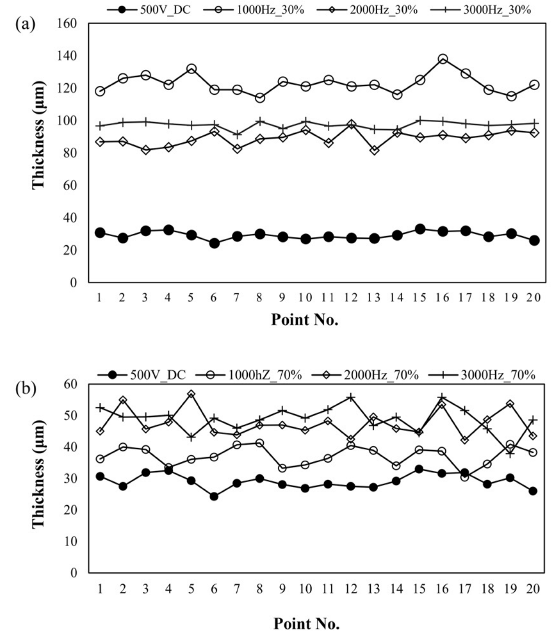

Fig. 11. Coating thicknesses in different parts of the surface under different coating conditions in electrolyte solution including 10 g/l tetra sodium pyrophosphate 3 g/l sodium aluminate and 3 g/l potash for DC-500 V sample and pulsed samples in frequency 1000, 2000 and 3000 in (a) 30% and (70%) duty cycle (measured with Quanix 7500 thickness gauge).

Table 5.
Electrical parameters measured during the PEO process on the aluminum surface. The area of the samples was about 42 cm^2.

Parameter	500 V-DC	Duty cycle 70%			Duty cycle 30%		
		1000 Hz	2000 Hz	3000 Hz	1000 Hz	2000 Hz	3000 Hz
Breaking voltage (V)	370	341	350	359	263	280	290
Starting voltage (V)	500	414	438	452	265	291	317
Final current (A)	1.7	1	1.7	1.6	2.8	1.5	1.9

is reduced under this voltage. The test time has also been optimized in previous experiments for this electrolyte solution at 10 minutes.

In general, the morphology of the coating in the electrolytic plasma oxidation process depends on the electrical parameters and the type of solution. In sample 8 (Fig. 5(a)), the amount of porosity is very high and the pores are interconnected and many surface cracks are observed, which can be caused by a large increase in the conductivity of the solution leading to the formation of strong electric arcs on the surface of the sample. In Fig. 5(b) (sample 9), as the amount of potassium hydroxide decreased compared to sample 8, the conductivity of the solution decreased and the amount of cracks was greatly reduced. In Fig. 6 (samples 10 and 11), due to the increase in phosphate compared to samples 8 and 9, the amount of porosity has been drastically reduced. Also, in these samples, the amount of volcanic structure in the surface decreased significantly and the surfaces are very smooth. Compared to sample 10, in sample 11 (Fig. 6(b)), the amount of porosity decreased by reducing the amount of potassium hydroxide as well as the conductivity of the solution. According to the SEM results, the surface of the samples seems to provide a coating with the expected corrosion resistance.

To compare the cross sections of the specimens and the metal/coating interface, SEM images of the cross sections of each specimen were also obtained (Fig. 7). As seen in the SEM images, the electrolyte solution has a significant effect on the coating thickness and compaction. In Fig. 7(a) (sample 8), the amount of cavities and surface porosities is very high. With the decrease in the amount of potassium hydroxide in sample 9, (Fig. 7(b)), the amount of porosity is remarkably reduced. Furthermore, by increasing the amount of phosphate (Fig. 7(c), sample 10), the coating has shown a better compaction and the gap between the substrate and the coating has been reduced to a desirable level. In Fig. 7(d) (sample 11), the thickness of the coating is more uniform than that of sample 10 (Fig. 7(c)), which appears to be due to a decrease in potassium hydroxide and the uniform ignition. In general, according to the SEM evaluations, the electrolyte solution used in sample 11 was selected as the appropriate solution for PEO tests. The thickness of the coating is estimated to be about 30 µm according to the SEM images.

According to SEM images, under the same conditions of the coating time and the applied voltage, by changing the percentage of tetra sodium pyrophosphate, sodium aluminate and potassium in the electrolyte, the adhesion of coating layer to the substrate and the amount of cavities have changed, however, the thickness of coating does not show variations as indicated in Table 7.

3.5. Influence of frequency and duty cycle on pulse potential application regime

Work cycle parameters and frequency are two important and effective parameters in the pulse DC potential application regime. To evaluate the effect of the work cycle, the coating process was done in the optimal solution as described in the previous steps, i.e. electrolyte solution of sample 11 involving 10 g/l tetra sodium pyrophosphate, 3 g/l sodium aluminate and 3 g/l potassium hydroxide under 30% and 70% work cycle. Different frequencies of 1000, 2000, and 3000 Hz are also selected to investigate the effect of coating frequency. A description of the test conditions is given in Table 4. The PEO process under the DC and pulse DC potential application regimes experiences different conditions in terms of breakdown voltage, process start voltage, and final current. PEO coating can also be performed by pulse potential regimen. The voltage was applied periodically (connected and disconnected). Frequency and operating cycle are important parameters in the pulse potential application regime. In a single pulse, t_{on} and t_{off} pulse are the periods in which the current is connected and disconnected, respectively. The work cycle parameter in the pulse regime is defined as follows [24].

$$D_t = \frac{t_{on}}{t_{on}+t_{off}} \times 100 \qquad (1)$$

To investigate the effect of these two coating parameters, the coating process was done in the optimal solution, i.e. electrolyte solution including 10 g/l tetra sodium pyrophosphate, 3 g/l aluminate and 3 g/l potassium hydroxide for 10 minutes. Coating is performed in 30% and 70% operating cycles at frequencies of 1000, 2000 and 3000 Hz, and the SEM images of the surface of the coating area are comparatively shown in Fig. 8. By changing the electrical parameters, the ignition behavior will change. In shorter operating cycles, micro-sparks are generated with higher density and lower intensity, which might be due to the breakdown voltage decrease, the increase in the micro-sparks distance, and the decrease in the intensity of the electrical discharge [24]. Therefore, the molten pools appearing as volcanic craters become smaller as observed in the SEM images. For example, in Fig. 8(a), which is related to the coating under the frequency of 1000 Hz, the working cycle is equal to 30% and the average diameter of the holes is about 3 µm. The micro-pores are dispersed throughout the coating layer, but in Fig. 8(a), the diameter of the pores has increased significantly (about 25 µm), and the pores are localized, and the uniform distribution of the pores was noticeably reduced.

Figs. 8 (b-c) are related to the coating at the frequencies of 2000 and 3000 Hz, respectively. With increasing the working cycle, the diameter of the pores and their percentage has increased. Also, under all three frequencies, with the increase of the work cycle, the growth of the coating becomes non-uniform and shows a mass structure which can be related to the increase in the intensity of micro-sparks due to the increase of the work cycle. The cross-sectional images are shown in Fig. 9. In Fig. 9 (a), which is related to the frequency of 1000 Hz and the duty cycle of 30%, the coating is thicker than other samples. In general, the percentage of porosity and their size have been improved compared to the DC potential application regime. In the SEM images of cross sections, spallation in the coating is observed, which seems to be related to the sample preparation for SEM observations.

3.6. Effect of thickness

The thickness of the samples was measured based on the SEM images. According to Fig. 10, the thickness of the coatings in all frequencies and operating cycles applied in the pulse mode is greater than that of the DC mode, which is probably due to the mechanism of the coating growth in the pulse mode. In the pulse mode, during the time when the voltage is cut off at the surface, the coating is dissolved and thus the coating pores are more easily filled and the coating grows more easily. Moreover, the maximum coating thickness is obtained at the frequency of 1000 Hz and the working cycle of 30%. At the same frequencies,

Table 6.
Thickness obtained from PEO coatings under different coating conditions in silicate or phosphate base electrolyte solution for 10 min

Sample	1	2	3	4	5	6	7
Thickness (µm)	112	26	18	28	75	65	97

Table 7.
Mean thickness obtained from SEM images in different amounts of tetra sodium electrophoresis of pephrophosphate, sodium aluminate and potash during coating for 10 minutes under voltage 500 V

Sample	8	9	10	11
Thickness (µm)	32	33	33	30

Table 8.
Mean thickness obtained from the thickness gauge handle in different potential application regimes

Applied regime	500 V-DC	1000 Hz-70%	2000 Hz-70%	3000 Hz-70%	1000 Hz-30%	2000 Hz-30%	3000 Hz-30%
Mean thickness (µm)	29.135	37.16	47.55	48.78	122.75	88.96	97.22

the thickness increases with decreasing duty cycle. As the duty cycle decreases, the number of micro-sparks increases and their intensity decreases. Therefore, the ignition of the coating becomes more uniform and the coating growth becomes easier. In the same work cycle, increasing or decreasing the frequency does not show a specific trend for thickness, which is probably due to the nature of PEO coating, because during coating, oxygen is constantly trapped in the coating. Furthermore, over a period in the pulse regime, which is proportional to the frequency and work cycle, the coating is dissolved and the released oxygen has the possibility to be released. However, sometimes, it may not be completely dissolved and the un-corroded areas act as centers of stress leading to the non-uniform growth of the coating in different areas.

Generally, the PEO coatings have a porous structure, and therefore, the reported thicknesses cannot be the actual thickness values. Thus, the thickness is measured at more points on the surface, but the SEM images illustrate only a limited cross section of the surface. For measuring the thickness, a QNix T500 thickness gauge was used. The results are shown in two graphs in Fig. 11. As can be seen, the thickness of the coating varies at different points on the surface. The reason for this is the nature of these coatings, which are formed based on electrical discharge and plasma generation. Due to the formation of an electric arc, molten oxide material is thrown out of the arc space and is solidified rapidly in the areas adjacent to the arc channel in contact with the electrolyte [24]. Therefore, the amount of accumulation of solid oxides in different parts of the surface will be different, which is the main cause of thickness differences in different parts of the sample surface. The strength of the electric arc and the amplitude of the created arc channel affect the amount of melt thrown out and the amount of oxides accumulated around these channels resulting in a change in the thickness of the samples and strength of arcs. The average values of the thicknesses obtained using the thickness gauge are given in Table 8.

4. Conclusions

In this research, electrolytic plasma method was used to prepare aluminum oxide coatings on the Al alloy and the effect of potential regimes was investigated. The obtained results are:

1. The optimal voltage to achieve a uniform coating with an ideal thickness and morphology was 500 V.

2. The addition of sodium silicate to the electrolyte solution caused porosity and non-adhesive coating on the substrate. On the other hand, the use of tetra sodium pyrophosphate increased the adhesion of the coating by the penetration of phosphorus into the metal/coating interface.

3. The optimal solution for coating by plasma electrolytic oxidation method is 10, 3, and 3 g/l of tetra sodium pyrophosphate, sodium aluminate, and KOH, respectively.

4. Coating by DC pulse method controls the coating process and the uniformity of the coating. The appropriate frequency for coating with pulse DC potential application regime is 1000 Hz under 30% duty cycle.

REFERENCES

[1] V.A. Andrei, C. Radulescu, V. Malinovschi, A. Marin, E. Coaca, M. Mihalache, C.N. Mihailescu, I.D. Dulama, S. Teodorescu, I.A. Bucurica, Aluminum Oxide Ceramic Coatings on 316l Austenitic Steel Obtained by Plasma Electrolysis Oxidation Using a Pulsed Unipolar Power Supply, Coatings 10(4) (2020) 318.

[2] T. Iman, G. Ehsan, Production methods of CNT-reinforced Al matrix composites: a review, Journal of Composites and Compounds 2(2) (2020).

[3] Z. Kaiqiang, J. Ho Won, L. Quyet Van, Production methods of ceramic-reinforced Al-Li matrix composites: A review, Journal of Composites and Compounds 2(3) (2020).

[4] E.H. Jazi, R. Esalmi-Farsani, G. Borhani, F.S. Jazi, Synthesis and Characterization of In Situ Al-Al$_{13}$Fe$_4$-Al$_2$O$_3$-TiB$_2$ Nanocomposite Powder by Mechanical Alloying and Subsequent Heat Treatment, Synthesis and Reactivity in Inorganic, Metal-Organic, and Nano-Metal Chemistry 44(2) (2014) 177-184.

[5] K. Zhang, H.W. Jang, Q. Van Le, Production methods of ceramic-reinforced Al-Li matrix composites: A review, Journal of Composites and Compounds 2(3) (2020) 77-84.

[6] M. Fattahi, K. Vaferi, M. Vajdi, F. Sadegh Moghanlou, A. Sabahi Namini, M. Shahedi Asl, Aluminum nitride as an alternative ceramic for fabrication of microchannel heat exchangers: A numerical study, Ceramics International 46(8, Part B) (2020) 11647-11657.

[7] B. Nayebi, A. Bahmani, M.S. Asl, A. Rasooli, M.G. Kakroudi, M. Shokouhimehr, Characteristics of dynamically formed oxide films in aluminum–calcium foamable alloys, Journal of Alloys and Compounds 655 (2016) 433-441.

[8] A. Chlanda, P. Oberbek, M. Heljak, E. Kijeńska-Gawrońska, T. Bolek, M. Gloc, Ł. John, M. Janeta, M.J. Woźniak, Fabrication, multi-scale characterization and in-vitro evaluation of porous hybrid bioactive glass polymer-coated scaffolds for bone tissue engineering, Materials Science and Engineering: C 94 (2019) 516-523.

[9] M. Shahedi Asl, B. Nayebi, M. Shokouhimehr, TEM characterization of spark plasma sintered ZrB$_2$–SiC–graphene nanocomposite, Ceramics International 44(13) (2018) 15269-15273.

[10] S.A. Delbari, B. Nayebi, E. Ghasali, M. Shokouhimehr, M. Shahedi Asl, Spark plasma sintering of TiN ceramics codoped with SiC and CNT, Ceramics International 45(3) (2019) 3207-3216.

[11] V.T. Targhi, H. Omidvar, S.M.M. Hadavi, F. Sharifianjazi, Microstructure and hot corrosion behavior of hot dip siliconized coating on Ni-base superalloy IN-738LC, Materials Research Express 7(5) (2020) 056527

[12] V. Egorkin, S. Gnedenkov, S. Sinebryukhov, I. Vyaliy, A. Gnedenkov, R. Chizhikov, Increasing thickness and protective properties of PEO-coatings on aluminum alloy, Surface and coatings Technology 334 (2018) 29-42.

[13] B. Kasalica, M. Petković-Benazzouz, M. Sarvan, I. Belča, B. Maksimović, B. Misailović, Z. Popović, Mechanisms of plasma electrolytic oxidation of aluminum at the multi-hour timescales, Surface and Coatings Technology 390 (2020) 125681.

[14] T. Kikuchi, T. Taniguchi, R.O. Suzuki, S. Natsui, Fabrication of a plasma electrolytic oxidation/anodic aluminum oxide multi-layer film via one-step anodizing aluminum in ammonium carbonate, Thin Solid Films 697 (2020) 137799.

[15] S. Wang, X. Liu, X. Yin, N. Du, Influence of electrolyte components on the microstructure and growth mechanism of plasma electrolytic oxidation coatings on 1060 aluminum alloy, Surface and Coatings Technology 381 (2020) 125214.

[16] N. Angulakshmi, R.B. Dhanalakshmi, M. Kathiresan, Y. Zhou, A.M. Stephan, The suppression of lithium dendrites by a triazine-based porous organic polymer-laden PEO-based electrolyte and its application for all-solid-state lithium batteries, Materials Chemistry Frontiers 4(3) (2020) 933-940.

[17] R. Hussein, D. Northwood, X. Nie, The effect of processing parameters and substrate composition on the corrosion resistance of plasma electrolytic oxidation (PEO) coated magnesium alloys, Surface and Coatings Technology 237 (2013) 357-368.

[18] B. Ghorbanian, S.M.M. Khoie, Formation of vanadium carbide with the plasma electrolytic saturation method (PES) and comparison with Thermo Reactive diffusion method (TRD), Acta Metallurgica Slovaca 22(2) (2016) 111-119.

[19] A. Yerokhin, X. Nie, A. Leyland, A. Matthews, S. Dowey, Plasma electrolysis for surface engineering, Surface and coatings technology 122(2-3) (1999) 73-93.

[20] B. Ghorbanian, S.M.M. Khoie, M. Rasouli, R.J. Doodran, Investigation of the electrolyte effects on formation of vanadium carbide via plasma electrolytic saturation method (pes), Surface Review and Letters 23(04) (2016) 1650021.

[21] Y. Gao, B. Ghorbanian, H.N. Gargari, W. Gao, Catalytic activity of char produced from brown coal for steam-gasification of bitumen oil, Petroleum Science and Technology 36(1) (2018) 75-78.

[22] Y. Gao, B. Ghorbanian, H.N. Gargari, W. Gao, Steam gasification of bitumen oil in presence of Ni/dolomite catalysts, Petroleum Science and Technology 35(21) (2017) 2074-2079.

[23] F. Momeni, B. Ghorbanian, S.M.M. Khoie, S.M.M. Nazari, M. Rasouli, Study of Current and Voltage Diagram In The Formed Vanadium Carbide Coatings Via Plasma Electrolytic Saturation Method, JOURNAL OF MATERIALS 7(11) (2016) 4073-4078.

[24] V. Dehnavi, B.L. Luan, D.W. Shoesmith, X.Y. Liu, S. Rohani, Effect of duty cycle and applied current frequency on plasma electrolytic oxidation (PEO) coating growth behavior, Surface and Coatings Technology 226 (2013) 100-107.

[25] V.T. Targhi, H. Omidvar, F. Sharifianjazi, A. Pakseresht, Hot Corrosion Behavior of Aluminized and Si-modified Aluminized Coated IN-738LC Produced by a Novel Hot-dip Process, Surfaces and Interfaces (2020) 100599.

[26] S. Rahimi, F. SharifianJazi, A. Esmaeilkhanian, M. Moradi, A.H. Safi Samghabadi, Effect of SiO2 content on Y-TZP/Al_2O_3 ceramic-nanocomposite properties as potential dental applications, Ceramics International 46(8, Part A) (2020) 10910-10916.

[27] M. Alizadeh, M.H. Paydar, F. Sharifian Jazi, Structural evaluation and mechanical properties of nanostructured Al/B_4C composite fabricated by ARB process, Composites Part B: Engineering 44(1) (2013) 339-343.

[28] J. Curran, T. Clyne, Thermo-physical properties of plasma electrolytic oxide coatings on aluminium, Surface and Coatings Technology 199(2-3) (2005) 168-176.

[29] Y.-J. Oh, J.-I. Mun, J.-H. Kim, Effects of alloying elements on microstructure and protective properties of Al_2O_3 coatings formed on aluminum alloy substrates by plasma electrolysis, Surface and Coatings Technology 204(1-2) (2009) 141-148.

Journal of Composites and Compounds 2 (2020) 123-128

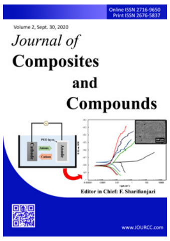

Available online at www.jourcc.com

Journal homepage: www.JOURCC.com

Journal of Composites and Compounds

Ni-Cu matrix composite reinforced with CNTs: preparation, characterization, wear and corrosion behavior, inhibitory effects

Morteza Ferdosi Heragh*[a]*, Sara Eskandarinezhad*[b], Alireza Dehghan*[c]***

[a] *Faculty of Materials and Metallurgical Engineering, Semnan University*
[b] *Department of Mining and Metallurgical Engineering, Yazd University, Yazd, Iran*
[c] *Department of Research and Development, Applied research center of the geological survey of Iran, Alborz, Iran*

ABSTRACT

St37 steel has been used in various industries due to its abundance and low cost. However, the high corrosion rate of steel in acidic environments is one of the limiting factors for its application. In this study, Ni-Cu composite coating reinforced with CNTs was applied on the st37 steel substrate. The extract of the Sarang Semut plant was added to the coating as inhibitory particles and the electrochemical behavior of the coating was investigated. The X-ray diffraction test was performed for phase analysis. Hardness, wear, and dynamic potential polarization tests were performed. Results showed that the presence of CNT particles improved the hardness, tribological performance, and electrochemical behavior of the coating. Also, the presence of Sarang Semut particles acted as a barrier and protected the surface of st37 steel from corrosion. It should be noted that these particles affected the kinetics and thermodynamics of corrosion reactions and were not involved in the reactions.

ARTICLE INFORMATION

Article history:
Received 18 August 2020
Received in revised form 13 September 2020
Accepted 17 September 2020

Keywords:
St37
Corrosion resistance
CNTs
Ni-Cu composite coating

1. Introduction

St37 steel is structural steel available in various forms. This type of steel is inexpensive and can be used in different applications including plant fabrication, piping, etc. Carbon is the main alloying element in the steel and there are some trace impurities as well. The hardness and strength of the steel are enhanced with the increment of the carbon content [1-4]. As steel and its alloys are extensively utilized in industrial components, their protection against acid electrolytes and their corrosive effect is necessary [5-7]. Common protection methods are alloying steel with inhibiting elements, using corrosion inhibitors, cathodic and anodic protection, and protective coatings [8, 9]. In various applications like the automotive and aerospace industry, composite coatings prepared via co-deposition of small reinforcement particles into a metal matrix are extensively used [10, 11]. It has been reported that the composite coatings could enhance microhardness, high-temperature stability, wear resistance, and corrosion resistance of metal and alloy. There are several factors that should be considered in selecting these coatings such as technical constraints, environmental pollution, costs, simplicity of the coating process [12-15].

In the marine environment, Ni-Cu alloys, particularly alloy that contain about 70%, Ni shows high corrosion resistance. Apart from corrosion resistance, solderability, ductility, and malleability are other attractive features. Cu and Ni have the standard reduction potentials of +0.34 V and 0.25 V vs. a normal electrode of hydrogen (NHE), respectively, which are disparate to some extent. A normal co-deposition of Ni and Cu is the plating process of Ni-Cu alloy. The incorporation of Cu in Ni strengthens it owing to the formation of a solid solution that enhances wear and corrosion resistance [16].

Besides the selection of the coating method, optimization of the electroplating method and the alloying system is also necessary. Some applicable techniques include electrodeposition, physical vapor deposition, chemical vapor deposition, plasma spraying, and thermal spraying. For the preparation of Ni coatings, electrodeposition has been reported to be a proper technique [17]. The reduction of the corrosion rate could occur in the alloy by adding metallic (e.g., Cr, or Mo) or nonmetallic (e.g., P, N or Si) inhibiting components, which forms adsorbed intermediate products on the alloy surface and blocks the active areas [8].

Since their emergence, carbon nanotubes (CNTs) have been increasingly used for the fabrication of advanced composites as the ideal reinforcing agent owing to their rewarding mechanical properties such as fracture strain sustaining capability, light weight, large elastic strain, and high elastic modulus [18-20]. However, CNT-containing composite applications are accompanied by the high complexity because several factors such as the nanotube/matrix bonding, nanotubes dispersion, reinforcement aspect ratio, surface reactivity, and densification of bulk composites should be controlled [8, 21-23]. In this research, the Ni-Cu/CNT composite coating is deposited on the st37 substrate, and its mechanical and corrosion behaviors as well as the inhibitory property of CNT on the coating surface were evaluated.

---

* *Corresponding author: Sara Eskandarinezhad; E-mail: s.eskandari.nezhad@gmail.com*

https://doi.org/10.29252/jcc.2.3.3

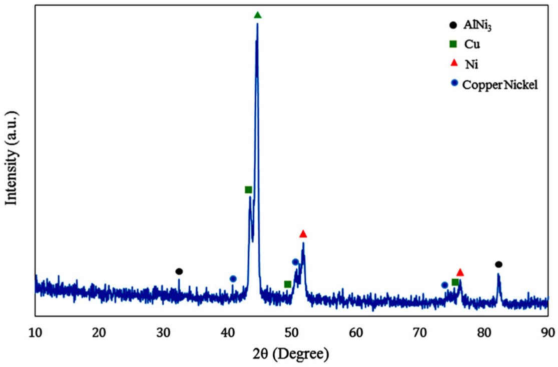

Fig. 1. XRD pattern for composite coated specimen.

2. Materials and method

2.1. Substrate preparation

The substrate used in this research for coating is St37 steel, and its chemical composition is shown in Table 1. The samples with 20×20×1 mm^3 dimensions were sanded using silicon carbide sandpaper (No. 60 to 3000) and then polished with alumina solution to reach an appropriate surface. Then the samples were washed with acetone and distilled water in order to remove the impurities from the surface and acid-washed by sulfuric acid (10 vol. %).

2.2. Preparation of electrolyte and coating

To prepare the electroplating bath, 100 g/L of $NiSO_4.6H_2O$, 25 g/L of $CuSO_4.5H_2O$, 32 g/L of H_3BO_3, 25, 100, and 500 mg/L of CNT, 0.30 g/L of sodium dodecyl sulphate (SDS) (German company Merck) were used. The complexing agent used in this study is $Na_3C_6H_5O_7$ (65 g/L). The conditions for applying the coating are listed in Table 2. The inhibitor used in this study is Sarang Semut, which has been studied by Shahab et al [24]. They prove that the extract of this plant has inhibitory properties in 3.5 wt. % sodium chloride solution. The extract was prepared from this plant (according to the research of Shahab et al.) and was completely pulverized after the production. In order to observe the effect of the presence of this extract on the composite coatings reinforced with CNT particles, 500 mg/L of this powder was mixed with 200 mg/L of reinforcing CNT particles, and then the mixture was added to the electroplating bath as the composite agent. The coating deposited in this bath was subjected to electrochemical tests.

The anode used in this study is a pure nickel sheet (99.99%) with 10×10×50 mm^3 dimensions. The anode and cathode were immersed vertically in a 400 cc of bath with a distance of about 5 cm between the anode and cathode and connected to the power supply by suitable electrical connections.

2.3. Characterization of coatings

Phase analysis of the coating was carried out by X-ray diffraction (XRD) using Philips Xpert pro type with Cu kα_1, 2θ range of 20-100°, step size of 0.03 at a voltage of 20 kV. Tribological behavior of the samples using the pin on disc was studied by BONG SHIN model obu-50 in humidity conditions of 35% and at a temperature of 31.5 ° C. The pin rotation speed was 0.125 m/s and wear distance was 50 m and the test was performed without lubricant. The conversion factor in these tests was 26.32 and the applied force was 10 N. The pin was made of hardened steel with 50 HRC hardness.

Table 1.
Chemical composition of steel used as substrate

Element	P	Mn	Si	S	C	Fe
wt. %	0.05	0.32	0.33	0.05	0.18	99.03

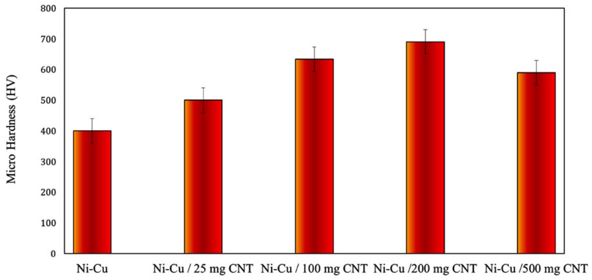

Fig. 2. Microhardness results of the applied coatings.

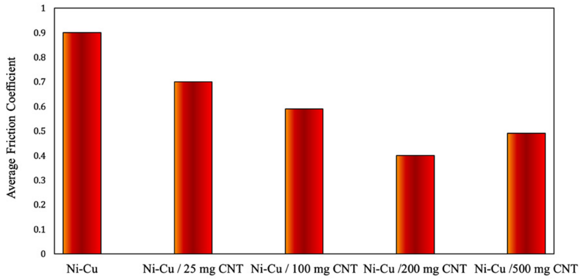

Fig. 3. Friction coefficient changes for coated specimens.

Potentiodynamic polarization (PDP) test was used to investigate the corrosion behavior of the samples. The samples were immersed in 3.5 wt. % sodium chloride for 1 hour to balance the chemical potential. Electrochemical experiments were carried out in a three-electrode-type cell with different compartments for the reference electrode (SCE). The counter electrode was a platinum plate, while the working electrode was St37 steel. Before each experiment, the working electrode was immersed in the test solution for 2 h at 25 °C to attain a stable open circuit potential (OCP).

The micro-hardness test was performed using the German Buhler machine, MMT-V model with Vickers submersible according to ASTM-E 384 standard under a load of 10 g for 10 seconds. The tests were randomly performed and finally, the average test results were presented.

Table 2.
Parameters of coating application

Parameter	Value
Temperature (°C)	35
Current density (A/dm^2)	2
Steering rate (rpm)	350
pH	4-5

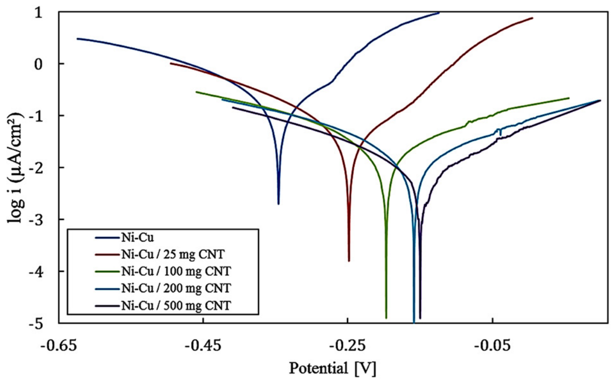

Fig. 4. PDP test results in 3.5% NaCl electrolyte.

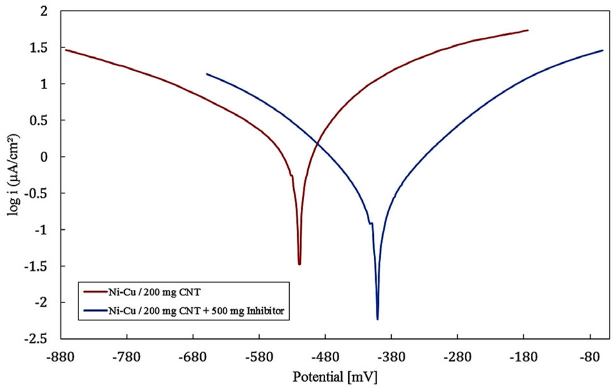

Fig. 5. PDP test results in 3.5% NaCl electrolyte for distorted specimens containing no inhibitor.

3. Results and discussion

3.1. XRD results

Fig. 1 indicates the XRD results of Ni-Cu/CNT alloy coatings. Fig. 1 shows that the Ni and Cu peak is present only in the coating. According to the figure, it is clear that nickel and copper together formed a solid solution leading to the formation of the nickel-copper alloy phase, and finally, the peak of this solid solution is observed, which has been proven in other studies as well [25, 26]. The conducted studies have shown that the presence of Cu atoms in the structure of Ni leads to a decrease in the lattice parameter and ultimately shifts 2θ to a lower value [27]. The figure clarifies that CNT peaks are seen in the X-ray pattern as well. This shows that CNT composite particles exist in the coating structure. Thus, the existence of CNT peaks in X-ray diffraction patterns shows that the fabrication of Ni-Cu/CNT composite coatings is possible using the electrodeposition method. Some studies show that the presence of composite particles like CNT or the presence of their alloying elements and cations like Cu^{2+} has led to changes in the energy of the growing plates. As the structure of the applied coating is related to the energy of the growing plates, the presence of CNT and Cu^{2+} particles leads to changes in the texture and structure of the specimens. It has been indicated that the changes in the texture of the specimens led to changes in the electrochemical and tribological behavior of the specimens [28-30].

According to Fig. 1, it is shown that peaks related to carbon nanoparticles are not seen, which may be due to the high density of peaks related to Ni or Cu. Another factor for the absence of peaks related to CNTs is their low concentration. This has been confirmed in the case of C_3N_4 carbon nitrite nanoparticles too [31].

3.2. Mechanical behavior of the specimens

The micro-hardness test was used to study the mechanical behavior of the specimens. Fig. 2 shows the micro-hardness results of the specimens. The hardness test was conducted to evaluate the micro-hardness of coatings applied to the cross-section of the specimens. Fig. 2 shows that composite specimens have a higher hardness compared with the Ni-Cu specimens. According to studies, it has been found that the hardness of the coating increases with the presence of Cu in the coating. The reason for the increase in hardness is related to the presence of Cu atoms in the correction of orientation and growth of coating grains [17, 30]. This issue can be seen in this study too. Fig. 2 shows that the hardness of the specimens increased with the presence of the secondary phase of CNT in the coating and the creation of Ni-Cu/CNT composite coating. The increase in hardness due to the presence of the secondary phase can be analyzed by several mechanisms. Texture change, change in grain boundary energy in the presence of secondary phase (Hall–Petch equation), dispersion strengthening (Orwan theory) are the causes that explain the increase in hardness in the presence of secondary particles [30, 32-34]. According to Orowan's theory, it is clear that the presence of CNT particles locks dislocations and hence prevents them from moving and ultimately leads to an increase in the hardness of the specimens.

Carbon nanotubes are one of the hardest materials in nature that have high strength and can withstand up to 55 GPa pressure conditions without degrading the tubular shape. The hardness of single-walled nanotubes can be up to 62 to 150 GPa. According to some studies, CNTs showed a much higher hardness compared to SiC in the nickel-phosphorus coating, which subsequently improved the abrasion properties.

According to Fig. 2, it is clear that the presence of nanotubes increases the hardness of the coatings. The presence of 25 mg/L of nanotubes increased the hardness from 400 to approximately 500 Vickers. The further increase in the concentration of nanotubes in the bath and the possibility of greater participation of nanotubes in the coating increase the hardness and reinforcing particles with uniform distribution inside the coating, thus reduce the role of the ground phase in the final hardness and load-bearing capacity by more particles. Therefore, the role of the matrix in the final hardness of the coating is reduced. Moreover, it is clear that by the increase in the nanotube concentration from 200 mg/L to 500 mg/L, the hardness of the specimens decreased. This can be because of the agglomeration of carbon nanoparticles. Carbon nanotubes agglomerate in 500 mg/L concentration and do not properly distribute, leading to the reduction of engineering properties of the specimens, including hardness. In three-component Ni-Cu-P-nano graphite composite coating, where lower concentrations of copper were used in the soluble compounds, the hardness increased due to the strengthening effect of the reinforcement particles. However, the hardness reduced in the solution with more copper compounds.

3.3. Tribological behavior of coatings

Pin-on-disk wear testing was used to study the tribological behavior of the specimens. The changes in the coefficient of friction of the specimens are shown in Fig. 3. According to this figure, it is clear that the average friction coefficients of composite specimens are lower than that of the Ni-Cu specimens. This shows an improvement in the tribological behavior of the specimens in the presence of the composite particle. The presence of carbon nanotubes as reinforcements has reduced the friction coefficient, which can be attributed to the atomic structure and shape of their tubes, leading to the property of self-lubrication [35, 36]. According to some studies, CNT particles increase coating hardness and strength (Hall–Petch and Orwan theory) [37], so they prevent the plastic deformation of the specimens during the wear test. During the abrasion process, the loss of material on the surface makes one end of the nanotubes placed vertically in the coating to be removed from the coating and due to the pressure of the pin, it becomes curved and the pin starts moving on its walls. Thus, this movement reduces the coefficient of friction [38]. Carbon nanotubes are made of concentric layers or walls of carbon tubes and the bonding of the layers is of the van der Waals type so they can easily slide over each other [39]. Dye et al. reported that nanotubes that detach from the surface act like a microbearing. CNTs can rotate, separate slippery surfaces, prevent strong contact between the two surfaces; thus, they reduce the friction coefficient, and increase wear resistance [31, 40].

It is clear that in the wear test, with an increase in the concentration of CNT to 500 mg/L, the coefficient of friction increased compared to the specimen of 200 mg/L, which can be analyzed by CNT agglomeration in the coating as well.

Among composites, carbon-reinforced composites have better abrasion behavior compared to ceramic-reinforced composites like Al_2O_3 or SiC, which is due to the lubricating nature of the carbon materials that make them natural reinforcement for lubricating composites [41].

3.4. Electrochemical behavior of coatings

3.4.1. Examining the electrochemical behavior of composite coating

The potentiodynamic polarization (PDP) test in 3.5 wt. % sodium chloride was used to examine the electrochemical behavior of the coatings. Fig. 4 shows the results of the PDP test. According to this figure, it is clear that the application of composite coatings caused a change in the electrochemical behavior of the specimens. This can be recognized by changes in the Tafel branches and the potential of the specimens. According to Fig. 4 and Table 3, it is clear that the presence of reinforcement particles in any amount has reduced the corrosion flow rate of the specimens [33, 42-46]. The reduction in the corrosion rate of composite specimens compared to the Ni-Cu alloy specimens can be due to a higher density of composite specimens. Due to the low ion radius of Cl^-, it is clear that increasing the density of the coating and reducing the micropores in the coating leads to the enhancement in the electrochemical behavior of the specimens. This is because increasing the density of the coating leads to a decrease in the penetration rate of this ion and ultimately the corrosion rate is reduced [47]. This has been proven in other studies [32, 33]. The improvement in the electrochemical behavior of the specimens due to the presence of CNT particles, in addition to the above, is related to the coating of metal sites by these particles in such a way that these particles reduce the charge transfer by creating electrical resistance between the electrolyte and the substrate. Ultimately, it enhances the electrochemical behavior of the specimens [34]. By studying the potential of the specimens, it is seen that the composite specimens have a nobler potential compared to the Ni-Cu specimen. The reason why the potential of composite specimens is nobler than Ni-Cu specimens is the presence of CNT particles. CNT shifts the potential of the specimens to more positive and noble values. This decreases the thermodynamic tendency of the specimens to perform corrosion reactions [48]. It is further clear that the anodic and cathodic slopes will undergo drastic changes if reinforcement particles are added. In other words, there is no parallel line between the branches of Ni-Cu diagrams and the composite specimens. This shows that the application of composite particles affected the mechanism of anodic and cathodic reactions [49].

Table 3.
Results extracted from PDP test by Tafel method

Sample	i_{corr} ($\mu A.cm^{-2}$)	E_{corr} (V)	β_a (mv/decade)	β_c (mv/decade)
Ni-Cu	3.16	-0.346	99	-84
Ni-Cu / 25 mg CNT	0.312	-0.248	96	-83
Ni-Cu / 100 mg CNT	0.031	-0.197	90	-79
Ni-Cu / 200 mg CNT	0.019	-0.158	91	-80
Ni-Cu / 500 mg CNT	0.012	-0.150	89	-81

3.4.2. Examining the electrochemical behavior of coating in the presence of inhibitor

It is clear that the presence of inhibitory particles in corrosion systems will reduce the corrosion rate. Thus, the use of inhibitors in the systems involved in corrosion reactions is one of the ways to prevent corrosion reactions. Inhibitors are used in corrosive soluble forms in corrosion protection systems. In this study, inhibitory particles were used as particles in the coating. Thus, the coating has inhibitory particles and if there is a scratch or scar in the coating, the inhibitor will be removed from the coating and it will protect the part of the base metal that does not have a coating by using inhibitory mechanisms. To this end, 500 mg/L of the inhibitory particles were mixed with 200 mg/L of CNT, and then the resulting powder was introduced into the plating bath as reinforcement particles. Ultimately, after coating, a small 5 mm scratch was applied to the coating, the specimen reinforced with inhibitory particles, and CNT was tested for PDP. Another specimen that does not contain inhibitory particles (Ni-Cu/200 mg CNT) was scratched about 5 mm and then subjected to PDP under the same conditions to compare the electrochemical behavior of this coating with coatings without inhibitory particles. Fig. 5 and Table 4 show the PDP test results for two composite specimens with and without the inhibitor.

Equation 1 was used to measure the inhibition percentage [50]:

$$\% IE = \frac{i_{Corr} - i_{Corr(\,Inhibitor)}}{i_{Corr}} \times 100 \tag{1}$$

In this equation, i_{Corr} is the corrosion current density in the absence of the inhibitor and $i_{Corr(Inhibitor)}$ is the corrosion current density in the presence of the inhibitor.

Fig. 5 and Table 4 clearly show that, firstly, by scratching the specimens, the corrosion rate of the specimens increases compared to healthy specimens. The presence of scratches in the coating facilitates the attack of ions like Cl^- and finally brings about an increase in the formation rate of the base metal chloride, which increases the corrosion rate of the specimens too. To prevent this, the study used inhibitory particles inside the coating. In other words, a coating is prepared by the incorporation of inhibitory particles. In case of damage to the coating and stripping of the base metal, the inhibitory particles enter the environment from the scratched area and protect the stripped metal site. The protection of the base metal is shown in Fig. 5 and Table 4. According to Fig. 5 and Table 4, it is clear that the corrosion rate in the inhibitor-containing specimen is lower than the specimen without the inhibitor, which is a reason for the inhibition by the particles applied in the coating. It is clearly seen that the potential of the scratched specimen shifts to more noble values with the presence of a scratched inhibitor. This shows that the thermo-

Table 4.
The results of Tafel PDP test for distorted specimens without and with inhibitor

Sample	i_{corr} ($\mu A.cm^{-2}$)	E_{corr} (V)	β_a (mv/decade)	β_c (mv/decade)	I.E (%)
Ni-Cu / 200 mg CNT	10.32	-0.518	95	-87	-
Ni-Cu / 200 mg CNT + 500 mg Inhibitor	5.011	-0.248	96	-83	51

dynamic inhibitory particles affect the corrosion reactions at the site of the bare metal and reduce corrosion reactions. As the corrosion rate decreases, it is clear that the kinetics of corrosion reactions are affected by the presence of inhibitors at the bare metal site, and in the presence of inhibitors, the kinetics of electron transfer is slowed down. Given the parallel state of Tafel branches, it is clear that the presence of inhibitory particles in the coatings has only affected the kinetics and thermodynamics of corrosion reactions and it was not able to change the mechanism of corrosion reactions in the present conditions [51].

4. Conclusions

In this research, the Ni-Cu alloy coating containing carbon nanotubes was produced. Then, the particles of the Sarang Semut plant were added to the coating as inhibitory particles and the electrochemical behavior of the coatings was investigated in the case of damaged coating in the presence of inhibitory particles. The results of the studies are as follows:

- In the Ni-Cu coating, CNT particles can be present as a composite agent.
- The presence of composite particles up to 200 mg/L improved the hardness of the samples compared to the pure Ni-Cu sample.
- Tribological behavior of the composite samples was more favorable than pure Ni-Cu samples and in the presence of composite particles up to 200 mg/L, the coefficient of friction of the samples decreased.
- By increasing the concentration of composite particles from 200 mg/L, the composite particles agglomerated and decreased the engineering properties of the samples such as mechanical and tribological properties.
- The presence of carbon nanotubes in the coatings led to the improvement of the electrochemical behavior of the samples due to the blockage of micropores, making the potential of the coatings nobler and creating insulation between the metal substrate and the electrolyte.
- The presence of Sarang Semut particles in addition to carbon nanotubes improved the electrochemical behavior of the coatings.
- In the coatings reinforced with CNT and Sarang Semut, in case of scratches in the coating, Sarang Semut particles act as an inhibiting agent and protect the bare surface of the metal from corrosion.
- Sarang Semut as an inhibitor is not able to change the mechanism of corrosion reactions and only affects the kinetics and thermodynamics of corrosion reactions.

REFERENCES

[1] N.D. Hassiotis, G.P. Petropoulos, Influence of surface roughness on corrosion resistance of turned carbon steel parts, International Journal of Machining and Machinability of Materials 1(2) (2006) 202-212.

[2] I. Tajzad, E. Ghasali, Production methods of CNT-reinforced Al matrix composites: a review, Journal of Composites and Compounds 2(1) (2020) 1-9.

[3] S.-W. Kim, B.-G. Jeon, D.-G. Hahm, M.-K. Kim, Ratcheting fatigue failure of a carbon steel pipe tee in a nuclear power plant using the deformation angle, Engineering Failure Analysis (2020) 104595.

[4] P. Jordan, C. Maharaj, Asset management strategy for HAZ cracking caused by sigma-phase and creep embrittlement in 304H stainless steel piping, Engineering Failure Analysis 110 (2020) 104452.

[5] M. Ferdosi Heragh, H. Tavakoli, Electrochemical Properties of a New Green Corrosion Inhibitor Derived from Prosopis farcta for St37 Steel in 1 M Hydrochloric Acid, Metals and Materials International (2019).

[6] A.H. Shahbaz, M. Esmaeilian, R. NasrAzadani, K. Gavanji, The effect of MgF_2 addition on the mechanical properties of hydroxyapatite synthesized via powder metallurgy, Journal of Composites and Compounds 1(1) (2019) 18-24.

[7] S.E. Sanni, A.P. Ewetade, M.E. Emetere, O. Agboola, E. Okoro, S.J. Olorunshola, T.S. Olugbenga, Enhancing the inhibition potential of sodium tungstate towards mitigating the corrosive effect of Acidithiobacillus thiooxidan on X-52 carbon steel, Materials Today Communications 19 (2019) 238-251.

[8] A. Pruna, Advances in carbon nanotube technology for corrosion applications, Handbook of Polymer Nanocomposites. Processing, Performance and Application, Springer2015, pp. 335-359.

[9] R.S. Erami, M. Amirnasr, S. Meghdadi, M. Talebian, H. Farrokhpour, K. Raeissi, Carboxamide derivatives as new corrosion inhibitors for mild steel protection in hydrochloric acid solution, Corrosion Science 151 (2019) 190-197.

[10] M. Adabi, A.A. Amadeh, Electrodeposition mechanism of Ni–Al composite coating, Transactions of Nonferrous Metals Society of China 24(10) (2014) 3189-3195.

[11] Z.M. Al-Rashidy, M. Farag, N.A. Ghany, A. Ibrahim, W.I. Abdel-Fattah, Orthopaedic bioactive glass/chitosan composites coated 316L stainless steel by green electrophoretic co-deposition, Surface and Coatings Technology 334 (2018) 479-490.

[12] T. Abedi, S.K. Asl, Synthesis of a novel functionally graded coatings of Ni-Cr/Al_2O_3 nanocomposite coating by pulse electrodeposition, Materials Research Express 6(5) (2019).

[13] D. Zhang, H. Zhang, S. Zhao, Z. Li, S. Hou, Electrochemical impedance spectroscopy evaluation of corrosion protection of X65 carbon steel by halloysite nanotube-filled epoxy composite coatings in 3.5% NaCl solution, Int. J. Electrochem. Sci 14 (2019) 4659-4667.

[14] X. He, R. Song, D. Kong, Microstructure and corrosion behaviour of laser-cladding Al-Ni-TiC-CeO_2 composite coatings on S355 offshore steel, Journal of Alloys and Compounds 770 (2019) 771-783.

[15] M.A.U. Rehman, M.A. Munawar, D.W. Schubert, A.R. Boccaccini, Electrophoretic deposition of chitosan/gelatin/bioactive glass composite coatings on 316L stainless steel: A design of experiment study, Surface and Coatings Technology 358 (2019) 976-986.

[16] Z. Abdel Hamid, A.Y. El-Etre, M. Fareed, Performance of Ni–Cu–ZrO_2 nanocomposite coatings fabricated by electrodeposition technique, Anti-Corrosion Methods and Materials 64(3) (2017) 315-325.

[17] M. Alizadeh, H. Safaei, Characterization of Ni-Cu matrix, Al_2O_3 reinforced nano-composite coatings prepared by electrodeposition, Applied Surface Science 456 (2018) 195-203.

[18] Z. Hu, X. Jie, G. Lu, Corrosion resistance of Pb–Sn composite coatings reinforced by carbon nanotubes, Journal of coatings technology and research 7(6) (2010) 809-814.

[19] Y. Orooji, A.a. Alizadeh, E. Ghasali, M.R. Derakhshandeh, M. Alizadeh, M.S. Asl, T. Ebadzadeh, Co-reinforcing of mullite-TiN-CNT composites with ZrB_2 and TiB_2 compounds, Ceramics International 45(16) (2019) 20844-20854.

[20] A. Agarwal, S.R. Bakshi, D. Lahiri, Carbon nanotubes: reinforced metal matrix composites, CRC press2018.

[21] G. Fan, Y. Jiang, Z. Tan, Q. Guo, D.-b. Xiong, Y. Su, R. Lin, L. Hu, Z. Li, D. Zhang, Enhanced interfacial bonding and mechanical properties in CNT/Al composites fabricated by flake powder metallurgy, Carbon 130 (2018) 333-339.

[22] M. Chen, G. Fan, Z. Tan, D. Xiong, Q. Guo, Y. Su, J. Zhang, Z. Li, M. Naito, D. Zhang, Design of an efficient flake powder metallurgy route to fabricate CNT/6061Al composites, Materials & Design 142 (2018) 288-296.

[23] M. Akbarpour, S. Alipour, M. Farvizi, H. Kim, Mechanical, tribological and electrical properties of Cu-CNT composites fabricated by flake powder metallurgy method, Archives of Civil and Mechanical Engineering 19 (2019) 694-706.

[24] A. Pradityana, Sulistijono, A. Shahab, S. Chyntara, Eco-friendly green inhibitor of mild steel in 3, 5% NaCl solution by Sarang Semut (Myrmecodia Pendans) extract, AIP Conference Proceedings, AIP, 2014, pp. 161-164.

[25] P. Dai, C. Zhang, J. Wen, H. Rao, Q. Wang, Tensile properties of electrodeposited nanocrystalline Ni-Cu alloys, Journal of Materials Engineering and Performance 25(2) (2016) 594-600.

[26] I. Bakonyi, E. Tóth-Kádár, J. Tóth, T. Becsei, T. Tarnóczi, P. Kamasa, Magnetic and electrical transport properties of electrodeposited Ni-Cu alloys and multilayers, Journal of Physics: Condensed Matter 11(4) (1999) 963.

[27] U. Sarac, M.C. Baykul, Morphological and microstructural properties of two-phase Ni–Cu films electrodeposited at different electrolyte temperatures, Journal of alloys and compounds 552 (2013) 195-201.

[28] L. Chen, L. Wang, Z. Zeng, T. Xu, Influence of pulse frequency on the microstructure and wear resistance of electrodeposited Ni–Al_2O_3 composite coatings, Surface and Coatings Technology 201(3) (2006) 599-605.

[29] L. Wang, Y. Gao, Q. Xue, H. Liu, T. Xu, Microstructure and tribological properties of electrodeposited Ni–Co alloy deposits, Applied Surface Science 242(3-4) (2005) 326-332.

[30] M. Zamani, A. Amadeh, S.L. Baghal, Effect of Co content on electrodeposition mechanism and mechanical properties of electrodeposited Ni–Co alloy, Transactions of Nonferrous Metals Society of China 26(2) (2016) 484-491.

[31] L. Reinert, S. Suárez, A. Rosenkranz, Tribo-mechanisms of carbon nanotubes: friction and wear behavior of CNT-reinforced nickel matrix composites and CNT-coated bulk nickel, Lubricants 4(2) (2016) 11.

[32] A. Laszczyńska, J. Winiarski, B. Szczygieł, I. Szczygieł, Electrodeposition and characterization of Ni–Mo–ZrO_2 composite coatings, Applied Surface Science 369 (2016) 224-231.

[33] Q. Feng, T. Li, H. Teng, X. Zhang, Y. Zhang, C. Liu, J. Jin, Investigation on the corrosion and oxidation resistance of Ni–Al_2O_3 nano-composite coatings prepared by sediment co-deposition, Surface and Coatings Technology 202(17) (2008) 4137-4144.

[34] M. Alizadeh, Strengthening mechanisms in particulate Al/B_4C composites produced by repeated roll bonding process, Journal of Alloys and Compounds 509(5) (2011) 2243-2247.

[35] M. Alishahi, S.M. Monirvaghefi, A. Saatchi, S.M. Hosseini, The effect of carbon nanotubes on the corrosion and tribological behavior of electroless Ni–P–CNT composite coating, Applied Surface Science 258(7) (2012) 2439-2446.

[36] Z.-q. MENG, X.-b. LI, Y.-j. XIONG, Z. Jing, Preparation and tribological performances of Ni-P-multi-walled carbon nanotubes composite coatings, Transactions of Nonferrous Metals Society of China 22(11) (2012) 2719-2725.

[37] R. Casati, M. Vedani, Metal matrix composites reinforced by nano-particles—a review, Metals 4(1) (2014) 65-83.

[38] Z. Li, X. Wang, M. Wang, F. Wang, H. Ge, Preparation and tribological properties of the carbon nanotubes–Ni–P composite coating, Tribology international 39(9) (2006) 953-957.

[39] X. Chen, C. Chen, H. Xiao, H. Liu, L. Zhou, S. Li, G. Zhang, Dry friction and wear characteristics of nickel/carbon nanotube electroless composite deposits, Tribology international 39(1) (2006) 22-28.

[40] W. Chen, J. Tu, H. Gan, Z. Xu, Q. Wang, J. Lee, Z. Liu, X. Zhang, Electroless preparation and tribological properties of Ni-P-Carbon nanotube composite coatings under lubricated condition, Surface and Coatings Technology 160(1) (2002) 68-73.

[41] A.D. Moghadam, E. Omrani, P.L. Menezes, P.K. Rohatgi, Mechanical and tribological properties of self-lubricating metal matrix nanocomposites reinforced by carbon nanotubes (CNTs) and graphene–a review, Composites Part B: Engineering 77 (2015) 402-420.

[42] A. Barbucci, G. Farne, P. Matteazzi, R. Riccieri, G. Cerisola, Corrosion behaviour of nanocrystalline $Cu_{90}Ni_{10}$ alloy in neutral solution containing chlorides, Corrosion Science 41(3) (1998) 463-475.

[43] H. Dhar, R.E. White, G. Burnell, L. Cornwell, R. Griffin, R. Darby, Corrosion of Cu and Cu-Ni alloys in 0.5 M NaCl and in synthetic seawater, Corrosion 41(6) (1985) 317-323.

[44] A. Varea, E. Pellicer, S. Pané, B.J. Nelson, S. Suriñach, M.D. Baró, J. Sort, Mechanical properties and corrosion behaviour of nanostructured Cu-rich CuNi electrodeposited films, Int. J. Electrochem. Sci 7(2) (2012) 1288-1302.

[45] H.-h. Zhou, Z.-w. Liao, C.-x. Fang, H.-x. Li, F. Bin, X. Song, G.-f. Cao, Y.-f. Kuang, Pulse electroplating of Ni-WP coating and its anti-corrosion performance, Transactions of Nonferrous Metals Society of China 28(1) (2018) 88-95.

[46] M. Metikoš-Huković, I. Škugor, Z. Grubač, R. Babić, Complexities of corrosion behaviour of copper–nickel alloys under liquid impingement conditions in saline water, Electrochimica acta 55(9) (2010) 3123-3129.

[47] Q. Li, X. Yang, L. Zhang, J. Wang, B. Chen, Corrosion resistance and mechanical properties of pulse electrodeposited Ni–TiO_2 composite coating for sintered NdFeB magnet, Journal of Alloys and Compounds 482(1-2) (2009) 339-344.

[48] H.R. Bakhsheshi-Rad, X. Chen, A.F. Ismail, M. Aziz, E. Abdolahi, F. Mahmoodiyan, Improved antibacterial properties of an Mg-Zn-Ca alloy coated with chitosan nanofibers incorporating silver sulfadiazine multiwall carbon nanotubes for bone implants, Polymers for Advanced Technologies 30(5) (2019) 1333-1339.

[49] L.-Y. Cui, S.-D. Gao, P.-P. Li, R.-C. Zeng, F. Zhang, S.-Q. Li, E.-H. Han, Corrosion resistance of a self-healing micro-arc oxidation/polymethyltrimethoxysilane composite coating on magnesium alloy AZ31, Corrosion Science 118 (2017) 84-95.

[50] S. Mo, L.J. Li, H.Q. Luo, N.B. Li, An example of green copper corrosion inhibitors derived from flavor and medicine: vanillin and isoniazid, Journal of Molecular Liquids 242 (2017) 822-830.

[51] M. Abdallah, Antibacterial drugs as corrosion inhibitors for corrosion of aluminium in hydrochloric solution, Corrosion Science 46(8) (2004) 1981-1996.

Journal of Composites and Compounds 2 (2020) 129-137

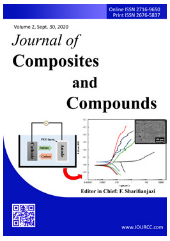

Available online at www.jourcc.com

Journal homepage: www.JOURCC.com

Journal of Composites and Compounds

Corrosion behavior of aluminum oxide coatings created by electrolytic plasma method under different potential regimes

Mahsa Amiri*[a]*, Vahid Tavakoli Targhi*[a]*, Saman Padervand*[a]*, Seyed Mohammad Mousavi khoei*[a]**

[a] *Material and Metallurgical Engineering Department, Amirkabir University of Technology, Hafez Street, Tehran, Iran*

A B S T R A C T

The electrolytic plasma coating is affected by various factors such as electrolyte conductivity, voltage, and current. However, there has not been much attention to the effect of the current regime. The main objective of the present study is to investigate the potential of Al_2O_3 coatings deposited by the electrolytic plasma method. Aluminum Series 2 was used in this study and the electrolyte was composed of sodium silicate, sodium tetraphosphate, sodium aluminate and potassium hydroxide. The results showed that, in general, according to the impedance diagrams, the corrosion resistance of the coated specimens greatly increases with the immersion time. Therefore, the unit of resistance increased on average to about 10 MHz after 72 hours. In the case of pulsed potential application regime, the corrosion behavior of the samples in the working cycle of 30% was better than that of 70%, which can be related to the thickness of the formed coatings and their porosity. This allows the coating to degrade the coating faster by increasing the thickness and decreasing the porosity of the aggressive chloride ion.

A R T I C L E I N F O R M A T I O N

Article history:
Received 17 August 2020
Received in revised form 13 September 2020
Accepted 20 September 2020

Keywords:
Plasma electrolytic oxidation
Aluminum oxide coatings
Potential regime
Corrosion

1. Introduction

Aluminum and its alloys are of particular importance in the industry due to their light weight, excellent chemical resistance, especially in neutral environments, and high strength to weight ratio [1-3]. They are mainly used in the aerospace, automotive, oil and gas, and drilling industries. Automotive and aircraft parts, pump shells, valves, tanks for transporting petroleum products are among the most important uses of aluminum and its alloys. Aluminum also has many applications in the marine industry. The construction of high-speed vessels is perhaps the most tangible example of this application [4]. Aluminum has good corrosion resistance in many solutions, but in cases where it is in contact with high concentrations of aggressive corrosive agents such as chloride, severe local corrosion occurs [4, 5]. In seawater environment, due to the high concentration of dissolved oxygen, especially chloride ions, the aluminum structures suffer from local corrosion. Therefore, if a suitable surface treatment is performed on aluminum, the service life of aluminum structures and equipment will increase significantly in corrosive environments and it will be used with more confidence [4].

Plasma electrolytic oxidation (PEO) using high voltage is a recently developed surface engineering method [6]. PEO is considered as a method between a common low voltage anodizing in aqueous solutions and a high-energy plasma coating in dry conditions in a controlled gas pressure chamber [7]. PEO can produce ceramic coatings on light metal surfaces with improved properties and the thickness of ten to hundreds of microns [8]. Oxide coatings are produced by high voltage anodic polarization in an electrolyte [9]. Using this method, it is possible to coat aluminum composites as well as hybrid and composite coatings on aluminum substrate [10, 11].

Despite the industrial application of the PEO method, all aspects of this process have not yet been scientifically identified. As a result, PEO is considered as a new method in the field of surface engineering [12, 13]. Despite the excellent mechanical and chemical properties of PEO coatings, researchers are still trying to further improve their properties [14]. It should be noted that parameters affecting the process could severely affect its corrosion and abrasion properties. Among the effective parameters, the type of applied electrical regime can affect the porosity and cracking networks of the coating as well as its chemical composition. Therefore, by selecting the appropriate electrical regime, and controlling the porosity, cracking and the type of formed phases in the coating, better mechanical properties and corrosion resistance can be provided for PEO coatings [12, 15-17].

In order to improve the protective performance of the coating, the defects of the coating must be controlled. Process control can be done with the effective parameters mentioned earlier. Recent research in the field of controlling the structure and morphology of PEO coatings, stress level control and reduction of crack networks are among the most important areas of research in the field of PEO process. In this research, an attempt is made to create enhanced corrosion properties for PEO aluminum coatings by controlling the electrical parameters. Therefore, in this research, aluminum is coated by the PEO process and the effect of different potential regimes on the corrosion resistance is evaluated.

---

* *Corresponding author: Seyed Mohammad Mousavi khoei; E-mail: Mmousavi@aut.ac.ir*

https://doi.org/10.29252/jcc.2.3.4

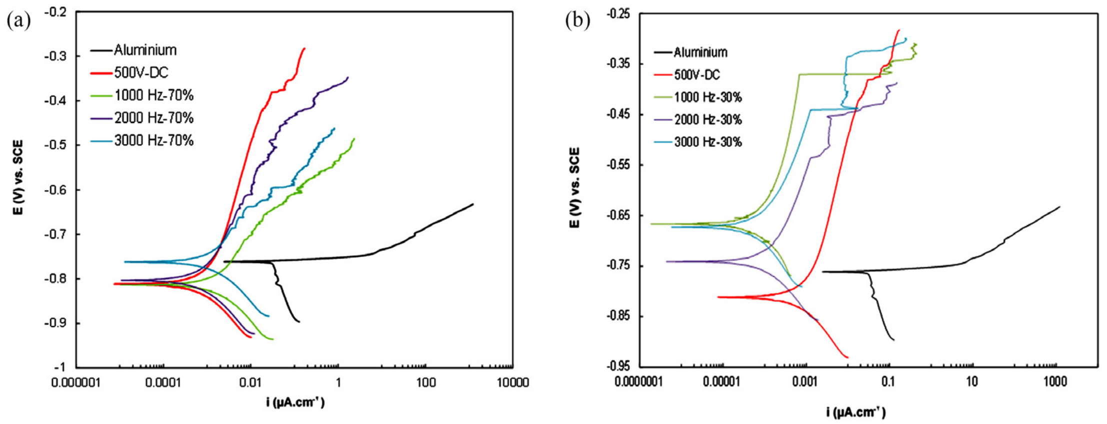

Fig. 1. Polarization diagrams of uncoated aluminum sample and coated aluminum samples with constant potential application of 500 V and application of unilateral pulse potential in different frequencies and operating cycles of (a) 70% and (b) 30% after 72 hours of immersion in 3.5 wt%. sodium chloride solution at room temperature - the solution was static and the potential scan rate was 0.2 mv.sec^{-1}.

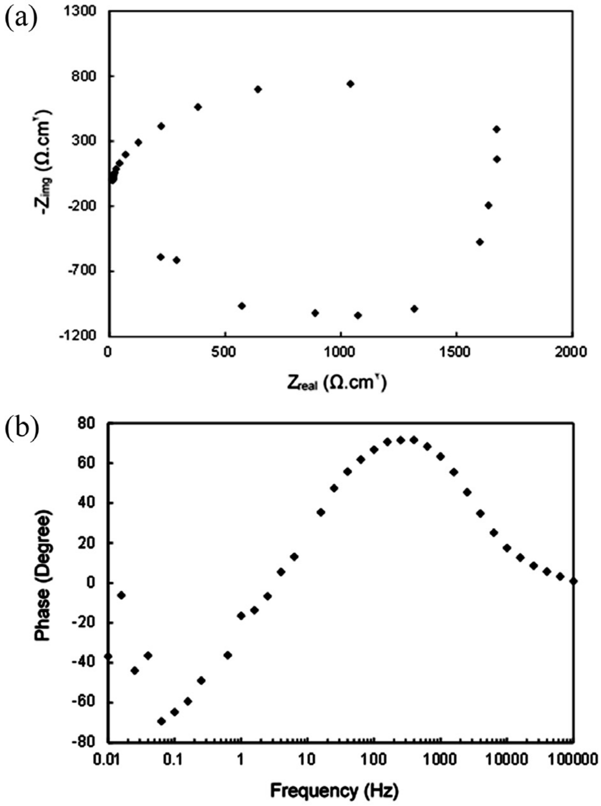

Fig. 2. (a) Nyquist and (b) Bode-phase diagrams of aluminum in 3.5 wt% of sodium chloride at room temperature after 45 min of immersion.

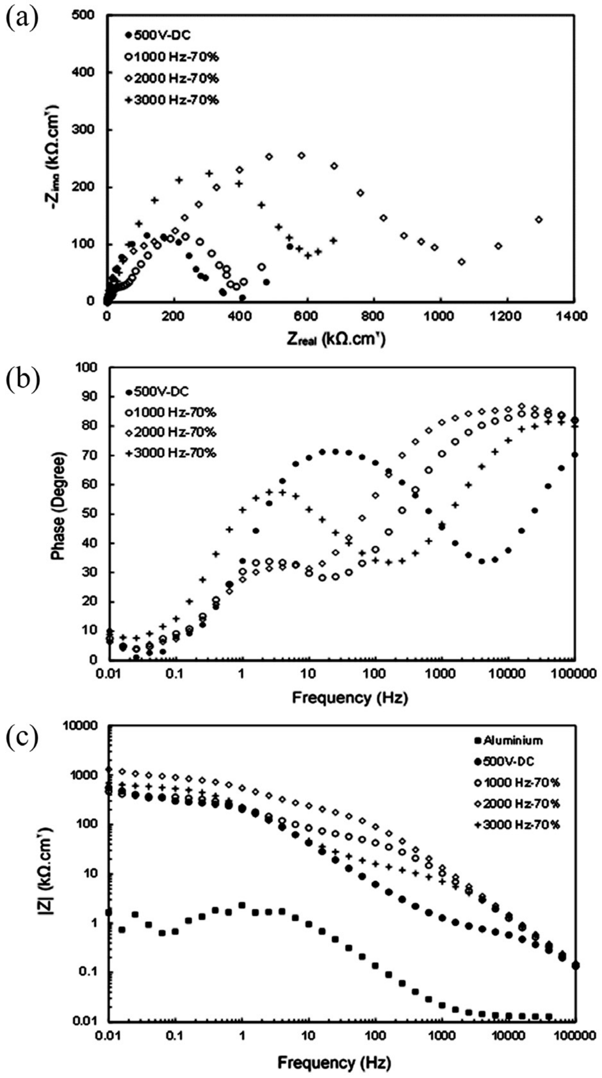

Fig. 3. (a) Nyquist, (b) Bode-phase, and (c) Bode-modulus diagrams of PEO-coated aluminum specimens by applying constant potential and one-way pulse in 70% fixed duty cycle and different frequencies in 3.5 wt% of sodium chloride after 45 min of immersion.

2. Material and methods

2.1. Materials and sample preparation

In this research, 2025 aluminum sheet with the thickness of 4 mm containing the chemical composition of 0.23% silicon, 0.6% Fe, 0.22% Mg, 0.11% St, 0.03% of Sn (produced by Arak Rolling Company, Iran) was used. Aluminum specimens were cut into 4×20×20 mm dimensions. The surfaces of the samples were sanded by silicon carbide sandpapers up to the grit number of 1800. Then, the samples were cleaned by the ultrasonic method in pure ethanol and distilled water and dried in the air before the PEO process. Based on the initial optimization experiments, the optimal electrolyte composition of 10 g/l tetra sodium pyrophosphate, 3 g/l sodium aluminate and 3 g/l potash (KOH) was used and according to the obtained morphologies, the coating time of 10 minutes was selected.

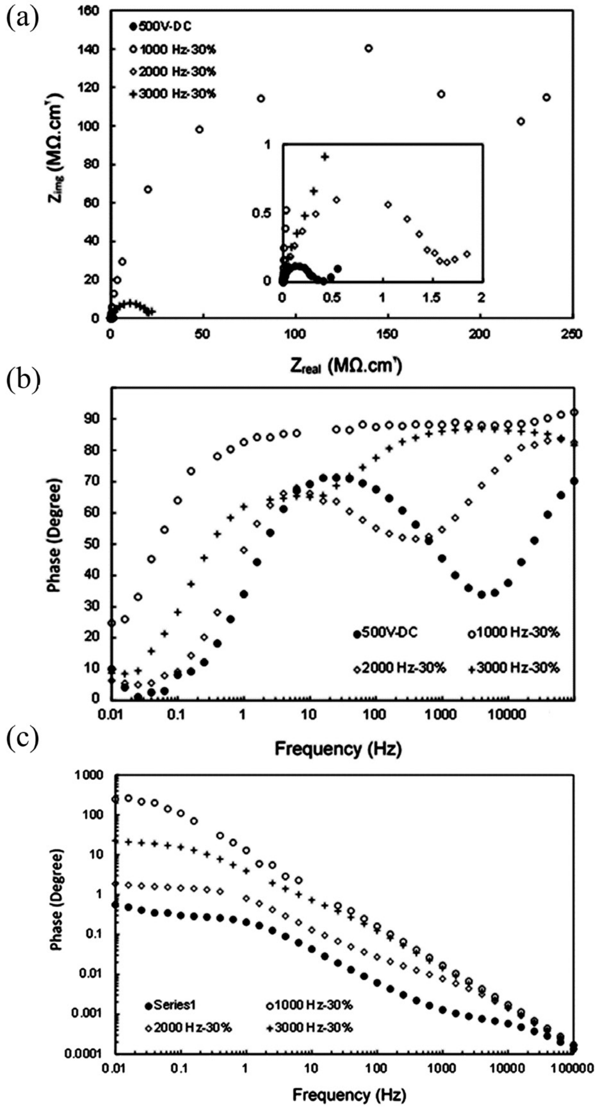

Fig. 4. (a) Nyquist, (b) Bode-phase, and (c) Bode-modulus diagrams of PEO-coated aluminum specimens by applying constant potential and one-way pulse in 30% fixed duty cycle and different frequencies in 3.5 wt% of sodium chloride after 45 min of immersion.

2.2. PEO process

The PEO coating was applied on the aluminum surface at a potential of 500 V for 10 minutes. The current density after reaching the potential of 500 V was about 2.5 Am^{-2}. The electric current gradually decreased during the process due to the formation of coating and its thickening.

Table 1.

The electrical parameters measured during the PEO process. The area of the samples was about 4 cm^2.

Parameter	DC-500V	Duty cycle 70%			Duty cycle 30%		
		1000 Hz	2000 Hz	3000 Hz	1000 Hz	2000 Hz	3000 Hz
Breakdown Voltage (V)	370	341	350	359	263	280	290
Starting Voltage (V)	500	414	438	452	265	291	317
Final Current (A)	1.7	1	1.7	1.6	2.8	1.5	1.9

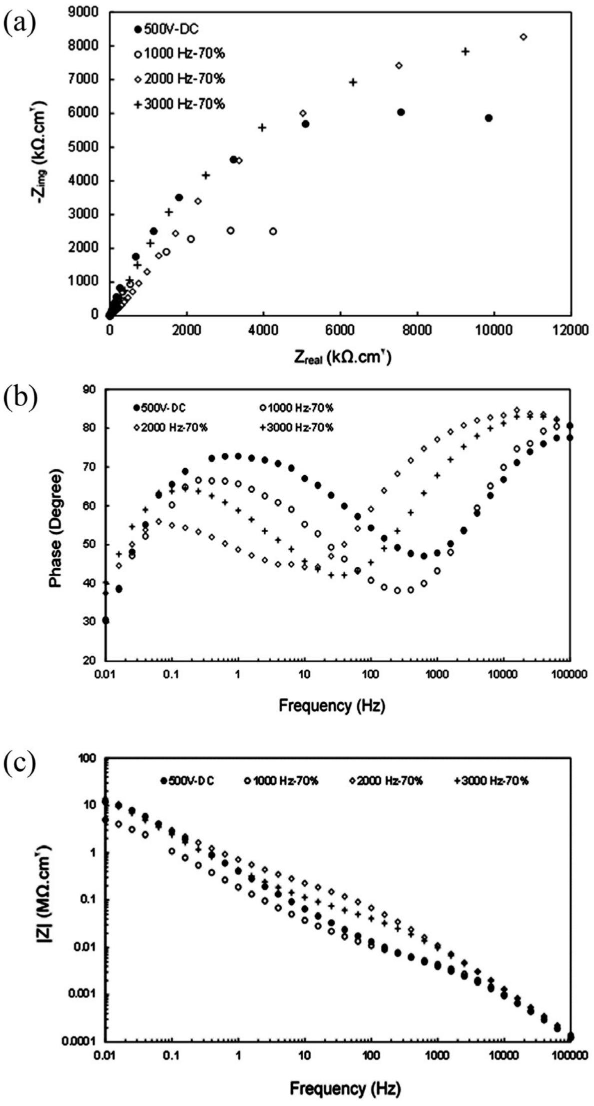

Fig. 5. (a) Nyquist, (b) phase-Bode, and (c) Bode-modulus diagrams of PEO-coated aluminum specimens by applying constant potential and one-way pulse in 70% fixed duty cycle and different frequencies in 3.5 wt% of sodium chloride after 24 h of immersion.

In the pulse method, the ignition voltage practically occurs earlier than the constant DC mode and due to the high intensity of the generated electric arcs, it is practically impossible to reach the potential of 500 V. Therefore, instead of the potential value, the amount of electric current is considered as a controlling parameter. In other words, when the potential is applied, the potential increases until the current reaches 7 A. Once this current is reached, the potential increase stops and the PEO process continues without the potential increase. Table 1 shows the electrical parameters measured during the PEO process.

2.3. Morphological and structural analysis

The phase composition of coatings was evaluated using X-ray diffraction (XRD, Digaku D/max-2500) using Cu Kα radiation at 40 and 100 mA and at 2θ between 20° and 90°. For studying the morphology and thickness of the coating, a scanning electron microscope (SEM) manufactured by Philips XL 30 was used. A 60-EC conductivity meter was used to measure the conductivity of the electrolyte solution. The thickness of the samples was measured using SEM images. Measurements were made at three points of the cross section (maximum, minimum, and the average thickness), and the average of these three values was reported. The thickness measurement was done using a Quanix 7500 thickness gauge.

2.4. Polarization test

Electrochemical polarization tests were performed in a three-electrode cell with EG&G A273A potentiostat/galvanostat. For EIS tests, a Solartron FRA device (SI 1255) coupled with potentiostat/galvanostat was used. The saturated calomel electrode was used as the reference electrode and the graphite rod was used as the auxiliary electrode. Electrochemical impedance tests were performed in the frequency range of 10 mHz-100 kHz with a range of 10 mV (rms) and after reaching the equilibrium potential of the samples. Polarization tests were performed after the immersion period (72 hours) with a scanning velocity of 0.2 mV/s from -150 mV relative to the open circuit potential to about +500 mV relative to the open circuit potential. Electrochemical polarization tests were performed with ACM Gill 8 potentiostat/galvanostat apparatus manufactured by ACM. Polarization diagrams were analyzed to determine TOEFL slopes and corrosion velocities with ACM software (ACM Analysis Version 4). It should be noted that all electrochemical corrosion tests were performed at ambient temperature and in 3.5% (wt%) sodium chloride solution.

2.5. Electrochemical Impedance Spectroscopy (EIS)

In order to create a linear system, the application of alternating voltage of 10 mV was used to disturb the steady state of the system [6]. In this project, Princeton Applied Research Model 1025 made by EG&G Company was used. Saturated calomel reference electrode made by Azar Electrode and the used cell was the same used for the polarization test.

3. Results and discussion

In this study, two polarization and electrochemical impedance tests were used to investigate the corrosion resistance and its properties in PEO coatings. Here, the results of these tests will be discussed.

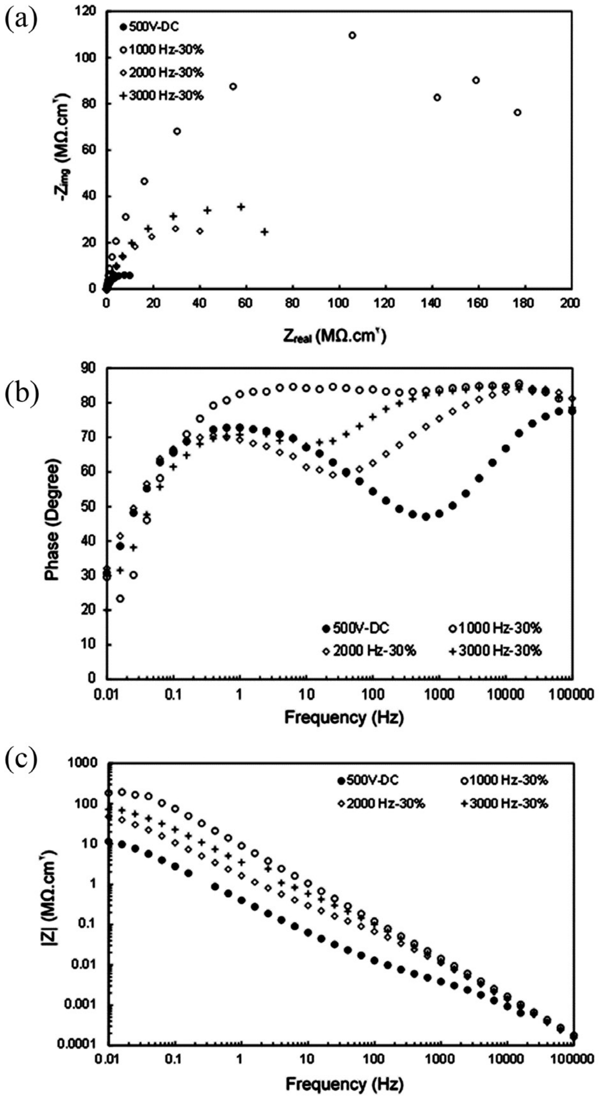

Fig. 6. (a) Nyquist, (b) Bode-phase, and (c) Bode-modulus diagrams of PEO-coated aluminum specimens by applying constant potential and one-way pulse in 30% fixed duty cycle and different frequencies in 3.5 wt% of sodium chloride after 24 h of immersion.

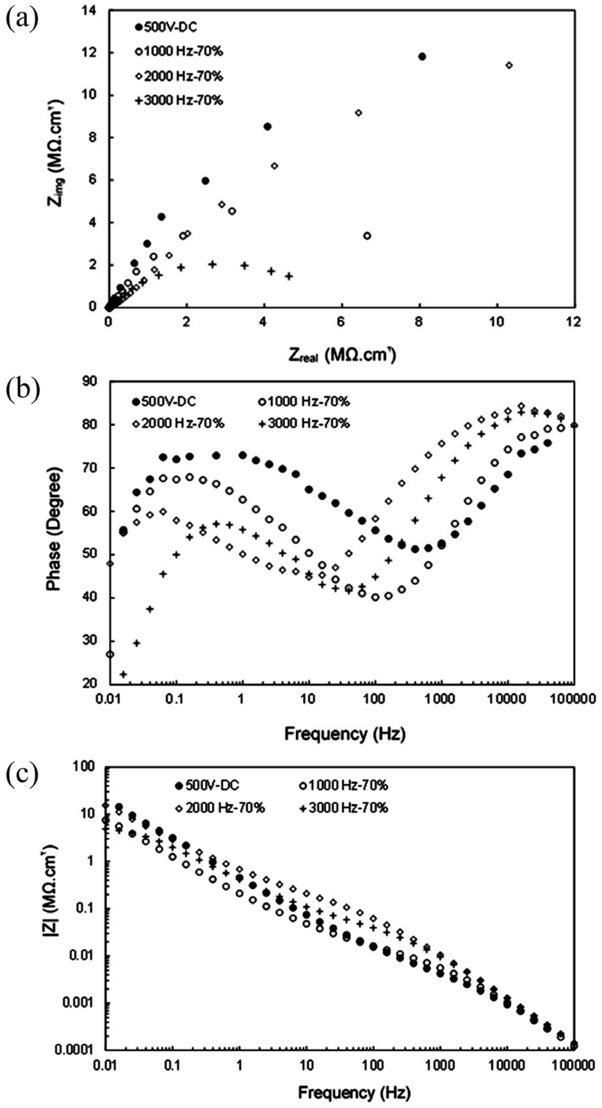

Fig. 7. (a) Nyquist, (b) Bode-phase, and (c) Bode-modulus diagrams of PEO-coated aluminum specimens by applying constant potential and one-way pulse in 70% fixed duty cycle and different frequencies in 3.5 wt% of sodium chloride after 48 h of immersion.

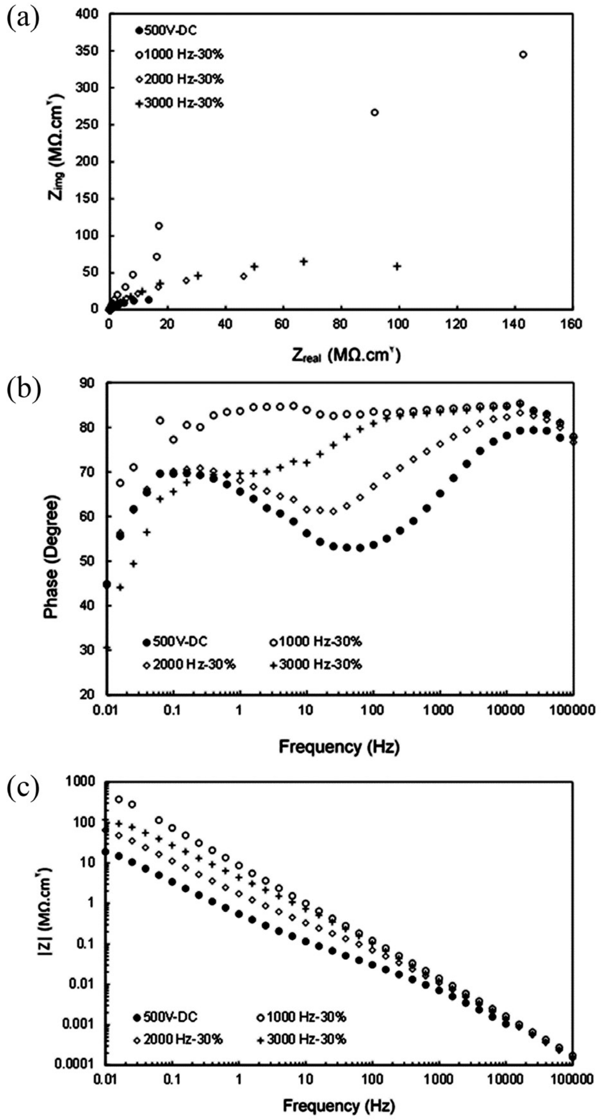

Fig. 8. (a) Nyquist, (b) Bode-phase, and (c) Bode-modulus diagrams of PEO-coated aluminum specimens by applying constant potential and one-way pulse in 30% fixed duty cycle and different frequencies in 3.5 wt% of sodium chloride after 48 h of immersion.

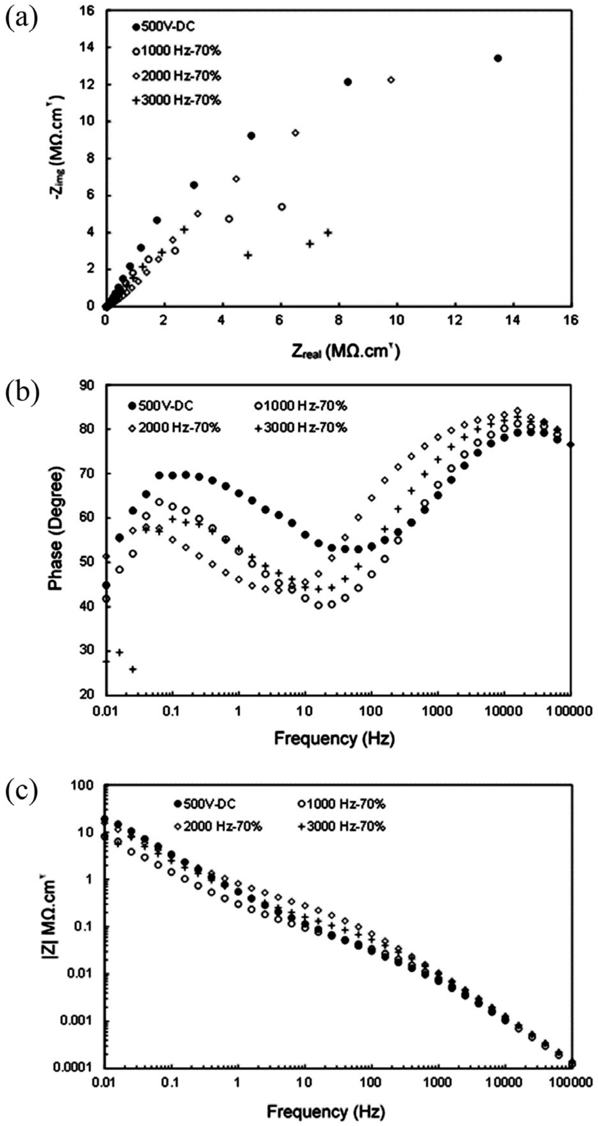

Fig. 9. (a) Nyquist, (b) Bode-phase, and (c) Bode-modulus diagrams of PEO-coated aluminum specimens by applying constant potential and one-way pulse in 70% fixed duty cycle and different frequencies in 3.5 wt% of sodium chloride after 72 h of immersion.

3.1. Polarization test

Fig. 1(a) shows that by creating PEO coatings on the aluminum surface, the polarization diagram is transferred to lower current values. In fact, with the formation of PEO coating, corrosion of aluminum in sodium chloride solution has been reduced by 3.5 wt%. Polarization diagrams have a special behavior in sodium chloride medium. As can be seen, the anode branch of the aluminum polarization diagram experiences a sharp increase in current with a small increase in potential. This type of anodic polarization behavior generally means that the pitting potential is very close to the corrosion potential. In other words, the pitting potential almost overlaps the corrosion potential [18-20]. Under these conditions, the metal or alloy undergoes severe local corrosion in the corrosive environment. Therefore, according to the polarization diagram of uncoated aluminum in Fig. 1(b), it is possible to predict severe local corrosion of aluminum in sodium chloride medium. With the creation of PEO coatings, this behavior is practically not observed and there is almost a considerable difference between the corrosion potential and the pitting potential. Therefore, it seems that the presence of PEO coatings has a positive role in controlling local and pitting corrosion of aluminum. Among PEO coatings, the largest difference between corrosion potential and pitting corrosion potential is observed for the sample coated in the constant potential application regime; in other words, this coating has a better performance than other coatings in preventing local corrosion (pits) on aluminum surface.

The polarization curves of the uncoated and coated samples with a constant potential application of 500 V and a one-way pulse potential application at different frequencies of 70% and 30% duty cycle are shown in Fig. 1. After immersion in 3.5 wt% sodium chloride solution at room temperature, the samples were polarized. As can be seen in the figures, by applying the PEO coating on the samples, polarization curves are shifted to the left and the shift in current density is low, which indicates a decrease in corrosion current in the presence of the PEO coating. Therefore, the PEO coating clearly reduces the corrosion rate of aluminum. Also, according to Fig. 1, the cathodic branches of uncoated and coated samples do not show a significant difference, while in the anodic branches of uncoated samples with a small increase in potential, a sharp increase in current is observed. This means that the corrosion

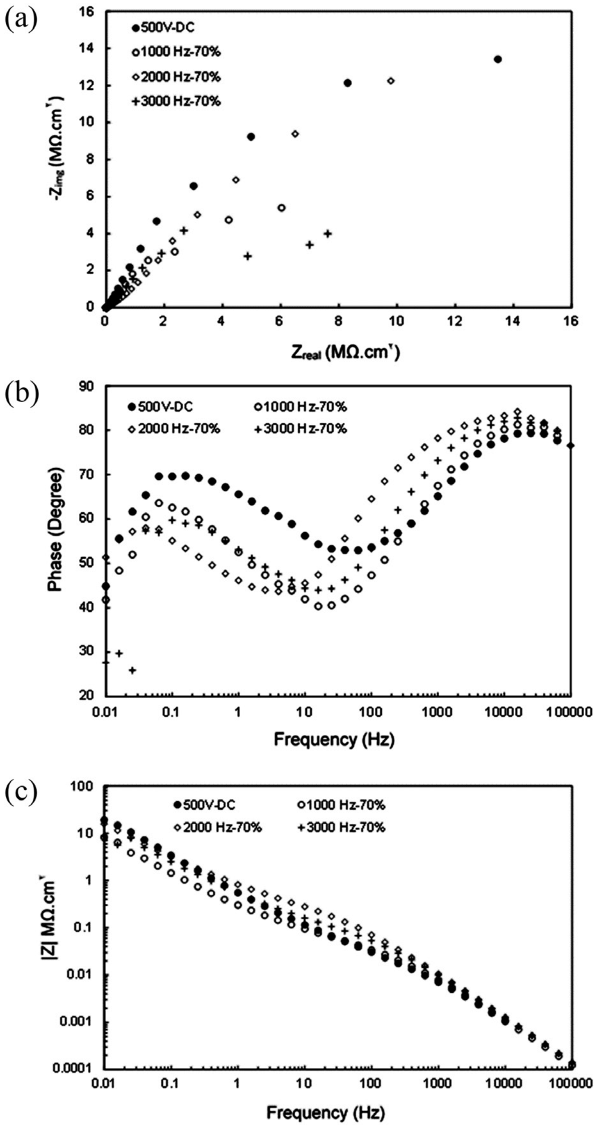

Fig. 10. (a) Nyquist, (b) Bode-phase, and (c) Bode-impedance diagrams of PEO-coated aluminum specimens by applying constant potential and one-way pulse in 30% fixed duty cycle and different frequencies in 3.5 wt% of sodium chloride after 72 h of immersion.

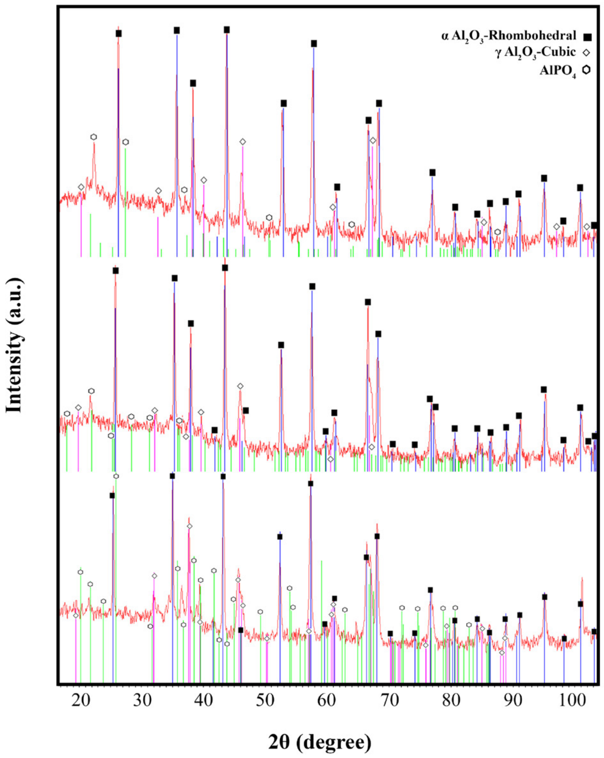

Fig. 11. XRD analysis of phosphorus element in the aluminum sample coated by applying DC-500V potential, one-way pulse potential at 2000 Hz and 70 % work cycles, and one-way pulse potential at 1000 Hz and 30% duty cycle.

Table 3.

Resistance values extracted from impedance diagrams in different immersion times in terms of cm^{2}Ω

Sample	45 min	24 h	48 h	72 h
Al-bare	200	-	-	-
DC-Coated	4E6	9.8 E3	8E6	13.5E6
1000 Hz-70%	4E6	11 E3	6.6E6	6.3E6
2000 Hz-70%	10E6	4.2 E3	10.3E6	9.7E6
3000 Hz-70%	6E5	9.2 E3	4.6E6	4.8E6
1000 Hz-30%	221.8 E6	176E3	142.8E6	174 E6
2000 Hz-30%	1.6 E6	40E3	46.3E6	46 E6
3000 Hz-30%	22.14E6	67E3	99.3E6	111E6

potential (open circuit potential) is very close to the pitting potential of the samples. In other words, by immersing uncoated samples in 3.5 wt.% sodium chloride solution, pitting corrosion occurs, which is practically not observed in the presence of the PEO coating, and there is a significant difference between corrosion potential and pitting potential. As seen, this difference between the pitting potential and the corrosion potential is greater for specimens containing coatings with a duty cycle of 30%, indicating that pitting occurs later in these specimens

Table 1 shows the results of the slope intersection of the anodic and cathodic branches for the polarization curves. As can be seen, data including corrosion current (i_{corr}) and corrosion potential (E_{corr}), slope of anodic and cathodic branches, etc. are obtained from polarization test data. As shown in Table 2, with the application of the coating, the corrosion current decreased significantly from 4.3×10^{-4} to 10^{-5}, indicating a reduction in corrosion in the presence of the coating. Comparing the corrosion current for the coated samples, the coated samples with the duty cycle of 30% shows a greater reduction in the corrosion current, which indicates the suitability of this duty cycle for the improvement of the corrosion resistance.

3.2. EIS test

Fig. 2 shows the Nyquist and Bode diagrams of aluminum in 3.5 wt% sodium chloride medium. As illustrated, the EIS diagrams of aluminum in this solution have a time constant at high and intermediate frequencies and an induction loop at low frequencies. The induction loop with a negative phase angle appears in the Bode-phase diagram (Fig. 2-b). The time constants of the high and middle frequencies are attributed to the electrochemical interactions of the aluminum surface leading to the formation of the protective layer or surface oxide layer

Table 3.
Parameters obtained from polarization corrosion test

Sample	**E_{corr} (mV)**	**i_{corr} (A.cm^{-2})**	**β_a (V/decade)**	**β_c (V/decade)**	**R_p (Ω.cm^2)**	**C.R (mm/y)**	E_{pitt} (V)	%P
Al-bare	-0.760	3.2E-4	0.013	0.239	16	3.5	~ -0.760	-
DC Coated	-0.812	3.7E-9	0.143	0.090	6562884	4E-5	-0.420	2.7E-10
1000 Hz-70%	-0.814	7.7E-8	0.142	0.093	319865.8	8.35E-4	-0.670	4.11E-9
2000 Hz-70%	-0.803	1.4E-8	0.150	0.093	1718095	62.4E-4	-0.470	5.16E-9
3000 Hz-70%	-0.763	1.6E-7	0.134	0.079	137813.2	671E-4	-0.608	7.85E-5
1000 Hz-30%	-0.667	6.8E-9	0.077	0.062	2175061	7.45E-5	-0.380	7.45E-5
2000 Hz-30%	-0.741	1.1E-9	0.108	0.077	18232089	1.2E-5	-0.465	1.17E-5
3000 Hz-30%	-0.675	1.2E-9	0.137	0.118	23540935	1.3E-5	-0.453	1.28E-5

itself. The most common theory for describing this time constant is that it appears due to the corrosion of aluminum at the metal/oxide interface and the formation of Al^{+} cations. Due to the presence of a high electric field in the oxide layer, these cations are transferred to the oxide/solution interface, where they are converted to Al^{3+} cations [21, 22].

The reason for the appearance of the induction loop for aluminum in most corrosive environments has not yet been fully identified. Adsorption of intermediate species such as hydroxyl anions, presence of a protective layer on the aluminum surface, rearrangement of surface charges at the metal/oxide interface are the most common theories in this regard [23, 24]. The results of research activities show that the polarization resistance at the emergence of the induction loop (as in Fig. 2) can be estimated by subtracting the diameter of the induction loop from the time constant diameter of high frequencies. Therefore, in Fig. 2, due to the large diameter of the induction loop compared to the time constant of high frequencies, the polarization resistance of aluminum in 3.5 wt.% sodium chloride solution is estimated to be about 200 Ω.cm^2.

Fig. 3 shows the impedance diagrams of aluminum specimens with PEO coating after 45 minutes of immersion in 3.5 wt% sodium chloride solution. As can be seen, the resulting diagrams are different from the aluminum impedance diagrams. In this case, the diagrams have a time constant at high frequencies, a time constant at medium frequencies, and an infiltration sequence at low frequencies. In the Bode diagrams (Fig. 3b and c), two time constants can be seen at high and medium frequencies. According to Nyquist diagrams, the semicircular diameter is the largest for the 2000 Hz specimen and the smallest for DC-500 V.

The observation of the impedance diagrams in Fig. 3 for the samples coated with different potential regimes clearly shows the difference between the different potential regimes. In DC potential mode (500V-DC), the phase angle starts at about 70 degrees and decreases rapidly. With the application of the pulse regime, the initial phase angle is increased to values greater than 80 degrees. In the coating applied at 1000 Hz, the phase angle in the impedance test is maintained up to a frequency of about 2000 Hz in phase angle values greater than 80. By increasing the frequency to 2000 Hz, the time constant of the high frequencies is maintained up to about 500 Hz and then decreases. Generally, in electrochemical impedance tests, the occurrence of high phase angle and its maintenance in a wide frequency range indicates the presence of continuous and dense layers on the metal surface [11, 25, 26]. In the coating applied at 3000 Hz, although the phase angle of time constant of the high frequencies started at about 80 °, it did not behave like the previous two modes (1000 and 2000 Hz). Therefore, according to the results, it seems that the coatings obtained from the pulse regime are denser than the DC coating, and the coating obtained from the pulse regime with a frequency of 2000 Hz at the beginning of the immersion period behaves much better than other coatings.

In the case of Bode module diagrams, the difference in the behavior of the uncoated aluminum sample and the coated samples in different conditions can be easily seen. According to Fig. 3, the overall strength of the aluminum sample is about 21 kΩ.cm, which is about 1000 times for coated samples. The impedance diagrams of the coated specimens under pulsed conditions and a 30% duty cycle are shown in Fig. 4. Among these samples, the frequency of 1000 Hz shows better performance than other samples, and the diameter of the Nyquist diagram of this coating is larger than that of the others. The DC sample has less resistance than the others. In the Bode-phase diagram according to Fig. 4, for a coated sample at a frequency of 1000 Hz over a large frequency range (up to a frequency of 10 Hz), the value of the phase angle is higher than 80. In the 3000 Hz coated sample, the phase angle is higher than 80 up to the frequency of about 300 Hz, but for the 2000 Hz sample and the DC-V500, the phase angle stability is not observed over a wide range. Decreasing and then increasing the phase angle is probably due to the accumulation of corrosion products in the coating pores. Comparing the diagrams of Fig. 3 with Fig. 4, it can be seen that at 24 h immersion time, samples with 70% duty cycle have better corrosion behavior and higher corrosion resistance than 30%.

The impedance diagrams of the samples after 24 hours of immersion are shown in Fig. 5. During this immersion period, the corrosion behavior of all samples is almost the same. Specimens with a frequency of 2000 Hz and 3000 Hz have larger semicircle diameters. In Bode-phase diagrams, the phase angle of all samples at the frequency of 100,000 Hz is almost the same and it suddenly decreases. It seems that during this immersion time, the corrosive solution has entered the coating pores because the phase angle gradually increases with decreasing frequency. The Bode module diagram also clearly shows that the behavior of the coated samples in pulsed mode and at frequencies of 2000 and 3000 is better than other samples.

After a 24 h of immersion, the impedance diagrams for the DC-500 V and pulse samples under the 30% duty cycle are shown in Fig. 6. During this immersion period, the behavior of the coated sample at a frequency of 1000 Hz is shown to be better than other samples. According to the Bode-phase diagram, the phase angle for the sample of 1000 Hz in a wide range of frequency (up to 1 Hz) is higher than 80 degrees. In the case of coated samples at 3000 Hz and 2000 Hz, the phase angle is constant in lower frequency range (approximately up to 900 Hz). In the case of the DC-V500 coated specimen, the phase angle decreases rapidly. This trend can be clearly seen in the Bode-module diagram.

The impedance diagrams during the 48-hour immersion period are shown in Fig. 7. The corrosion behavior of all samples is similar, and the process is similar to that of the 24-hour immersion. During this immersion period, the phase angle decreases immediately. In the Bode-module pattern, the process is similar to the 24-hour immersion time. In the 30% duty cycle, after 48 hours of immersion, the impedance test information is extracted and the results are shown in Fig. 8. The behavior of the samples is similar to that of 24 hours, and for the sample coated at 1000 Hz, the phase angle value is constant over a wide frequency range (approximately up to 0.5 Hz) and is above 80 °. For the 3000 Hz coated sample, the phase angle is also statically stable and above 80, but for the other 2 samples (the 2000 Hz coated sample and the DC-500 V coated sample), the phase angle suddenly decreases.

After immersion for 72 hours, the results of the impedance test for the DC-500 V potential regime and the pulse potential regime at the frequencies of 1000 Hz, 2000 Hz, and 3000 Hz are plotted as Nyquist and Bode diagrams in Fig. 9. According to the images, the corrosion process has not changed noticeably compared to the previous immersion times. Nevertheless, the corrosion resistance of the coating has increased dramatically. The results of the impedance test after 72 hours of immersion for the DC-500 V sample and pulse samples with a 30% duty cycle are shown in Fig. 10. Similar to the previous immersion time, the coated sample at a frequency of 1000 Hz has the phase angle frequency of about 85 degrees in wider frequency range. According to the Bode-modulus diagram, almost all coated samples show good capacitive behavior in the pulsed mode. In the case of the DC-500V, there is some difference with the capacitive behavior, but in general, the corrosion resistance has increased in all samples.

Generally, according to the impedance diagrams, the corrosion resistance of the coated specimens increases significantly over the immersion time. Therefore, after 72 hours, the resistance increased to an average of about 10 MΩ [27, 28]. Regarding the pulse potential application regime, the corrosion behavior of the samples in the duty cycle of 30% is better than 70%, which can be related to the thickness of the coatings and their porosity percentage [29]. Therefore, by increasing the thickness and decreasing the porosity, the invading chloride ion is able to destroy the coating at a slower rate. The value of resistance, R_p, at different times is summarized in Table 3. In the analysis of the impedance diagrams, other parameters can be also extracted and the corrosion resistance performance of the coating can be examined from other aspects, which will be explained below.

3.3. XRD analysis

To investigate the corrosion behavior, it is better to study the XRD analysis of the coating. For this purpose, the coatings created in the DC potential regime and optimized coatings in terms of corrosion resistance and morphology have been analyzed for further investigation. And the results are shown in Fig. 11. In the PEO coatings, the α phase provides the wear resistance of the coating and the γ phase provides the corrosion resistance. In the XRD images, the coated samples generally show three types of peaks. Fig. 11 shows the sample coated under the DC potential regime under 500 V. It has a lower γ value than the other two samples. This sample has a large amount of α-Al_2O_3 phase and about 30% of it is composed of the γ-Al_2O_3 phase. Also in this composition, some amounts of aluminum phosphate have been observed.

In the samples coated under the pulse voltage regime at the frequency of 2000 Hz and the operating cycle of 70 % (Fig. 11), the amount of aluminum phosphate composition is almost the same as the previous sample. In this sample, α-Al_2O_3 decreases compared to the previous sample and the amount of γ-Al_2O_3 has been increased. In Fig. 11, which is related to the coating at 1000 Hz and 30% duty cycle, the percentage of γ phase reaches about 50%, which is in good agreement with the corrosion diagrams and their corrosion resistance has been increased.

In Fig. 11, there is some aluminum phosphate compound. By increasing the γ phase, the amount of this phase has decreased. It is worth noting that the γ phase is in the form of the tetragonal type. γ-Al_2O_3, regardless of its tetragonal distortions, has always been described as having a cubic spinel structure and a spatial group of Fd3m. Paglia et al. [29] showed that there is also a tetragonal type for $\gamma-Al_2O_3$ through neutron diffraction and TEM analysis. In Fig. 11, the XRD result of the 30% sample at 1000Hz is presented, which confirms the presence of this phase with a tetragonal structure in the coating too. One of the interesting points in XRD diagrams is the presence of aluminum phosphate phase in the coating, which may be one of the factors that increase the corrosion resistance of PEO coatings. To confirm the presence of aluminum phosphate phase, the distribution of phosphorus under the substrate was examined.

4. Conclusions

In this research, aluminum was coated by the PEO method in the optimal electrolyte composition of 10 g/l tetra sodium pyrophosphate, 3 g/l sodium aluminate and 3 g/l potash (KOH). The results are summarized as follows:

1. In general, according to the impedance diagrams, the corrosion resistance of the coated specimens increases greatly over the immersion time. After 72 hours, the resistance increased to an average of about 10 MΩ.
2. In the case of pulse potential regime, the corrosion behavior of the samples in the work cycle of 30% is better than 70%, which can be related to the thickness of the coatings created and their porosity.
3. In this way, by increasing the thickness and decreasing the porosity, the invading chloride ion is able to destroy the coating at a slower rate.

REFERENCES

[1] I. Tajzad, E. Ghasali, Production methods of CNT-reinforced Al matrix composites: a review, Journal of Composites and Compounds 2(1) (2020) 1-9.

[2] K. Zhang, H.W. Jang, Q. Van Le, Production methods of ceramic-reinforced Al-Li matrix composites: A review, Journal of Composites and Compounds 2(3) (2020) 77-84.

[3] F. Sharifianjazi, M. Moradi, A. Abouchenari, A.H. Pakseresht, A. Esmaeilkhanian, M. Shokouhimehr, M.S. Asl, Effects of Sr and Mg dopants on biological and mechanical properties of SiO2–CaO–P2O5 bioactive glass, Ceramics International (2020).

[4] B. Ghorbanian, S.M.M. Khoie, Formation of vanadium carbide with the plasma electrolytic saturation method (PES) and comparison with Thermo Reactive diffusion method (TRD), Acta Metallurgica Slovaca 22(2) (2016) 111-119.

[5] S. Nasibi, K. Alimohammadi, L. Bazli, S. Eskandarinezhad, A. Mohammadi, N. Sheysi, TZNT alloy for surgical implant applications: A systematic review, Journal of Composites and Compounds 2(3) (2020) 62-68.

[6] B. Kasalica, M. Petković-Benazzouz, M. Sarvan, I. Belča, B. Maksimović, B. Misailović, Z. Popović, Mechanisms of plasma electrolytic oxidation of aluminum at the multi-hour timescales, Surface and Coatings Technology (2020) 125681.

[7] T. Kikuchi, T. Taniguchi, R.O. Suzuki, S. Natsui, Fabrication of a plasma electrolytic oxidation/anodic aluminum oxide multi-layer film via one-step anodizing aluminum in ammonium carbonate, Thin Solid Films 697 (2020) 137799.

[8] W. Liu, C. Blawert, M.L. Zheludkevich, Y. Lin, M. Talha, Y. Shi, L. Chen, Effects of graphene nanosheets on the ceramic coatings formed on Ti6Al4V alloy drill pipe by plasma electrolytic oxidation, Journal of Alloys and Compounds 789 (2019) 996-1007.

[9] L. Famiyeh, H. Xiaohu, Improving Corrosion Resistance and Mechanical Properties of Aluminum and its Alloys via Plasma Electrolytic Oxidation (PEO) for Aerospace Applications: A Review.

[10] R. Barik, J. Wharton, R. Wood, K. Stokes, R. Jones, Corrosion, erosion and erosion–corrosion performance of plasma electrolytic oxidation (PEO) deposited Al_2O_3 coatings, Surface and coatings technology 199(2-3) (2005) 158-167.

[11] L. Pezzato, M. Rigon, A. Martucci, K. Brunelli, M. Dabalà, Plasma Electrolytic Oxidation (PEO) as pre-treatment for sol-gel coating on aluminum and magnesium alloys, Surface and Coatings Technology 366 (2019) 114-123.

[12] V. Dehnavi, B.L. Luan, D.W. Shoesmith, X.Y. Liu, S. Rohani, Effect of duty cycle and applied current frequency on plasma electrolytic oxidation (PEO) coating growth behavior, Surface and Coatings Technology 226 (2013) 100-107.

[13] S.S. Kamble, A. Gunasekaran, S.A. Gawankar, Sustainable Industry 4.0 framework: A systematic literature review identifying the current trends and future perspectives, Process Safety and Environmental Protection 117 (2018) 408-425.

[14] J. Parameswaranpillai, S.K. Sidhardhan, P. Harikrishnan, J. Pionteck, S. Siengchin, A.B. Unni, A. Magueresse, Y. Grohens, N. Hameed, S. Jose, Morphology, thermo-mechanical properties and surface hydrophobicity of nanostructured epoxy thermosets modified with PEO-PPO-PEO triblock copolymer, Polymer

Testing 59 (2017) 168-176.

[15] J. Curran, T. Clyne, Thermo-physical properties of plasma electrolytic oxide coatings on aluminium, Surface and Coatings Technology 199(2-3) (2005) 168-176.

[16] V.T. Targhi, H. Omidvar, S.M.M. Hadavi, F. Sharifianjazi, Microstructure and hot corrosion behavior of hot dip siliconized coating on Ni-base superalloy IN-738LC, Materials Research Express 7(5) (2020) 056527

[17] A. Shirani, T. Joy, A. Rogov, M. Lin, A. Yerokhin, J.-E. Mogonye, A. Korenyi-Both, S.M. Aouadi, A.A. Voevodin, D. Berman, PEO-Chameleon as a potential protective coating on cast aluminum alloys for high-temperature applications, Surface and Coatings Technology (2020) 126016.

[18] J. Guest, S. Papavinasam, N.S. Berke, S. Brossia, Corrosion Monitoringand Measurement.

[19] Y. Rao, Q. Wang, D. Oka, C.S. Ramachandran, On the PEO treatment of cold sprayed 7075 aluminum alloy and its effects on mechanical, corrosion and dry sliding wear performances thereof, Surface and Coatings Technology 383 (2020) 125271.

[20] T. Arunnellaiappan, S. Arun, S. Hariprasad, S. Gowtham, B. Ravisankar, N. Rameshbabu, Fabrication of corrosion resistant hydrophobic ceramic nanocomposite coatings on PEO treated AA7075, Ceramics International 44(1) (2018) 874-884.

[21] E. Parfenov, A. Yerokhin, A. Matthews, Impedance spectroscopy characterisation of PEO process and coatings on aluminium, Thin solid films 516(2-4) (2007) 428-432.

[22] A. Bahramian, K. Raeissi, A. Hakimizad, Characterizing of DC-Plasma Electrolytic Oxidation (PEO) Coatings on 7075 Aluminum Alloy.

[23] V.T. Targhi, H. Omidvar, F. Sharifianjazi, A. Pakseresht, Hot Corrosion Behavior of Aluminized and Si-modified Aluminized Coated IN-738LC Produced by a Novel Hot-dip Process, Surfaces and Interfaces (2020) 100599.

[24] E. Akbari, F. Di Franco, P. Ceraolo, K. Raeissi, M. Santamaria, A. Hakimizad, Electrochemically-induced TiO2 incorporation for enhancing corrosion and tribocorrosion resistance of PEO coating on 7075 Al alloy, Corrosion Science 143 (2018) 314-328.

[25] H.P. Hack, J.R. Scully, Defect area determination of organic coated steels in seawater using the breakpoint frequency method, Journal of the Electrochemical Society 138(1) (1991) 33.

[26] V. Egorkin, S. Gnedenkov, S. Sinebryukhov, I. Vyaliy, A. Gnedenkov, R. Chizhikov, Increasing thickness and protective properties of PEO-coatings on aluminum alloy, Surface and coatings Technology 334 (2018) 29-42.

[27] I.Š. Rončević, Z. Grubač, M. Metikoš-Huković, Electrodeposition of hydroxyapatite coating on AZ91D alloy for biodegradable implant application, Int. J. Electrochem. Sci 9 (2014) 5907-5923.

[28] A. Hakimizad, K. Raeissi, M.A. Golozar, X. Lu, C. Blawert, M.L. Zheludkevich, The effect of pulse waveforms on surface morphology, composition and corrosion behavior of Al2O3 and Al2O3/TiO2 nano-composite PEO coatings on 7075 aluminum alloy, Surface and Coatings Technology 324 (2017) 208-221.

[29] G. Paglia, C. Buckley, A. Rohl, B. Hunter, R. Hart, J. Hanna, L. Byrne, Tetragonal structure model for boehmite-derived γ-alumina, Physical Review B 68(14) (2003) 144110.

Journal of Composites and Compounds 2 (2020) 138-146

Available online at www.jourcc.com

Journal homepage: www.JOURCC.com

Journal of Composites and Compounds

The rechargeable aluminum-ion battery with different composite cathodes: A review

Leyla Saei Fard[a]*, Naeimeh Sadat Peighambardoust[b], Ho Won Jang[c], Alireza Dehghan[d],

Niloufar Nehzat Khosh Saligheh[e], Marjan Iranpour[f], Mitra Isvand Rajabi[g]

[a] Department of Organic and Biochemistry, Faculty of Chemistry, University of Tabriz, Tabriz 5166416471, Iran
[b] Koç University Boron and Advanced Materials Applications and Research Center (KUBAM), Sariyer, Istanbul, 34450, Turkey
[c] Department of Materials Science and Engineering, Seoul National University, Seoul 08826, Republic of Korea
[d] Department of Research and Development, Applied research center of the geological survey of Iran, Alborz, Iran
[e] Shomal University, Amol, Mazandaran, Iran
[f] Department of Agricultural Machinery Mechanics, Univesity of Tehran, Alborz, Iran
[g] Islamic Azad University, Dezful Branch, Dezful, Khuzestan, Iran

ABSTRACT

Digital cameras, laptop computers, cellular phones, as well as many portable electronic devices require batteries for powering. Based on the electrolyte type, electrolytic batteries can be categorized into solid-based, liquid-based, and ionic-based batteries. Aluminum ion batteries (AIBs) have some promising properties such as low cost, high safety, and high specific volumetric capacity. Nevertheless, in order for AIBs to be extensively used, developing novel electrode materials possessing high energy density is required. This is mainly dependent on the cathode materials. However, these cathode materials have some drawbacks such as structural decomposition, low battery capacity, low discharge voltage, and volume expansion resulting from the intercalation of large-sized ions. Therefore, future research might concentrate on the investigation of cheaper electrolyte and novel cathode materials for enhancement of energy density and working voltage. This review focuses on the recently developed cathodes, particularly, composite cathode materials, including graphite, CuS, V_2O_5, Li_3VO_4@C, VS_4/rGO, and Ni_3S_2/graphene.

ARTICLE INFORMATION

Article history:
Received 15 August 2020
Received in revised form 5 September 2020
Accepted 17 September 2020

Keywords:
Liquid electrolyte
Solid electrolyte
Ionic electrolyte
Aluminum-ion battery
Composite cathodes

Table of contents

1. Introduction

Electricity supply enhances productivity and access to principal services [1]. Powering many electronic devices such as digital cameras, laptop computers, and cellular phones have raised the demand for batteries. Rapid response and long operation times times are favored for the development of high-power batteries with high energy densities. NiCd and Ni metal hydride batteries have been principally utilized [2]; Gaston Plante first developed lead-acid battery in 1859. Meanwhile, the second generation of batteries with long cycle life, high energy density, high power density has been investigated in the chemical power industry [3]. A novel battery for electronic vehicles was developed by Thomas A. Edison in 1900 and finally, he patented his Ni-iron battery in 1901 in

---

* Corresponding author: Leyla Saei Fard; E-mail: leylasaiifard@yahoo.com

https://doi.org/10.29252/jcc.2.3.5

the USA. This battery is regarded as his most commercially successful product. To fabricate the best commercial battery with the right material combination, he spent over 10 years, performed more than 50,000 experimental investigations, and withdrew the first fabricated version form the market [4].

The most extensively used batteries for electrochemical energy storage since the early 1990s are lithium-ion batteries consisting of a lithiated metal oxide cathode, a liquid electrolyte, and a carbonaceous anode [5]. Their popularity is due to some inherent advantages such as no environmental toxicity, no memory effect, and a long life span. However, by the dramatic increase in the energy storage demand, we are dealing with the limited source of lithium over the next decades [6]. Many solid electrolytes such as lithium phosphorus oxynitride (Lipon), $Li_7La_3Zr_2O_{12}$, Li_4SnS_4, Li_3PS_4, and $Li_{10}GeP_2S_{12}$, possess a voltage window beyond 5 V, therefore, their decomposition does not occur under anodic current. Moreover, there is a minimal possibility of the dissolution of transition metals into the electrolyte when a solid electrolyte is used. Contrary to carbonate electrolytes, the majority of ceramic solid electrolytes are intrinsically inflammable [7].

Room temperature ionic liquids (RTILs) are attracting attention as green solvents. These materials are being used for new applications as electrolytes for electrochromic windows, electrochemical mechanical actuators, and numerical displays with dye-sensitized solar cells, light-emitting electrochemical cells, conducting polymers, and other devices. These new materials are revolutionizing various technological and scientific areas such as the battery field [2].

One of the post-lithium batteries is the aluminum-ion batteries (AIBs) that were first introduced by Tech Vision Electronics in 2017. It has been reported that the number of patents in this field showed a 29% growth from 2010 to 2016 while the patent filings began only in 2013 [8]. The reason for significant interest in AIBs is the abundance of Al and its even distribution in the earth [9, 10]. Additionally, a very high capacity of up to 8.05 Ah/cm^3 and 2.98 Ah/g can be obtained using multivalent metal ions transmitting internally in the AIBs [11]. During the electrochemical reaction, three-electron transfer is usually involved in an Al-based redox couple, leading to higher energy capacities and energy density [12].

In this article, we first focus on the description of the electrolyte batteries, their benefits, and their limitations. Then, batteries with ionic electrolyte, solid electrolyte, and liquid electrolyte are reviewed. Finally, the current state of knowledge in the field of AIBs with different composite cathodes is summarized [13].

2. Electrolytic batteries

Electrolytic batteries consist of the cathode, anode, and electrolyte. Oxides formed on metals provide passive layers on the surfaces of metals, which make them stable in contact with gas phases such as air or liquid phases such as electrolyte solutions. This also happens for the ion battery electrodes [14]. Therefore, both anode and cathode materials used in ion batteries do not show stability with respect to electrolyte solutions [15].

2.1 Batteries with liquid electrolyte

Recently, there have been many papers concentrating on the performance improvement of Li/S batteries [16, 17]. Nevertheless, a few research reports mentioned that the dissolution of lithium polysulfide in the lithium/sulfur cell has a significant effect on the performance of the cell. Polysulfides (PS) are the sulfur reduction intermediates [18-20]. Based on the general formula of $Li_2Sn \rightarrow m/8S_8 + Li_2S_{n-m,}$ a series of complicated disproportionation occur for PS in the solution. Therefore, low-order PS and the less soluble sulfur are formed leading to inactivation when it deposits into the pores of the separator or precipitates out of the liquid electrolyte [21]. The literature shows that by the incorporation of an ionic liquid or a solid salt of quaternary ammonium into the liquid electrolyte, the disproportionation of polysulfide intermediate can be suppressed [22]. This approach enhances cell capacity retention, but the redox shuttle of PS cannot be suppressed. Additionally, $LiNO_3$ can effectively suppress the PS redox shuttle and increase the charging efficiency of the cell; however, this effect is vanished by time due to the gradual consumption of $LiNO_3$ on the Li anode. It has also been observed that the rate capability of the upper voltage plateau is better compared to the lower voltage plateau because the solid-to-liquid phase transition is more favorable [23].

It has been indicated that room-temperature lithium/sulfur cells with organic liquid electrolytes use very low active material [24]. Various investigations have investigated the electrochemical properties of these cells with different electrolytes such as polymer/gel electrolytes [25-30], 1,2-dimethoxyethane (DME) [31], tetra (ethylene glycol) dimethyl ether (TEGDME) [26, 32-35], carbonate systems [36, 37], 1,3-dioxolane (DIOX) [31, 33], and tetrahydrofuran (THF). One of the promising organic solvents for room-temperature lithium/sulfur cells is tetramethylene glycol dimethyl ether (TEGDME). This gel/polymer or liquid electrolyte solvent provides a high first discharge capacity of more than 1200 mAh g^{-1} [27, 34, 35].

Cycle performance and discharge capacity of room-temperature lithium/sulfur cells containing polymer electrolytes and single/binary liquid electrolytes with $LiCF_3SO_3$ (1 M) were studied [38]. The cycle property and the cell's first discharge capacity were shown to be largely dependent on the liquid electrolyte content [39]. According to the investigations, at about 450 mAh g$^-$1, a medium containing electrolyte around 12 µl yields the stable and optimal cycle performance. Cycle performance of cells using different electrolytes including 1,2-dimethoxyethane/di(ethylene glycol)dimethyl ether (DEGDME) (1:1, v/v), TEGDME/DIOX (1:1, v/v), and TEGDME showed that the TEGDME-based mixed electrolytes had better results. An increase from 386 to 736 mAh g^{-1} was observed in the initial discharge capacity that stabilized the cycle properties by adding toluene 5 (vol.%) to TEGDME owing to the decrease in Li metal interfacial resistance [40]. In this study, cycle performance, Li metal interfacial resistance, and ionic conductivity in room-temperature lithium/sulfur cells containing TEGDME/DIOX polymeric electrolyte and poly(vinylidene fluoride) (PVDF) microporous membrane were evaluated [41]. Studies revealed the better performance of the liquid electrolyte in comparison with the polymer electrolyte [30].

Although advancements in the field of lithium/sulfur cells with the liquid electrolyte are significant challenges remain. The operation of these cells requires the dissolution of polysulfides and elemental sulfur in the organic liquid electrolytes [42]. PS and sulfur are electronically and ionically conductive resistance, therefore, their redox takes place on the conductive carbon surface in contact with the electrolyte [43]. Hence, the cells are considered as liquid electrochemical cells. However, two negative charges are carried by polysulfide anions, and it is required to maintain electric drag between the two electrodes during the cell function [44]. It has been proven that the outward diffusion of the dissolved polysulfide from the cathode can be effectively suppressed by sulfur-carbon composites [45]. However, as a result of the incorporation of extra electrochemically inactive carbon, the improvement is accompanied by the reduction of the energy density. Although a large amount of carbon is introduced by these composites, the lithium/sulfur cell is still a liquid cell [46]. The difference is that the absorption of the dissolved PS occurs on the carbon pores and surfaces. According to the electrical drag effect of polysulfide, protecting the lithium anode against the corrosive attack of the dissolved polysulfide and the redox shuttle occurs [47]. PS dissolution and the determination of the power capability of the cells

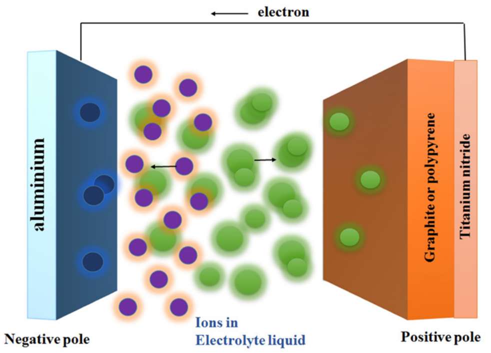

Fig. 1. Schematic illustration of batteries with liquid electrolyte.

are dependent on the liquid electrolyte. A facile approach to suppress the polysulfide redox shuttle and improve the Li deposition morphology is to incorporate additives to the electrolyte [48]. The low coulombic efficiency of lithium cycling could be solved by adding $LiNO_3$, however, it undergoes gradual consumption on the Li anode and cathode and its strong oxidative property causes safety issues [49].

The advancement of Li/S technology needs safer and more effective additives. As a result of the high reactivity of PS anionic radicals, the chemical compatibility for selecting the cell materials such as cathode's binder, salt, and electrolyte solvent should be considered as a high priority [50]. Regardless of the taken approach, it is necessary for the cathode to possess a relatively high loading and content of sulfur to ensure the high energy density of the cell [17].

Different liquid electrolytes with high ionic conductivity including dimethyl carbonate (DMC)/ethylene carbonate (EC), propylene carbonate (PC), and EC/PC have been utilized in sodium-ion batteries [51-54]. Although sulfur electrodes are able to yield good ionic conductivity, the investigations about using these electrodes for Na batteries with liquid electrolytes are not extensive. At ambient temperature, a liquid electrolyte sodium ionic conductivity composed of $NaCF_3SO_3$ salt and TEGDME is 3.9×10^{-3} S cm^{-1}, and it could be utilized for room-temperature sodium-sulfur batteries. Two regions are observed in the discharge curve: the first region has a decreasing trend from 2.23 to 1.66 V and the second region is a plateau at 1.66 V. The first discharge capacity of sodium-sulfur cells with liquid electrolytes [55] at room temperature (538 mAh g^{-1}) is lower compared to high-temperature counterparts. After a sharp decrease in the second cycle, the discharge capacity is stabilized at 250 mAh g^{-1} up to the 10th cycle, and Na_2S_2 and Na_2S_3 are the final discharge products. Sodium or sulfur polysulfides are dissolved into the electrolyte and sodium sulfides are reduced irreversibly to elemental S at full charge leading to a decrement of discharge capacity [56]. A schematic illustration of batteries with liquid electrolytes is shown in Fig. 1.

2.2 Batteries with solid electrolyte

Inorganic solid electrolytes are used in all-solid-state secondary batteries. These batteries are attracting attention due to their ionic conductivities and better safety compared to conventional batteries [57]. Besides conductivity, the enhancement of cycle performance and the energy density are highly affected by the mechanical characteristics of solid electrolytes [58]. High ionic conductivities of some new solid electrolytes including Na_3PS_4, $Li_{10}GeP_2S_{12}$, and $Li_3P_7S_{11}$ have been reported. The ionic conductivities of some of them are even close to those of liquid electrolytes [59]. The current issue regarding solid electrolytes is the improvement of their electrochemical and electrical properties [60]. The mechanical characteristics of these electrolytes such as densification behavior and elastic modulus are important factors for the development of all-solid-state batteries practically, however, few studies are focusing on the mechanical characteristics of solid electrolytes with high-ion-conductivity [61]. All solid-state Li$^+$ ion battery illustration is seen in Fig. 2.

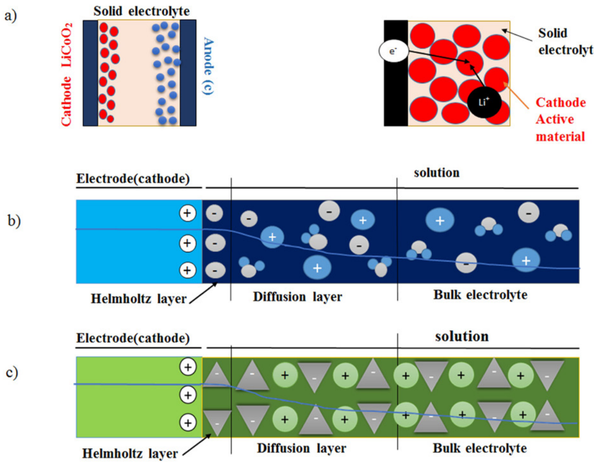

Fig. 2. Schematic illustration of (a) all-solid-state Li+ ion battery (b) a typical solid-liquid interface, and (c) positive electrode-solid electrolyte interfaces, in which cations (green circles) and anions (gray triangles) form their networks and the anions are less mobile.

Due to electrolyte decomposition upon the first cycle, a protecting layer, known as "solid electrolyte interphase (SEI)", is generated on the negative electrode of Li-ion batteries. The quality of the SEI highly influences battery performance, safety, exfoliation of graphite, rate capability, and irreversible charge loss [62]. Thus, this is important to comprehend the composition and actual nature of SEI. By understanding the way each component influences the performance of the battery and the chemistry of the SEI formation, it is possible to tune SEI to improve battery performance [63]. Properties of SEI including morphology, compactness, thickness, and composition have significant effects on battery performance. A characteristic of SEI is irreversible charge loss (ICL) that occurs upon the first cycle, which is the result of the reduction of the solvent and SEI formation [58]. Moreover, the SEI ability to change the active material surface to a passive one can affect self-discharge, which is a detrimental process during storage. Therefore, SEI determines the shelf-life of a battery [64]. As SEI may evolve and/or dissolve during cycling, for good cycling life in the battery, stable and effective SEI is necessary [65] and its necessity is more significant at a deeper depth of discharge and during high-rate cycling [66]. SEI components show high sensitivity to temperature, therefore, they affect the low- and high-temperatures performance of the battery [67]. Nevertheless, SEI mostly influences the safety of the battery [68-70].

The dissolution of transition metals into the electrolyte could be minimized by solid electrolytes. In contrast to carbonate electrolytes, most ceramic solid electrolytes are inflammable, and the compatibility between Li and various solid electrolytes and Li metal is likely to create dendrites during cycling due to the mechanical robustness of the electrolytes [71]. In comparison with liquid electrolyte Li batteries, solid-state batteries have lower power densities. This is the result of limited kinetics of the electrodes, the compatibility of the electrode/electrolyte interface, and the solid electrolyte low ionic conductivity [72]. Recently, the development of high ionic-conductive solid electrolytes has made the production of solid-state Li batteries possible with a power performance similar to liquid-electrolyte batteries. However, there is a great challenge about interfacial instability between the electrolyte and electrode in these batteries. For most solid-state Li batteries, it is required to properly engineer the interfaces between electrode and electrolyte to yield good cycling performance [73, 74]

Owing to a moderate Young's modulus as well as low bond energy, sulfide solid electrolytes have good processability and high ionic conductivity. Room-temperature pressure sintering can be used for the fabrication of sulfide solid electrolytes. All-solid-state batteries, therefore,

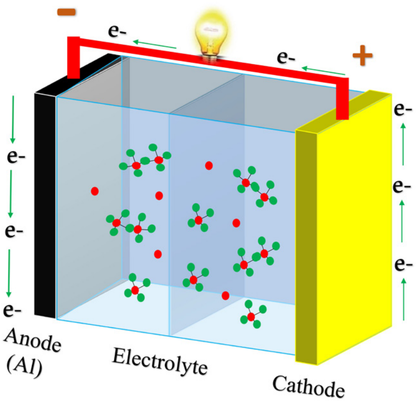

Fig. 3. Schematic illustration of batteries with ionic electrolyte.

can highly benefit from sulfide solid electrolytes. Some sulfide solid electrolytes have yielded conductivities comparable to practical Li-ion batteries [75]. It is necessary to obtain the ideal mechanical characteristics of all-solid-state batteries and fabricate novel solid electrolytes that have enhanced mechanical properties [61].

2.3 Batteries with ionic electrolyte

N-methyl-N-butyl-piperidinium bis(trifluoromethanesulfonyl imide (PP14-RTIL)) was prepared as a new room-temperature ionic electrolyte for lithium/sulfur cells. The cyclic voltammetry of this new electrolyte exhibited an extant potential window of 5.2 to 0.15 V as well as electrochemical stability, which make it proper for Li-S electrodes [76]. The viscosity of water is 0.89 cP at room temperature, while this value for ionic liquids is in the range of 30–50 cP and sometimes several hundreds of cP. When [Li+][X-] salt is added to the neat ionic liquid of [A+][X-], the formed $[Li+]_m[A+]_n[X-]_{m+n}$ system has even higher viscosity [77]. Due to the high viscosity of ionic liquids, there are some problems with their handling. Electrodes involve active materials, a polymer binder, and an electron conductor (acetylene black). The electrolyte fills the volume between particles [15]. Pure ionic liquids show low conductivities and high viscosity. The addition of an organic dipolar aprotic solvent can reduce the viscosity of neat ionic liquids. A schematic illustration of batteries with ionic electrolytes is observed in Fig. 3. Diaw et al. [78] studied conductivities and viscosities of 1-butyl-4 methyl-pyridinium (Py^+) or 1-butyl-3-methylimidazolium (IMI^+) associated with hexafluorophosphate (PF^{6-}) or tetrafluoroborate (BF^{4-}) anions mixed with butyrolactone (BL) or acetonitrile (ACN) in the presence of lithium hexafluorophosphate or lithium tetrafluoroborate [79]. The mixture of organic solvents with pyridinium and imidazolium are relevant electrolytes for electrochemical systems. It was shown that the viscosity and conductivity of the electrolytes are higher than those of pure ionic liquids. They proposed that these electrolytes are promising for various electrochemical applications due to their low vapor pressure and good thermal stability [75].

The liquids in batteries make special pack sealing by themselves that is necessary for the prevention of liquid leakage and explosive volatiles. Moreover, reactions of lithium metal with liquid solvents lead to poor battery performance. The electrolyte ionic conductivity often limits high power [80]. Recently, ionic liquids with organic cations have been offered as electrolytes [81-83]. Vapor pressure of ionic liquids is negligible compared to conventional liquid solvents. However, Li batteries need the transportation of Li^+ cations between the cathode and anode. Therefore, doping with a suitable LiX salt is required for ionic liquids [81, 82]. Then the doped ionic liquid is incorporated in a thin, flexible membrane to be applicable for a battery electrolyte. Within the membranes, the Li^+ cation transport mechanism is changed by the presence of an ionic liquid. This is an important issue because the conductivity can increase beyond the existing limits for dry polymer electrolytes offering promising possibilities for the long-sight in high energy lithium-metal-polymer batteries [2].

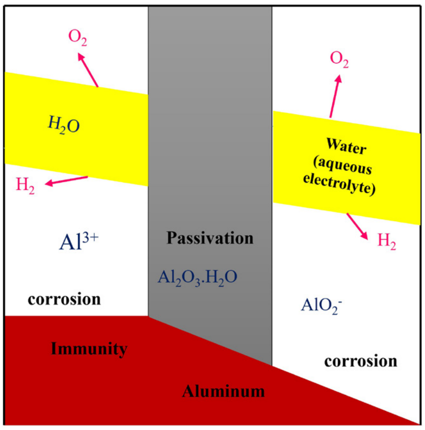

Fig. 4. Schematic of room-temperature corrosion behavior of aluminum in water.

3. Types of aluminum-ion batteries according to different cathodes

3.1. Aluminum-ion batteries

Aluminum is one of the most abundant metals in the earth's crust [84-86]. Al may offer considerable safety enhancement and cost-saving in comparison with its counterparts due to its easier handling and lower reactivity. Furthermore, aluminum is one of the ideal elements that can be used in rechargeable batteries owing to its small electrochemical equivalent around 0.336 g Ah^{-1} and highly negative redox potential around $\approx$1.676 V vs. standard hydrogen electrode [87]. On the other hand, there have been several issues in the past such as the effect of absence of discharge voltage plateaus on the capacitive behavior [69, 88] low discharge voltage [89], and the disintegration of disintegration [90, 91]. The surface of Al is easily oxidized and inert Al_2O_3 oxide films are generated that decreases the Al electrode potential rapidly. Al is an amphiprotic metal with the chemical activity that tends to react with aqueous-medium. This explains why rechargeable aluminum-ion-batteries have not been industrialized [92, 93].

In recent works, some new electrode materials have been explored such as Prussian blue analogues (PBAs) [94], polymers [95], fluorinated natural graphite [96], TiO_2 [97, 98], and V_2O_5 [99], VO_2 [100], graphitic-foam, carbon, and sulfide materials [101, 102]. According to several studies, Al ions intercalate into or de-intercalate from the electrode materials as complex ions or they can have a redox reaction with active materials of the positive electrode [3, 103].

Al deposition occurs at potentials that are beyond the water stability region, therefore, using Al as a negative electrode in the presence of an aqueous electrolyte in a secondary aluminum-ion battery is not feasible [104]. In these potentials, decomposition of the electrolyte occurs and ion transport gets disrupted [105]. Calculated theoretical specific energies and specific energies in real systems have reached 1,090 Wh/kg and 200 Wh/kg, respectively, which both are far less than the value for pure aluminum. By using a mixing system and a complex electrolyte supply, such batteries are utilized in the marine sector [106]. Because the Al electrode inherently generates hydrogen, it is required to design batteries with a different design in which metallic Al is not used [107]. Holland et al. [108] used TiO_2 as the negative electrode, copper-hexacyanoferrate (CuHCF) as the positive electrode, and an electrolyte of KCl and $AlCl_3$

aqueous solution. Fig. 4 shows the schematic of the room-temperature corrosion behavior of aluminum in water. According to the authors, the Al^{3+} ions are the mobile species, and the obtained discharge voltage measured to be 1.5 V. Furthermore, at a specific power of 300 W/kg, the specific energy was reported to be 15 Wh/kg and for over 1,750 cycles, energy efficiency remained above 70%. There is a limitation for the overall reachable energy density in these cells due to using a negative electrode that consists of other materials than Al [4].

Al-air batteries consist of a negative electrode of Al, a positive electrode that enables transportation and reduction of oxygen, and an electrolyte consisting of alkaline solutions of sodium chloride (NaCl), potassium hydroxide (KOH), or sodium hydroxide (NaOH) [109]. Rechargeable batteries with non-aqueous electrolytes like ionic liquids have been also reported. These batteries have some problems such as short shelf life, lack of rechargeability, sluggish discharge kinetics, a high self-discharge rate, and the corrosion of aluminum [38]. In the case of the passivation regime, the cell voltage and cell efficiency decreased due to the oxide layer on the Al electrode surface [110].

Secondary Al batteries usually consist of a negative electrode of Al and a non-aqueous ionic liquid electrolyte based on chloroaluminate [111]. Since 1988, these electrolytes have gained attention, when imidazolium chloride and $AlCl_3$ were utilized because of comparably wide electrochemical windows and their low vapor pressure which enable plating efficiencies and highly reversible stripping of aluminum. The same electrolyte was used for secondary aluminum batteries in subsequent studies due to the high success in Li-ion batteries [112].

For using the full potential of the Al-ion batteries, the negative electrode should be composed of pure Al. On the other hand, the protective oxide layer formed on the surface of this metal has an adverse effect on battery performance [113]. This is because the reversible electrode potential would not be obtained and there would be a delay in the activation of the electrode [105]. The enhancement of the electrode potential leads to accelerated corrosion in the liquid electrolyte (parasitic corrosion reaction occurs leading to the consumption of the electrode and evolution of hydrogen) and less shelf life. This happens for an Al battery with a liquid electrolyte. To reduce the parasitic corrosion of the Al electrodes, the deposition of other oxide layers and additions to the liquid electrolytes have been practiced [114]. Some research has reported the advantages of the oxide layer namely the restriction of strong surface corrosion and the growth of crystalline Al dendrites resulting in the improvement of the cycling stability of Al batteries [4].

In solid electrolytes, the Al electrode surface is of great importance. Before joining to the solid electrolyte, the oxide surface layer should be removed from the Al electrode surface. In an alternative way, a physical vapor deposition technique can be used for Al deposition or liquefied aluminum infiltration in the solid electrolyte [115]. Due to environmental benignity, low cost, and high energy density, Al is considered as a suitable electrode candidate for rechargeable batteries. However, the Al primary and secondary batteries have not found a way into the market. In the Al primary battery, the voltage is lower than the theoretical value. This behavior is the result of a protective layer on Al that delays the voltage recovery phenomenon. In the Al secondary battery, operation at high temperatures is needed because of the restrictions of some high-temperature molten salts in electrolytes [116].

To meet the techno-economic requirements, positive electrodes should have specific properties. The energy density of oxide materials is close to the upper boundary. The positive electrode has the open-circuit voltage (OCV) of around 2.5 V and the positive electrode is required to possess a density above 4 g/cm^3 for meeting the requirement of, for example, the United States Advanced Battery Consortium goals [117].

3.2 Aluminum-ion batteries with different cathodes

According to Rani et al. [26], to obtain high energy density in Al-ion batteries, the cathode is required to release and accommodate the Al^{3+} ions during charge/discharge. Cathode materials such as V_2O_5 nano-wire and spinel λ-Mn_2O_4 showed promising results in rechargeable aluminum-ion batteries with an aluminum ion conducting ionic liquid electrolyte. There are extensive studies about graphite fluorides as cathode materials in lithium batteries [29, 33, 118-120] and to a certain extent in Al and Mg batteries [81]. For the first time, an Al-ion battery consisting of $AlCl_3$ and imidazolium-based ionic liquid electrolyte, fluorinated natural graphite cathode, and an aluminum anode is reported. Non-covalent C-F bonds are formed in fluorinated natural graphite prepared by the electrochemical method. The discharge capacity of 225 mAh g^{-1} as well as very stable electrochemical behavior was observed during the cycle life studies of these batteries [121].

In a study by Reed et al. [27], the electrochemistry of CuHCF as a cathode material for Al ions during cycling with aqueous Mg^{2+} is described in detail. The electrolyte was composed of aluminum triflate that was dissolved in diethylene glycol dimethyl ether (diglyme). They presented reversible Al intercalation and deintercalation from an organic electrolyte into CuHCF. The study indicated the intercalating behavior of the Al-solute complex [122]. The results showed that the initial discharge capacities of the system were as high as 60 mAh/g. Furthermore, reversible capacities were found to be in the range of 5 and 14 mAh/g, and capacity typically faded after 10 to 15 cycles. The redox activity of Cu^{+}/Cu^{2+} and Fe^{2+}/Fe^{3+} was observed in cyclic voltammograms. It was proposed that the third redox peak might be the result of the Fe^{3+}/Fe^{4+} redox couple. According to Gaussian calculations and capacity analysis, an Al/diglyme complex intercalated into defect sites in the CuHCF more than a free aluminum ion resulting in low reversible capacity.

Anatase TiO_2 nanotube arrays were incorporated in an aqueous solution of $AlCl_3$ and the electrochemical aluminum storage was investigated by Liu et al. [28]. The metallic Ti foil substrate was anodized and calcinated to prepare anatase TiO_2 nanotube arrays. It was shown that Al^{3+} ions are able to be reversibly inserted into and extracted from anatase nanotube arrays of TiO_2 in the presence of aqueous solution owing to the Al ion small radius steric influence. The diffusion of the solid phase into the anatase TiO_2 nanotube arrays controls the aluminum ion insertion. This research is a guide for the fabrication of new intercalation materials for using in aqueous rechargeable batteries based on small radius, multi-valent ions [123].

Hu et al. [29] reported a new cathode material for Al-ion batteries based on a self-standing and binder-free cobalt sulfide encapsulated in carbon nanotubes. They reported that the novel electrode materials showed very high cycling stability, improved rate performance of 154 mAh g^{-1} at 1 A g^{-1}, and a high discharge capacity of about 315 mAh g^{-1} at 100 mA g^{-1}. Its discharge capacity was stabilized at 87 mAh g^{-1} at 1 A g^{-1} after 6000 cycles. The material disintegrations and side reactions were suppressed by the electrode freestanding property. Based on this investigation, the design of high-performance cathode materials for flexible as well as scalable Al-ion batteries s is possible [124].

Wang et al. [30] developed an aqueous rechargeable Zn/Al ion battery in which the positive electrode was ultrathin graphite nanosheets, the negative electrode was zinc, and the electrolyte was $Al_2(SO_4)_3$/$Zn(CHCOO)_2$. The preparation method for the positive electrode was the electrochemical expansion in aqueous solution. The raw materials for the preparation of the Zn negative electrode and the aqueous electrolyte are abundant and the cost is low [125]. The average operating voltage of this rechargeable battery (1.0 V) was reported to be higher compared to most rechargeable AIBs with ionic liquid electrolytes. Furthermore, the battery maintained a high capacity and was able to be rapidly charged in 2 min. It was also capable of retention of capacity (94%) after 200 cycles showing its good cycling behavior [126].

As a result of natural abundance and high electrochemical activity, Wei et al. [32] used MoO_2 as a host material for Li storage. The ionic liquid electrolyte was 1-ethyl-3- methylimidazolium chloride/$AlCl_3$ and the cathode was prepared by fabrication of a dense MoO_2 layer on nickel foam. It was observed that the discharge potential was 1.9 V that is indicated to be higher than most metal oxide cathodes of AIBs studied so far. Moreover, at 100 mA g^{-1}, it exhibited a specific discharge capacity of 90 mAh g-1. However, after long cycling, the dissolution of molybdenum oxide and its transfer to the separator lead to a rapid capacity decay [127].

3.3 Aluminum-ion batteries with composite cathodes

A new AIB based on intercalation and deintercalation of Al^{3+} was developed by Wang et al. [6]. In this battery, the anode was Al foil, the cathode material was Ni_3S_2/graphene micro flakes composite, and the ionic liquid electrolyte was 1-ethyl-3- methylimidazolium chloride/ $AlCl_3$. A high discharge voltage plateau was observed in the battery (≈1.0 V vs. $Al/AlCl^{4-}$) providing a remarkable step forward in developing AIBs.

Zhang et al. [3] used a composite of VS_4 and reduced graphene oxide (rGO) for the AIB cathode with ionic liquid electrolytes. At 100 mA g^{-1}, the initial charge specific capacity and discharge specific capacity were reported to approach 491.57 and 406.94 mAh g_{-1}, respectively. High-retained capacity and coulombic efficiency above 90% after 100 cycles are the indicators of the suitability of the cathode material for new rechargeable Al-ion batteries.

The microsphere composite of Li_3VO_4@C was developed by Jiang et al. [128] as a new cathode material used in AIBs. According to the results, the battery initial discharge capacity was 137 mAh g^{-1}, and the retained capacity upon 100 cycles was measured to be 48 mAh g^{-1} with coulombic efficiency of almost 100%. It was observed that metallic aluminum was dissolved and deposited in the anode and Al^{3+} cations inserted and de-inserted in the cathode. These fabricated rechargeable AIBs had low cost and high safety offering them suitable cathode materials in acidic ionic liquid electrolyte systems.

The rechargeable AIB prepared by Wang et al. [129] was composed of an ionic liquid electrolyte of 1- ethyl-3-methylimidazolium chloride/ $AlCl_3$ and a cathode of three-dimensional hierarchical CuS microsphere composed of nanoflakes. The battery demonstrated a coulombic efficiency of approximately 100% after 100 cycles, an average discharge voltage of nearly 1.0 V vs. $Al/AlCl^4$, and a reversible specific capacity of 90 mAh g^{-1} at 20 mA g^{-1}. The well-defined cathode nanostructure facilitates the ion/electron transfer, particularly for large-sized chloroaluminate ions resulting in remarkable electrochemical performance.

The use of natural graphite for the cathode for AIBs was reported by Wei et al. [130]. Nevertheless, the natural graphite lifetime is short due to some problems such as severe volume swelling. Therefore, the authors deposited an amorphous carbon on a graphite paper. According to the charge/discharge outcomes, the cycle life of the composite was higher than that of the graphite paper. It was also indicated that the enhancement of the cycling stability was mostly attributed to the graphite paper and amorphous carbon interface.

In a study by Chiku et al. [131], a composite of carbon/V_2O_5 was prepared for the positive electrode of AIB. The electrolyte solution was a mix of toluene, aluminum chloride, and dipropylsulfone with a mass ratio of 1:10:5. The amorphous V_2O_5 exhibited a reversible oxidation/ reduction reaction in the electrolyte. The rechargeable AIB with the positive electrode of V_2O_5/carbon exhibited a discharge capacity of more than 200 mA g^{-1} with the C/40 discharge rate.

The aluminum secondary battery developed by Uemura et al. [132] was composed of ionic liquid electrolytes of 1-ethyl-3-methylimidazolium chloride/$AlCl_3$, aluminum metal anode, and a cathode of graphene nanoplatelet composite, which was fabricated by a slurry-coating route. The battery showed capacity retention of around 66 % at 6000 mA g^{-1}, and a reversible capacity of 70 mAh g^{-1} at 2000 mA g^{-1}. At 2000 mA g^{-1}, a coulombic efficiency of 99% was obtained up to 3000 cycles.

4. Conclusions and future insights

This paper first summarized the types of electrolytic batteries in terms of the electrolyte type including solid, liquid, and ionic electrolytes. Then, due to the advantages of Al-ion batteries including excellent reversibility, high security, and low cost, more details are presented about these batteries. Some AIB cathodes including composite cathodes were introduced. A new trend for AIB development seems to be composite materials such as graphite, CuS, V_2O_5, Li_3VO_4@C, VS_4/rGO, and Ni_3S_2/graphene. However, such materials still have some drawbacks such as structural decomposition, low battery capacity, low discharge voltage, and volume expansion resulting from the embedment of large size intercalation ions [133]. The AIB development is still in primary stages; however, there are clear directions for forthcoming research. Future investigations might concentrate on seeking cheaper electrolytes and novel cathode materials to promote energy density and working voltage. Laptops and smartphones need high energy density, thus the application of AIBs in these devices is not feasible at present. On the other hand, AIBs can offer high power and fast charge transfer to balance the electricity supply, which is required for the electricity grid. AIBs can play a pivotal role in production and life in the future if their electrochemical performance is remarkably improved [112].

REFERENCES

[1] S. Saadi, B. Nazari, Recent developments and applications of nanocomposites in solar cells: a review, Journal of Composites and Compounds 1(1) (2019) 48-58.

[2] J. Shin, Ionic liquids to the rescue Overcoming the ionic conductivity limitations of polymer electrolytes, Electrochemistry Communications 5(12) (2003) 1016-1020.

[3] X. Zhang, S. Wang, J. Tu, G. Zhang, S. Li, D. Tian, S. Jiao, Flower-like Vanadium Suflide/Reduced Graphene Oxide Composite: An Energy Storage Material for Aluminum-Ion Batteries, ChemSusChem 11(4) (2018) 709-715.

[4] T. Leisegang, F. Meutzner, M. Zschornak, W. Munchgesang, R. Schmid, T. Nestler, R.A. Eremin, A.A. Kabanov, V.A. Blatov, D.C. Meyer, The Aluminum-Ion Battery: A Sustainable and Seminal Concept?, Front Chem 7 (2019) 268.

[5] A. Kim, Li Intercalation into Carbonaceous Anode Materials for $LiAlCl_4·3SO_2$ Electrolyte Based Lithium Ion Battery, Hanyang, 2019.

[6] S. Wang, Z. Yu, J. Tu, J. Wang, D. Tian, Y. Liu, S. Jiao, A novel aluminum-ion battery: $Al/AlCl_3$-[EMIm] Cl/Ni_3S_2@graphene, Advanced Energy Materials 6(13) (2016) 1600137.

[7] J. Li, C. Ma, M. Chi, C. Liang, N.J. Dudney, Solid Electrolyte: the Key for High-Voltage Lithium Batteries, Advanced Energy Materials 5(4) (2015).

[8] Y. Ru, S. Zheng, H. Xue, H. Pang, Potassium cobalt hexacyanoferrate nanocubic assemblies for high-performance aqueous aluminum ion batteries, Chemical Engineering Journal 382 (2020) 122853.

[9] K. Zhang, H.W. Jang, Q. Van Le, Production methods of ceramic-reinforced Al-Li matrix composites: A review, Journal of Composites and Compounds 2(3) (2020) 76-84.

[10] I. Tajzad, E. Ghasali, Production methods of CNT-reinforced Al matrix composites: a review, Journal of Composites and Compounds 2(1) (2020) 1-9.

[11] J. Jiang, H. Li, J. Huang, K. Li, J. Zeng, Y. Yang, J. Li, Y. Wang, J. Wang, J. Zhao, Investigation of the Reversible Intercalation/Deintercalation of Al into the Novel Li_3VO_4@C Microsphere Composite Cathode Material for Aluminum-Ion Batteries, ACS Appl Mater Interfaces 9(34) (2017) 28486-28494.

[12] S. Wang, S. Jiao, J. Wang, H.S. Chen, D. Tian, H. Lei, D.N. Fang, High-Performance Aluminum-Ion Battery with CuS@C Microsphere Composite Cathode, ACS Nano 11(1) (2017) 469-477.

[13] N.C. Rosero-Navarro, A. Miura, K. Tadanaga, Preparation of lithium ion conductive Li_6PS_5Cl solid electrolyte from solution for the fabrication of composite cathode of all-solid-state lithium battery, Journal of Sol-Gel Science and Technology 89(1) (2019) 303-309.

[14] L. Larush, V. Borgel, E. Markevich, O. Haik, E. Zinigrad, D. Aurbach, G. Semrau, M. Schmidt, On the thermal behavior of model Li–$LixCoO_2$ systems con-

taining ionic liquids in standard electrolyte solutions, Journal of Power Sources 189(1) (2009) 217-223.

[15] A. Lewandowski, A. Świderska-Mocek, Ionic liquids as electrolytes for Li-ion batteries—An overview of electrochemical studies, Journal of Power Sources 194(2) (2009) 601-609.

[16] Y. Zhang, Y. Zhao, K. Eun Sun, P. Chen, Development in lithium/sulfur secondary batteries, The Open Materials Science Journal 5(1) (2011).

[17] S.S. Zhang, Liquid electrolyte lithium/sulfur battery: fundamental chemistry, problems, and solutions, Journal of Power Sources 231 (2013) 153-162.

[18] R. Rauh, K. Abraham, G. Pearson, J. Surprenant, S. Brummer, A lithium/dissolved sulfur battery with an organic electrolyte, Journal of the Electrochemical Society 126(4) (1979) 523.

[19] E. Peled, Y. Sternberg, A. Gorenshtein, Y. Lavi, Lithium-sulfur battery: evaluation of dioxolane-based electrolytes, Journal of the Electrochemical Society 136(6) (1989) 1621.

[20] S.S. Zhang, J.A. Read, A new direction for the performance improvement of rechargeable lithium/sulfur batteries, Journal of Power Sources 200 (2012) 77-82.

[21] Z. Ye, Z. Cao, M.O. Lam Chee, P. Dong, P.M. Ajayan, J. Shen, M. Ye, Advances in Zn-ion batteries via regulating liquid electrolyte, Energy Storage Materials 32 (2020) 290-305.

[22] S. Sarwar, M.-s. Lee, S. Park, T.T. Dao, A. Ullah, S. Hong, C.-H. Han, Transformation of a liquid electrolyte to a gel inside dye sensitized solar cells for better stability and performance, Thin Solid Films 704 (2020) 138024.

[23] S.S. Zhang, New insight into liquid electrolyte of rechargeable lithium/sulfur battery, Electrochimica Acta 97 (2013) 226-230.

[24] H. Yamin, A. Gorenshtein, J. Penciner, Y. Sternberg, E. Peled, Lithium sulfur battery: oxidation/reduction mechanisms of polysulfides in THF solutions, Journal of the Electrochemical Society 135(5) (1988) 1045.

[25] D. Marmorstein, T. Yu, K. Striebel, F. McLarnon, J. Hou, E. Cairns, Electrochemical performance of lithium/sulfur cells with three different polymer electrolytes, Journal of Power Sources 89(2) (2000) 219-226.

[26] H.-S. Ryu, H.-J. Ahn, K.-W. Kim, J.-H. Ahn, J.-Y. Lee, Discharge process of Li/PVdF/S cells at room temperature, Journal of Power Sources 153(2) (2006) 360-364.

[27] J. Shin, S. Jung, K. Kim, H. Ahn, J. Ahn, Preparation and characterization of plasticized polymer electrolytes based on the PVdF-HFP copolymer for lithium/sulfur battery, Journal of Materials Science: Materials in Electronics 13(12) (2002) 727-733.

[28] B.H. Jeon, J.H. Yeon, I.J. Chung, Preparation and electrical properties of lithium–sulfur-composite polymer batteries, Journal of materials processing technology 143 (2003) 93-97.

[29] B.H. Jeon, J.H. Yeon, K.M. Kim, I.J. Chung, Preparation and electrochemical properties of lithium–sulfur polymer batteries, Journal of power sources 109(1) (2002) 89-97.

[30] J.-W. Choi, J.-K. Kim, G. Cheruvally, J.-H. Ahn, H.-J. Ahn, K.-W. Kim, Rechargeable lithium/sulfur battery with suitable mixed liquid electrolytes, Electrochimica Acta 52(5) (2007) 2075-2082.

[31] E. Peled, A. Gorenshtein, M. Segal, Y. Sternberg, Rechargeable lithium sulfur battery, Journal of Power Sources 26(3-4) (1989) 269-271.

[32] H. Ryu, H. Ahn, K. Kim, J. Ahn, J.-Y. Lee, E. Cairns, Self-discharge of lithium–sulfur cells using stainless-steel current-collectors, Journal of Power Sources 140(2) (2005) 365-369.

[33] D.-R. Chang, S.-H. Lee, S.-W. Kim, H.-T. Kim, Binary electrolyte based on tetra (ethylene glycol) dimethyl ether and 1, 3-dioxolane for lithium–sulfur battery, Journal of Power Sources 112(2) (2002) 452-460.

[34] S.-E. Cheon, K.-S. Ko, J.-H. Cho, S.-W. Kim, E.-Y. Chin, H.-T. Kim, Rechargeable lithium sulfur battery: I. Structural change of sulfur cathode during discharge and charge, Journal of the Electrochemical Society 150(6) (2003) A796.

[35] H.-S. Ryu, H.-J. Ahn, K.-W. Kim, J.-H. Ahn, K.-K. Cho, T.-H. Nam, J.-U. Kim, G.-B. Cho, Discharge behavior of lithium/sulfur cell with TEGDME based electrolyte at low temperature, Journal of Power Sources 163(1) (2006) 201-206.

[36] J. Wang, Y. Wang, X. He, J. Ren, C. Jiang, C. Wan, Electrochemical characteristics of sulfur composite cathode materials in rechargeable lithium batteries, Journal of power sources 138(1-2) (2004) 271-273.

[37] J. Wang, L. Liu, Z. Ling, J. Yang, C. Wan, C. Jiang, Polymer lithium cells with sulfur composites as cathode materials, Electrochimica Acta 48(13) (2003) 1861-1867.

[38] H. Yang, F. Wu, Y. Bai, C. Wu, Toward better electrode/electrolyte interfaces in the ionic-liquid-based rechargeable aluminum batteries, Journal of Energy Chemistry 45 (2020) 98-102.

[39] X. Wang, Z. Shang, A. Yang, Q. Zhang, F. Cheng, D. Jia, J. Chen, Combining quinone cathode and ionic liquid electrolyte for organic sodium-ion batteries, Chem 5(2) (2019) 364-375.

[40] X. Ke, Y. Wang, L. Dai, C. Yuan, Cell failures of all-solid-state lithium metal batteries with inorganic solid electrolytes: Lithium dendrites, Energy Storage Materials (2020).

[41] X. Wang, J. Sun, C. Feng, X. Wang, M. Xu, J. Sun, N. Zhang, J. Ma, Q. Wang, C. Zong, G. Cui, Lithium bis(oxalate)borate crosslinked polymer electrolytes for high-performance lithium batteries, Journal of Energy Chemistry 55 (2021) 228-235.

[42] X. Zhang, W. Zhou, M. Zhang, Z. Yang, W. Huang, Superior performance for lithium-ion battery with organic cathode and ionic liquid electrolyte, Journal of Energy Chemistry 52 (2021) 28-32.

[43] Z. Zhang, J. Zhang, H. Jia, L. Peng, T. An, J. Xie, Enhancing ionic conductivity of solid electrolyte by lithium substitution in halogenated Li-Argyrodite, Journal of Power Sources 450 (2020) 227601.

[44] M.A.K.L. Dissanayake, T. Liyanage, T. Jaseetharan, G.K.R. Senadeera, B.S. Dassanayake, Effect of PbS quantum dot-doped polysulfide nanofiber gel polymer electrolyte on efficiency enhancement in CdS quantum dot-sensitized TiO_2 solar cells, Electrochimica Acta 347 (2020) 136311.

[45] A. Gupta, A. Bhargav, J.-P. Jones, R.V. Bugga, A. Manthiram, Influence of Lithium Polysulfide Clustering on the Kinetics of Electrochemical Conversion in Lithium–Sulfur Batteries, Chemistry of Materials 32(5) (2020) 2070-2077.

[46] Z. Liu, V.S. Manikandan, A. Chen, Recent advances in nanomaterial-based electrochemical sensing of nitric oxide and nitrite for biomedical and food research, Current Opinion in Electrochemistry 16 (2019) 127-133.

[47] S.-e. Sheng, L. Sheng, L. Wang, N. Piao, X. He, Thickness variation of lithium metal anode with cycling, Journal of Power Sources 476 (2020) 228749.

[48] L. Kong, L. Yin, F. Xu, J. Bian, H. Yuan, Z. Lu, Y. Zhao, Electrolyte solvation chemistry for lithium–sulfur batteries with electrolyte-lean conditions, Journal of Energy Chemistry 55 (2021) 80-91.

[49] R. Weber, M. Genovese, A. Louli, S. Hames, C. Martin, I.G. Hill, J. Dahn, Long cycle life and dendrite-free lithium morphology in anode-free lithium pouch cells enabled by a dual-salt liquid electrolyte, Nature Energy 4(8) (2019) 683-689.

[50] H. Xia, C. Li, H. Chen, Green preparation of CuI particles in dielectric barrier discharge for colorimetric determination of trace mercury in comparison with atomic fluorescence spectrometric determination, Microchemical Journal 146 (2019) 1169-1172.

[51] H. Zhuo, X. Wang, A. Tang, Z. Liu, S. Gamboa, P. Sebastian, The preparation of $NaV_{1-x}Cr_xPO_4F$ cathode materials for sodium-ion battery, Journal of power sources 160(1) (2006) 698-703.

[52] R. Alcántara, J.M. Jiménez-Mateos, P. Lavela, J.L. Tirado, Carbon black: a promising electrode material for sodium-ion batteries, Electrochemistry Communications 3(11) (2001) 639-642.

[53] S. Komaba, C. Takei, T. Nakayama, A. Ogata, N. Yabuuchi, Electrochemical intercalation activity of layered $NaCrO_2$ vs. $LiCrO_2$, Electrochemistry Communications 12(3) (2010) 355-358.

[54] P. Moreau, D. Guyomard, J. Gaubicher, F. Boucher, Structure and stability of sodium intercalated phases in olivine $FePO_4$, Chemistry of Materials 22(14) (2010) 4126-4128.

[55] K.O. Oyedotun, T.M. Masikhwa, S. Lindberg, A. Matic, P. Johansson, N. Manyala, Comparison of ionic liquid electrolyte to aqueous electrolytes on carbon nanofibres supercapacitor electrode derived from oxygen-functionalized graphene, Chemical Engineering Journal 375 (2019) 121906.

[56] H. Ryu, T. Kim, K. Kim, J.-H. Ahn, T. Nam, G. Wang, H.-J. Ahn, Discharge reaction mechanism of room-temperature sodium–sulfur battery with tetra ethylene glycol dimethyl ether liquid electrolyte, Journal of Power Sources 196(11) (2011) 5186-5190.

[57] R. Pathak, K. Chen, A. Gurung, K.M. Reza, B. Bahrami, J. Pokharel, A. Baniya, W. He, F. Wu, Y. Zhou, Fluorinated hybrid solid-electrolyte-interphase for dendrite-free lithium deposition, Nature communications 11(1) (2020) 1-10.

[58] Y. Liu, J. Liu, Q. Sun, D. Wang, K.R. Adair, J. Liang, C. Zhang, L. Zhang, S. Lu, H. Huang, Insight into the microstructure and ionic conductivity of cold sintered NASICON solid electrolyte for solid-state batteries, ACS applied materials & interfaces 11(31) (2019) 27890-27896.

[59] Z. Chang, Y. Qiao, H. Deng, H. Yang, P. He, H. Zhou, A Liquid Electrolyte with De-Solvated Lithium Ions for Lithium-Metal Battery, Joule 4(8) (2020) 1776-1789.

[60] Y. Deng, X. Zhu, N. Chen, C. Feng, H. Wang, P. Kuang, W. Hu, Review on electrochemical system for landfill leachate treatment: Performance, mechanism, application, shortcoming, and improvement scheme, Science of The Total Environment 745 (2020) 140768.

[61] A. Sakuda, A. Hayashi, M. Tatsumisago, Sulfide solid electrolyte with favorable mechanical property for all-solid-state lithium battery, Sci Rep 3 (2013) 2261.

[62] A.L. Santhosha, L. Medenbach, T. Palaniselvam, P. Adelhelm, Sodium-Storage Behavior of Exfoliated MoS_2 as an Electrode Material for Solid-State Batteries with Na_3PS_4 as the Solid Electrolyte, The Journal of Physical Chemistry C 124(19) (2020) 10298-10305.

[63] T. Le Varlet, O. Schmidt, A. Gambhir, S. Few, I. Staffell, Comparative life cycle assessment of lithium-ion battery chemistries for residential storage, Journal of Energy Storage 28 (2020) 101230.

[64] R. Yazami, Y.F. Reynier, Mechanism of self-discharge in graphite–lithium anode, Electrochimica Acta 47(8) (2002) 1217-1223.

[65] P. Novák, J.-C. Panitz, F. Joho, M. Lanz, R. Imhof, M. Coluccia, Advanced in situ methods for the characterization of practical electrodes in lithium-ion batteries, Journal of power sources 90(1) (2000) 52-58.

[66] N. Ogihara, Y. Igarashi, A. Kamakura, K. Naoi, Y. Kusachi, K. Utsugi, Disordered carbon negative electrode for electrochemical capacitors and high-rate batteries, Electrochimica acta 52(4) (2006) 1713-1720.

[67] F. Ding, Y. Liu, X. Hu, 1,3-dioxolane pretreatment to improve the interfacial characteristics of a lithium anode, Rare Metals 25(4) (2006) 297-302.

[68] P. Verma, P. Maire, P. Novák, A review of the features and analyses of the solid electrolyte interphase in Li-ion batteries, Electrochimica Acta 55(22) (2010) 6332-6341.

[69] K.-H. Lee, D.B. Ahn, J.-H. Kim, J.-W. Lee, S.-Y. Lee, Printed Built-In Power Sources, Matter 2(2) (2020) 345-359.

[70] D.J. Suh, C. Kwak, J.-H. Kim, S.M. Kwon, T.-J. Park, Removal of carbon monoxide from hydrogen-rich fuels by selective low-temperature oxidation over base metal added platinum catalysts, Journal of Power Sources 142(1) (2005) 70-74.

[71] A. Sakuda, A. Hayashi, T. Ohtomo, S. Hama, M. Tatsumisago, $LiCoO_2$ electrode particles coated with $Li_2S–P_2S_5$ solid electrolyte for all-solid-state batteries, Electrochemical and Solid State Letters 13(6) (2010) A73.

[72] X. Wang, Y. Qian, L. Wang, H. Yang, H. Li, Y. Zhao, T. Liu, Sulfurized polyacrylonitrile cathodes with high compatibility in both ether and carbonate electrolytes for ultrastable lithium–sulfur batteries, Advanced Functional Materials 29(39) (2019) 1902929.

[73] X. Judez, M. Martinez-Ibañez, A. Santiago, M. Armand, H. Zhang, C. Li, Quasi-solid-state electrolytes for lithium sulfur batteries: Advances and perspectives, Journal of Power Sources 438 (2019) 226985.

[74] S. Wang, K.V. Kravchyk, A.N. Filippin, R. Widmer, A.N. Tiwari, S. Buecheler, M.I. Bodnarchuk, M.V. Kovalenko, Overcoming the High-Voltage Limitations of Li-Ion Batteries Using a Titanium Nitride Current Collector, ACS Applied Energy Materials 2(2) (2019) 974-978.

[75] D. Hayashi, K. Suzuki, S. Hori, Y. Yamada, M. Hirayama, R. Kanno, Synthesis of $Li_{10}GeP_2S_{12}$-type lithium superionic conductors under Ar gas flow, Journal of Power Sources 473 (2020) 228524.

[76] L.X. Yuan, J.K. Feng, X.P. Ai, Y.L. Cao, S.L. Chen, H.X. Yang, Improved dischargeability and reversibility of sulfur cathode in a novel ionic liquid electrolyte, Electrochemistry Communications 8(4) (2006) 610-614.

[77] M. Batteries, CA Vincent and B, Scrosati Wiley, New York (1997) 198-242.

[78] M. Diaw, A. Chagnes, B. Carré, P. Willmann, D. Lemordant, Mixed ionic liquid as electrolyte for lithium batteries, Journal of Power Sources 146(1-2) (2005) 682-684.

[79] C. Niu, J. Liu, G. Chen, C. Liu, T. Qian, J. Zhang, B. Cao, W. Shang, Y. Chen, J. Han, Anion-regulated solid polymer electrolyte enhances the stable deposition of lithium ion for lithium metal batteries, Journal of Power Sources 417 (2019) 70-75.

[80] J.-M. Tarascon, M. Armand, Issues and challenges facing rechargeable lithium batteries, Materials for sustainable energy: a collection of peer-reviewed research and review articles from Nature Publishing Group, World Scientific2011, pp. 171-179.

[81] ElectroChem integrates fuel cell technology in India, South Asia, Fuel Cells Bulletin 2007(8) (2007) 7.

[82] G. Angajala, R. Subashini, V. Aruna, Microwave assisted amberlite-IRA-402 (OH) ion exchange resin catalyzed synthesis of new benzoxazole scaffolds derived from antiinflammatory drugs aceclofenac and mefenamic acid as potential therapeutic agents for inflammation, Journal of Molecular Structure 1200 (2020) 127092.

[83] L. Auzel, Y. Ali, C. Monini, J.M. Létang, E. Testa, M. Beuve, L. Maigne, 35 Simulation of micro-nanodosimetry spectra and free radicals with Geant4-DNA, LQD, PHYCHEML, CHEM for ion beams, Physica Medica 68 (2019) 21-22.

[84] P. Vikas, I. Sudhakar, Dilkush, G. MohanaRao, B. Srinivas, Aging behaviour of hot deformed AA7075 aluminium alloy, Materials Today: Proceedings (2020).

[85] M. Alizadeh, M. Paydar, F.S. Jazi, Structural evaluation and mechanical properties of nanostructured Al/B_4C composite fabricated by ARB process, Composites Part B: Engineering 44(1) (2013) 339-343.

[86] E.H. Jazi, R. Esalmi-Farsani, G. Borhani, F.S. Jazi, Synthesis and Characterization of In Situ $Al-Al_{13}Fe_4-Al_2O_3-TiB_2$ Nanocomposite Powder by Mechanical Alloying and Subsequent Heat Treatment, Synthesis and Reactivity in Inorganic, Metal-Organic, and Nano-Metal Chemistry 44(2) (2014) 177-184.

[87] K. Parveen, U. Rafique, M. Javed Akhtar, M. Ashokkumar, Sonochemical synthesis of aluminium and aluminium hybrids for remediation of toxic metals, Ultrasonics Sonochemistry 70 (2021) 105299.

[88] H. Dohle, J. Mergel, D. Stolten, Heat and power management of a direct-methanol-fuel-cell (DMFC) system, Journal of Power Sources 111(2) (2002) 268-282.

[89] M. Tamski, J.P. Ansermet, C. Roussel, Stabilization of p-GaAs electrode surfaces in organic solvent by bi-phenyl rings for spin dependent electron transfer studies, Journal of Photochemistry and Photobiology A: Chemistry (2020) 112853.

[90] A. Fernández-Guillamón, E. Gómez-Lázaro, E. Muljadi, Á. Molina-García, Power systems with high renewable energy sources: A review of inertia and frequency control strategies over time, Renewable and Sustainable Energy Reviews 115 (2019) 109369.

[91] N.R. Avery, K.J. Black, Kinetic analysis of capacity fade in lithium/coke half-cells, Journal of Power Sources 68(2) (1997) 191-194.

[92] K.G.Y. Beaudelaire, B. Zhuang, J.T. Aladejana, D. Li, X. Hou, Y. Xie, Influence of Mesoporous Inorganic Al–B–P Amphiprotic Surfactant Material Resistances of Wood against Brown and White-Rot Fungi (Part 1), Coatings 10(2) (2020) 108.

[93] S. Abedini, N. Parvin, P. Ashtari, F. Jazi, Microstructure, strength and CO_2 separation characteristics of α-alumina supported γ-alumina thin film membrane, Advances in Applied Ceramics 112(1) (2013) 17-22.

[94] H. Sun, W. Wang, Z. Yu, Y. Yuan, S. Wang, S. Jiao, A new aluminium-ion battery with high voltage, high safety and low cost, Chemical Communications 51(59) (2015) 11892-11895.

[95] N.S. Hudak, Chloroaluminate-doped conducting polymers as positive electrodes in rechargeable aluminum batteries, The Journal of Physical Chemistry C 118(10) (2014) 5203-5215.

[96] J.V. Rani, V. Kanakaiah, T. Dadmal, M.S. Rao, S. Bhavanarushi, Fluorinated natural graphite cathode for rechargeable ionic liquid based aluminum–ion battery, Journal of The Electrochemical Society 160(10) (2013) A1781.

[97] S. Liu, J. Hu, N. Yan, G. Pan, G. Li, X. Gao, Aluminum storage behavior of anatase TiO_2 nanotube arrays in aqueous solution for aluminum ion batteries, Energy & Environmental Science 5(12) (2012) 9743-9746.

[98] L. Bazli, M. Siavashi, A. Shiravi, A Review of Carbon nanotube/TiO_2 Composite prepared via Sol-Gel method, Journal of Composites and Compounds 1(1) (2019) 1-12.

[99] N. Jayaprakash, S. Das, L. Archer, The rechargeable aluminum-ion battery, Chemical Communications 47(47) (2011) 12610-12612.

[100] S. Liu, G. Pan, G. Li, X. Gao, Copper hexacyanoferrate nanoparticles as cathode material for aqueous Al-ion batteries, Journal of Materials Chemistry A 3(3) (2015) 959-962.

[101] L.D. Reed, E. Menke, The roles of V_2O_5 and stainless steel in rechargeable Al–ion batteries, Journal of the Electrochemical Society 160(6) (2013) A915.

[102] W. Wang, B. Jiang, W. Xiong, H. Sun, Z. Lin, L. Hu, J. Tu, J. Hou, H. Zhu, S. Jiao, A new cathode material for super-valent battery based on aluminium ion intercalation and deintercalation, Scientific reports 3(1) (2013) 1-6.

[103] S. Wang, Z. Yu, J. Tu, J. Wang, D. Tian, Y. Liu, S. Jiao, A Novel Aluminum-Ion Battery: $Al/AlCl_3$-[EMIm]Cl/Ni_3S_2@Graphene, Advanced Energy Materials 6(13) (2016).

[104] Y. Liu, Q. Sun, W. Li, K.R. Adair, J. Li, X. Sun, A comprehensive review on recent progress in aluminum–air batteries, Green Energy & Environment 2(3) (2017) 246-277.

[105] Q. Li, N.J. Bjerrum, Aluminum as anode for energy storage and conversion: a review, Journal of Power Sources 110(1) (2002) 1-10.

[106] R.N. Mutlu, I. Kucukkara, A.M. Gizir, Hydrogen generation by electrolysis under subcritical water condition and the effect of aluminium anode, International Journal of Hydrogen Energy 45(23) (2020) 12641-12652.

[107] B. Craig, T. Schoetz, A. Cruden, C. Ponce de Leon, Review of current progress in non-aqueous aluminium batteries, Renewable and Sustainable Energy Reviews 133 (2020) 110100.

[108] A. Holland, R. Mckerracher, A. Cruden, R. Wills, An aluminium battery operating with an aqueous electrolyte, Journal of Applied Electrochemistry 48(3) (2018) 243-250.

[109] J. Li, J. Qiao, K. Lian, Hydroxide ion conducting polymer electrolytes and their applications in solid supercapacitors: a review, Energy Storage Materials 24 (2020) 6-21.

[110] K.M. Barcelos, K.S.G.C. Oliveira, L.A.M. Ruotolo, Insights on the role of interparticle porosity and electrode thickness on capacitive deionization perfor-

mance for desalination, Desalination 492 (2020) 114594.

[111] K.L. Ng, T. Dong, J. Anawati, G. Azimi, High-Performance Aluminum Ion Battery Using Cost-Effective $AlCl_3$-Trimethylamine Hydrochloride Ionic Liquid Electrolyte, Advanced Sustainable Systems (2020) 2000074.

[112] L. Wei, J. Tao, Y. Yang, X. Fan, X. Ran, J. Li, Y. Lin, Z. Huang, Surface sulfidization of spinel $LiNi_{0.5}Mn_{1.5}O_4$ cathode material for enhanced electrochemical performance in lithium-ion batteries, Chemical Engineering Journal 384 (2020) 123268.

[113] J. Zhong, Z. Yang, Y. Yu, Y. Liu, J. Li, F. Kang, Surface substitution of polyanion to improve structure stability and electrochemical properties of lithium-rich layered cathode oxides, Applied Surface Science 512 (2020) 145741.

[114] Y.-C. Yin, Q. Wang, J.-T. Yang, F. Li, G. Zhang, C.-H. Jiang, H.-S. Mo, J.-S. Yao, K.-H. Wang, F. Zhou, Metal chloride perovskite thin film based interfacial layer for shielding lithium metal from liquid electrolyte, Nature communications 11(1) (2020) 1-9.

[115] J. Schnell, T. Günther, T. Knoche, C. Vieider, L. Köhler, A. Just, M. Keller, S. Passerini, G. Reinhart, All-solid-state lithium-ion and lithium metal batteries – paving the way to large-scale production, Journal of Power Sources 382 (2018) 160-175.

[116] J. Wei, W. Chen, D. Chen, K. Yang, An amorphous carbon-graphite composite cathode for long cycle life rechargeable aluminum ion batteries, Journal of Materials Science & Technology 34(6) (2018) 983-989.

[117] K. Zhao, X. Shi, Y. Zhao, H. Wei, Q. Sun, T. Huang, X. Zhang, Y. Wang, Preparation and immunological effectiveness of a swine influenza DNA vaccine encapsulated in chitosan nanoparticles, Vaccine 29(47) (2011) 8549-8556.

[118] J. Shin, K. Kim, H. Ahn, J. Ahn, Electrochemical properties and interfacial stability of (PEO) $10LiCF_3SO_3$–$TinO_{2n-1}$ composite polymer electrolytes for lithium/sulfur battery, Materials Science and Engineering: B 95(2) (2002) 148-156.

[119] D.C. Kim, H.J. Shim, W. Lee, J.H. Koo, D.H. Kim, Material-Based Approaches for the Fabrication of Stretchable Electronics, Advanced Materials 32(15) (2020) 1902743.

[120] Y.M. Lee, N.-S. Choi, J.H. Park, J.-K. Park, Electrochemical performance of lithium/sulfur batteries with protected Li anodes, Journal of Power Sources 119 (2003) 964-972.

[121] S. Fang, D. Bresser, S. Passerini, Transition Metal Oxide Anodes for Electrochemical Energy Storage in Lithium-and Sodium-Ion Batteries, Advanced Energy Materials 10(1) (2020) 1902485.

[122] A. Rafique, M.A. Ahmad, I. Shakir, A. Ali, G. Abbas, M.S. Javed, M.A. Khan, R. Raza, Multioxide phase-based nanocomposite electrolyte (M@ SDC where M= $Zn^{2+}/Ba^{2+}/La^{3+}/Zr^{2+}/Al^{3+}$) materials, Ceramics International 46(5) (2020) 6882-6888.

[123] W. Guan, L. Wang, H. Lei, J. Tu, S. Jiao, Sb_2Se_3 nanorods with N-doped reduced graphene oxide hybrids as high-capacity positive electrode materials for rechargeable aluminum batteries, Nanoscale 11(35) (2019) 16437-16444.

[124] Y. Zhang, B. Zhang, J. Li, J. Liu, X. Huo, F. Kang, SnSe nano-particles as advanced positive electrode materials for rechargeable aluminum-ion batteries, Chemical Engineering Journal 403 (2021) 126377.

[125] K. Subramanyan, Y.-S. Lee, V. Aravindan, Impact of carbonate-based electrolytes on the electrochemical activity of carbon-coated $Na_3V_2(PO_4)_2F_3$ cathode in full-cell assembly with hard carbon anode, Journal of Colloid and Interface Science 582 (2021) 51-59.

[126] X. Ke, Y. Wang, G. Ren, C. Yuan, Towards rational mechanical design of inorganic solid electrolytes for all-solid-state lithium ion batteries, Energy Storage Materials 26 (2020) 313-324.

[127] Q. Zhao, F.K. Butt, Z. Guo, L. Wang, Y. Zhu, X. Xu, X. Ma, C. Cao, High-voltage P2-type manganese oxide cathode induced by titanium gradient modification for sodium ion batteries, Chemical Engineering Journal 403 (2021) 126308.

[128] J. Jiang, H. Li, J. Huang, K. Li, J. Zeng, Y. Yang, J. Li, Y. Wang, J. Wang, J. Zhao, Investigation of the reversible intercalation/deintercalation of Al into the novel Li3VO4@ C microsphere composite cathode material for aluminum-ion batteries, ACS applied materials & interfaces 9(34) (2017) 28486-28494.

[129] S. Wang, S. Jiao, J. Wang, H.-S. Chen, D. Tian, H. Lei, D.-N. Fang, High-performance aluminum-ion battery with CuS@ C microsphere composite cathode, ACS nano 11(1) (2017) 469-477.

[130] Y.-Q. Shen, F.-L. Zeng, X.-Y. Zhou, A.-b. Wang, W.-k. Wang, N.-Y. Yuan, J.-N. Ding, A novel permselective organo-polysulfides/PVDF gel polymer electrolyte enables stable lithium anode for lithium–sulfur batteries, Journal of Energy Chemistry 48 (2020) 267-276.

[131] D.-R. Chang, S.-H. Lee, S.-W. Kim, H.-T. Kim, Binary electrolyte based on tetra(ethylene glycol) dimethyl ether and 1,3-dioxolane for lithium–sulfur battery, Journal of Power Sources 112(2) (2002) 452-460.

[132] J. Zhou, X. Zhou, Y. Sun, X. Shen, T. Qian, C. Yan, Insight into the reaction mechanism of sulfur chains adjustable polymer cathode for high-loading lithium-organosulfur batteries, Journal of Energy Chemistry (2020).

[133] D.K. Rajak, D.D. Pagar, R. Kumar, C.I. Pruncu, Recent progress of reinforcement materials: A comprehensive overview of composite materials, Journal of Materials Research and Technology 8(6) (2019) 6354-6374.

Journal of Composites and Compounds 2 (2020) 147-154

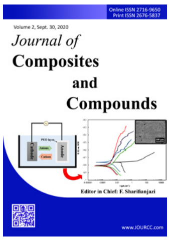

Available online at www.jourcc.com

Journal homepage: www.JOURCC.com

Journal of Composites and Compounds

A review on development and application of self-healing thermal barrier composite coatings

Aliasghar Abuchenari[a]***, Hadi Ghazanfari***[b]****, Mostafa Siavashi***[c]***, Maryam Sabetzadeh***[d]***, Sajad Talebi***[e]***,***

Zahra Karami Chemeh[f]***, Ata Jamavari***[g]

[a] *Materials Engineering, Shahid Bahonar University, Kerman, Iran*
[b] *Department of Mining, Metallurgical and Materials Engineering, Université Laval, Québec G1V 0A6, QC, Canada*
[c] *Faculty of Engineering, Christian-Albrechts-University Kiel, Germany*
[d] *Chemical Engineering Department, Polymer Group, Isfahan University of Technology, Isfahan, Iran*
[e] *Department of Materials and Metallurgy, Faculty of Engineering, University of Arak, Arak, Iran*
[f] *Department of textile Engineering, Amirkabir University of Technology, Tehran, Iran*
[g] *Department of Material Science and Engineering, University of Science and Technology, Tehran, Iran*

ABSTRACT

To improve the hot section metallic parts durability in advanced gas-turbine operating in power generation and aircraft, thermal barrier coating (TBCs) are extensively utilized to increase their lifetime. The reason for applying coatings on these components is the improvement of their physical properties, mechanical properties, and outer look. The self-repairing ability of materials is very promising due to expanding the service time of materials and it is also beneficial in terms of human safety and financial aspects. In this review article, structure, properties, limitations, and the modification approaches of TBCs were studied. In addition, self-healing agents for TBCs including SiC, $MoSi_2$, TiC were introduced, which release their oxide by reaction with air and O_2 that are able to heal the pores/cracks in the coatings. In this regard, their coating methods, mechanism, and applications in TBCs were reviewed.

ARTICLE INFORMATION

Article history:
Received 17 August 2020
Received in revised form 29 August 2020
Accepted 20 September 2020

Keywords:
Thermal barrier coating (TBC)
TBC lifetime
TBC modification
Self-healing composite

Table of contents

1. Introduction

Most industrial processes involve operating under harsh environments of high temperature, high pressure, increased temperature gradients, and foreign object damage (FOD), corroding and oxidizing atmosphere, and large stresses on individual components. Marine, aero, and industrial gas turbines are examples of such industrial processes [1].

Coatings on the surface of materials improve materials appearance, mechanical, and physical properties [2-4]. A thick barricade will be built on the surfaces of metals by the coating against atmospheric oxygen and water [5-7]. Thermal barrier coatings (TBCs) are extensively utilized for the durability enhancement of hot metallic components operating in advanced gas turbines or power generation and aircraft [8]. However, the initiation of cracks, their propagation, and coalescence result in the coating spallation, which exposes the hot-section metallic components

---

* *Corresponding author: Hadi Ghazanfari; E-mail: hadi.ghazanfari.1@ulaval.ca*

https://doi.org/10.29252/jcc.2.3.6

to high temperature and oxidation [9, 10].

In the past 15 years, a considerable section of research activities has been allocated to self-healing materials [11-13]. The aim of using self-healing materials is to restore the mechanical and physical integrity and properties rapidly after being damaged. The self-repairing ability of materials is a treasured characteristic due to expanding the material service period offering benefits in terms of financial aspects and human safety requirements [5, 14].

This review article focuses on the TBCs and their structures, restrictions, and modifications techniques [15]. Subsequently, self-healing materials and self-healing composite TBCs are introduced, and finally, their coating methods, mechanism, and applications in TBCs are discussed [16].

2. Structure of TBCs

In order to protect metallic parts of vanes, blades, and combustion chambers in jet engines and gas turbines from oxidation and corrosion at high temperatures, TBCs are often applied on their surfaces [17-19]. The TBCs primary function is to enable the hot operating parts to bear higher service temperatures beyond the underlying metals limit temperature. When the hot sections are protected by TBCs with a thickness in the range of 150 to 800 μm, the inlet temperature can be increased by 100 to 300 °C [20].

There are three layers in the TBC structure applied on the surface of a metallic substrate: 1) the bond-coat (BC) applied on the surface of the substrate; 2) thermally grown oxide (TGO), which is generated at the BC/TC interface; 3) the ceramic top-coat (TC) [21]. BC and TC commonly consist of MCrAlY (M can be Co, Ni, Fe, or their combinations) layer, and zirconia that is partially stabilized with Yittria (YSZ), respectively. The TGO oxide layer mostly composed of Al_2O_3, is generated at the BC/TC interface during high-temperature service in the air [22, 23]. YSZ has a porous structure and with the increase in service time, oxygen penetrates the coating or cracks and reacts with the bond coat materials. Due to this reaction, the TGO layer grows by the metallic BC selective oxidation and is mainly composed of alumina. One of the main reasons for cracking, delamination, and spallation of YSZ has been reported to be the TGO layer growth [24-27].

Zirconia-based coatings are favored in TBCs owing to their relatively high thermal expansion coefficient (TEC), good oxidation resistance, good thermal shock resistance low thermal conductivity, and good microstructure stability [28, 29].

3. TBC problems

Propagation of cracks in TBCs during the service period leads to the coating delamination and failure of TBC coatings on hot components [9, 30]. Spallation of the coatings occurs by the sequential steps of crack initiation, propagation, and coalescence leaving hot-section components unprotected against the high-temperature environment [1, 31]. TC is a high-temperature resistant oxide layer and BC is a connecting layer between TC and the substrate. The TGO layer formed by the diffusion of O_2 through TC and the BC layer oxidation has considerably different TEC with the top coat. Due to the thermal expansion coefficient mismatch, thermal cycling may cause stress in the coating resulting in the crack formation and the coating peeling leaving the substrate unprotected [32, 33]. Understanding the failure mechanisms in the TBC coatings during operation can help us improve the durability of these coatings. Several failure mechanisms have been reported in the literature [34]. Generally, three main mechanisms contribute to TBC failure:

1) Most TBC coatings fail at or near the BC/TGO interface resulting from elastic strain energy and stress concentration caused by the thickening of TGO and thermal expansion mismatch [35]. Upon cooling down from service temperature to room temperature, the mismatch of TEC between the substrate, BC, and TGO causes high compressive stresses in the ceramic layer [36]. Because of growth strain, high compressive stresses are applied to the TGO. Consequently, the strain energy is released by TGO distortion in the system, which leads to the creation of the tensile and compressive stress gradient. The key reason for nucleation and propagation of cracks in TGO and thereby, the ultimate spallation of the coating is tensile stress [34, 35, 37].

2) In air plasma-sprayed TBCs, spallation also occurs at the splat boundaries of the ceramic top coat. The spallation resistance of the coatings can be increased by altering the coatings architecture, sintering suppression within the top-coat, and using an innovative plasma-spray process [34, 38].

3) Besides thermal-driven damages, TBC damages might be due to mechanical causes such as mechanical fatigue caused by vibration and FOD [34, 39].

4. TBC modification

4.1. New TBCs

The refractory materials are preferably considered for developing new TBC materials. In this regard, the properties of four ceramic material groups are believed to be more promising for further investigations. These groups are mainly highly-defected zirconium oxide compounds, rare fluorite, and pyrochlore-type earth zirconates, hexa-aluminates, and perovskites. Fluorite and pyrochlore-type earth zirconates have been considered as the most promising choices for the development of new TBC coatings [26, 40].

Predicting the lifetime of TBCs is essential for the improvement of the safety of TBC components [41]. The turbine inlet temperature can be increased to 2000 K in the new generation of engines having high thrust ratios [42]. In these cases, YSZ-based traditional TBCs could not satisfy the requirements of thermal barriers [43]. In recent years, new TBC materials have been widely explored in order to build coatings that can bear higher temperatures than the traditional TBCs [25]. Some new TBCs include: 1) Lanthanum cerium oxide ($La_2Ce_2O_7$) that possess a lower thermal conductivity and a higher TEC than those of YSZ; Lanthanum cerium oxide ($La_2Ce_2O_7$) was proposed as a new material for TBC for its low thermal conductivity and large TEC, which is close to the BCs thermal expansion coefficient. Thermal cycling studies using a $La_2Ce_2O_7$ coating showed that the thermal stability of the $La_2Ce_2O_7$ coating is comparable to the stability of the more traditional YSZ coating. Thus, the lifetime of a single layer of $La_2Ce_2O_7$ is similar to the lifetime of a single layer of YSZ. However, for multi-layer coatings, the $La_2Ce_2O_7$ coatings showed a longer lifetime than the YSZ coatings [44-46].

2) Pyrochlore oxides ($A_2B_2O_7$) are structures comprised of 2 cations with a +3 oxidation state, such as La^{3+}, or Lu^{3+} (indicated by A), 2 cations with a +4 oxidation state, such as Zr^{4+}, Hf^{4+} or Ti^{4+} (indicated by B), and 7 oxygen anions. $Gd_2Zr_2O_7$ and $La_2Zr_2O_7$ are common examples of these pyrochlore oxides. These materials typically have a lower thermal conductivity, a higher melting point, and a relatively higher TEC compared to YSZ, which makes them suitable for TBC [24, 47-49].

3) Neodymium cerate ($Nd_2Ce_2O_7$) has a fluorite type crystal structure, which is stable at high temperatures up to 1600 °C and has a lower thermal conductivity than YSZ [29]. These thermal properties make this material very promising to be used in advanced TBCs [50-53], such as those used in turbine engines [54, 55].

4) Another material proposed as a new TBC is NiCoCrAlY, which is thermally stable at temperatures ranging from 1200 to 1400 °C [56].

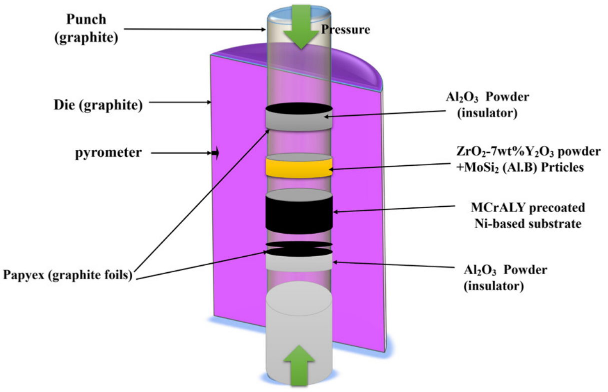

Fig. 1. Self-healing mechanism in TBCs with $MoSi_2$ particles.

This material is used on Ni-based superalloys to improve its resistance to oxidation. At high temperatures, NiCoCrAlY forms an oxide layer between the BC and the ceramic top coat. The underlying metal is protected from further oxidation by this oxide layer. This oxide layer is also the first place where this TBC fails and thereby, the spallation of TC is promoted [57-59].

4.2. Changing structure

Along with the new gas turbine development, there have been many investigations focusing on the introduction of advanced TBC coatings with higher temperature stability and lower thermal conductivity [60]. As mentioned above, the most popular material for TC in TBCs is 7-8 wt. % YSZ. It shows many advantages; however, it suffers from a few drawbacks and limitations. It is possible for the YSZ coating to undergo an adverse phase transformation upon thermal cycling; also, it may be sintered at elevated temperatures during the service period [34].

The coatings deposited by electron-beam physical vapor deposition (EB-PVD) exhibit improved erosion, strain, and thermal shock resistance due to their columnar microstructure [61]. Three types of EB–PVD thermal barrier coatings exist; two-layered, multilayered, and graded TBCs. TBCs with the two-layered structure is the conventional coatings involving the MCrAlY bond coat and YSZ top coat [56]. It has been recently proposed that graded composites of lanthanum hexa-aluminate and alumina present elevated fracture toughness and ductility [47, 62]. The feasibility of functionally graded thermal barrier coatings by spark plasma sintering was also reported [63, 64]. The stress between TC and BC that is the result of different TEC can be relaxed by graded TBCs. A transition layer with alumina between TC and BC is present in these coatings. It has been indicated that the oxidation and thermal shock resistance of graded TBCs are much higher than those of two-layered TBCs [61]. Multi-layered TBCs are commonly utilized for particular applications [56].

4.3. Nano Structure

New proposed structural, chemical, and technological approaches for developing new TBCs are not able to deal with all failure factors. Indeed, enhancements of some properties cause a reduction in other characteristics of the materials [65]. To obtain a combination of desired properties, the TBC architecture can be changed and multilayer coatings with engineered layers can be applied, according to their requirements [66]. Compared to conventional TBCs, nanostructure thermal barrier coatings have shown enhanced thermal insulation property and thermal cycling lifetime. Nanozones that consist of unmelted particles shows an utterly porous morphology. These nanopores are homogeneously distributed and besides microcracks, existing voids, and fine grain structure act as phonon scattering centers. Therefore, the thermal conductivity of the coatings is significantly reduced [34]. It has been reported that nanostructured ceramic coatings have excellent mechanical properties, and high TEC [67-74].

Despite the aforementioned properties, the applicability of nanostructured TBCs is skeptical. It is proposed that when nanostructured YSZ coatings are exposed to high-temperature environments, their densification or sintering rates are higher than that of conventional TBCs [73]. As a result of the high sintering rate, coating stiffening (elastic modulus values) and thermal conductivity/ diffusivity increase beyond critical levels; therefore, it might cause premature failure and limit the application of nanostructured TBCs [73].

5. Self-healing composite TBCs

In the 1970s, self-healing ceramic materials were first introduced. Self-healing materials are able to repair cracks in ceramics upon heat treatment. Many polymeric, metallic, and concrete-based materials have been reported as self-healing materials over the past few years [75]. Majority of studies in the field of self-healing ceramics are allocated to the use of SiC for healing, which occurs through the oxidation of SiC particles and the resulting volume expansion into the cracks [75].

Sloof et al. [76] took the first step to fabricate thermal barrier coatings with self-healing capability. They incorporated boron alloyed $MoSi_2$ (B-$MoSi_2$) into the YSZ coating and indicated that the addition of these particles did not create extra stresses during thermal cycles [77]. In the absence of oxidative atmospheres, B-$MoSi_2$ particles remain solid at 1100 ˚C, and their TEC is close to that of the YSZ matrix. Additionally, the fluidity of SiO_2 at the service temperature increases by alloying the $MoSi_2$ with B, which facilitates the filling of cracks [78]. When cracks are formed, B-$MoSi_2$ particles embedded into the thermal barrier coating are exposed to a high oxygen potential atmosphere followed by the formation of amorphous SiO_2 by the oxidation reaction. Amorphous silica flows into generated cracks and comes into direct contact with their walls. This amorphous oxide then reacts with zirconia and form solid reaction products, mainly $ZrSiO_4$, that adhere to the walls [79]. The mechanism of self-healing in TBCs with $MoSi_2$ particles is shown in Fig. 1.

6. Coating methods

As mentioned earlier, in an oxygen-containing atmosphere, the material is oxidized rapidly at 1000-1200 °C [80]. Besides, due to the very porous structure of YSZ, oxygen easily penetrates YSZ, and the ceramic layer is not able to accommodate the compressive stresses to a specific extent [76, 81]. The thickness of the protective SiO_2 coating on the bulk $MoSi_2$ formed above 800 °C reaches usually several µm; therefore, a significant amount of the material in particles is consumed. Moreover, formed SiO_2 would react with ZrO_2 to form zircon. To prevent these reactions, applying a coating is necessary. Various materials have been studied, such as $ZrSiO_4$, $Al_6Si_2O_{13}$, and Al_2O_3. However, Al_2O_3 is commonly used for coating the self-healing ceramics in TBCs [82]. To enhance their corrosion and oxidation resistance, silicon-containing particles such as $MoSi_2$ and SiC have been coated by Al_2O_3 [83-85].

Atomic layer deposition (ALD) and sol-gel are the two common methods for alumina coating deposition. The sol-gel method is very versatile; however, the system should be in the form of a sol or at least not fully gelated [86]. Although Al_2O_3 is the most studied material prepared by sol-gel, the majority of investigations are associated with bulk Al_2O_3, particularly for catalytic applications. For the production of particles from the environment, several studies have been carried out on particle

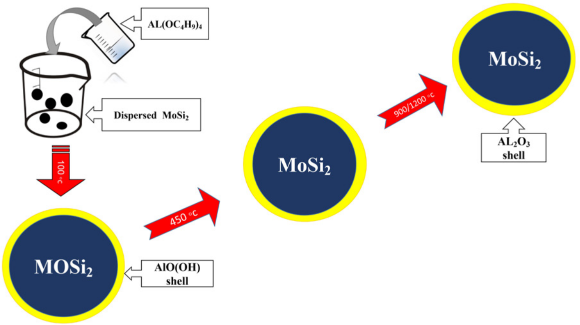

Fig. 2. Coating of $MoSi_2$ particles by the sol-gel method.

coating by sol-gel, for instance, on SiC [87, 88], magnetic particles [89], and phosphors [90]. As a result of very similar surfaces (a native SiO_2 layer), there have been several useful investigations of alumina coating on SiC by the sol-gel method; however, studies on $MoSi_2$ sol-gel coating with Al_2O_3 are rare [91]. The sol-gel production of the Al_2O_3 coating on $MoSi_2$ particles is shown schematically in Fig. 2.

ALD is a technique based on chemical vapor deposition, which is an important method to deposit thin films from gas-phase reactants. In this technique, two self-limiting half-reactions occur for the deposition of solid films on the surface. Controlling the thickness of the film is possible due to these self-limiting reactions [92]. ALD is mainly used for the deposition of thin coatings on relatively flat substrates and wafers. Although there are some challenges regarding deposition on particles, it is possible to use this technique for particles. Particles possess a significantly larger surface area compared to wafers requiring the supply of more reactants. The slow mass transfer occurring in a bed of particles is another problem associated with the particle coating, even in the case of high porosity. This leads to the formation of non-homogeneous coatings [93, 94].

Using a fluidized bed is a solution to these problems. In this process, the particles are suspended in a gas flow by blowing the gas with sufficient velocity through the bed of particles. As a result, both the gas and particles act as fluids enhancing contact and mixing gas and solid enormously [95].

7. Self-healing mechanism in thermal barrier coatings

The addition of SiC particles to brittle materials such as mullite ($3Al_2O_3{\cdot}2SiO_2$), Al_2O_3, and Si_3N_4 could increase the toughness of these materials and it also could give self-healing capability to these materials [96-98]. When SiC particles interact with cracks at high temperatures, SiC reacts with O_2 resulting in the formation of a silica-based reaction product with volume expansion, which flows into the crack [64]. It is desirable to use self-repair mechanisms at high temperatures to enhance the lifetime of TBC coatings. Using $MoSi_2$ particles in the YSZ matrix for high-temperature crack-healing has been reported [79, 99]. The healing ability of $MoSi_2$ particles is due to the release of viscous SiO_2 into the cracks and a subsequent reaction of the formed SiO_2 with the matrix through a solid-state reaction. As a result of the reaction, load-bearing crystalline $ZrSiO_4$ is formed, providing enhanced adhesion between the fractured surface and the healing agent [100].

The porous structure of YSZ facilitates the diffusion of oxygen, which might lead to the premature oxidation of the particles, even in the absence of cracks interfering in the healing process in TBCs [101]. Therefore, to prohibit the premature initiation of the healing mechanism in TBCs and maintain the particles in a dormant state, it is required to apply an inert shell that is impenetrable against oxygen on the surface of the actual intermetallic particles [102]. The ideal material for the protection of the particles is α-alumina, due to a low permeability for oxygen [103, 104] and good thermal stability [105]. When a crack penetrates the Al_2O_3 shell surrounding active $MoSi_2$, the healing mechanism is activated [17].

The healing agent incorporated in thermal barrier coatings should have some properties [106] including:1) it should be in the solid phase at the operating temperature because liquids have a large thermal conductivity and large TEC; 2) it should be turned into a liquid to wet the crack surfaces and fill the crack; 3) the liquid medium should turn into a solid phase by the reaction between the TBC material and the liquid phase through a solid-state chemical reaction. As a result of this process, the crack is healed by a well-bonded crystalline material having low thermal conductivity [107].

The high-temperature oxidation of $MoSi_2$ has been studied extensively, due to its use as heating elements in many high-temperature furnaces. There are two oxidizable components in the system: molybdenum and silicon, which make the behavior of the system rather complex [108]. The oxidation temperature of $MoSi_2$ ranges between 400 and 500 °C, and at temperatures lower than 800 °C, reaction starts as follow:

$$2\ MoSi_2\ (s) + 7\ O_2\ (g) \rightarrow 2\ MoO_3\ (s) + 4\ SiO_2\ (s)\ (<800\ ^{o}C) \qquad (1)$$

Zhu et al. [76] found that above the melting point of MoO_3 (approximately 800 °C), the formation of Mo_5Si_3 and SiO_2 is more thermodynamically favored than that of MoO_3, according to reaction 3.2. Mo_5Si_3 can be further oxidized in the presence of adequate oxygen (according to reaction 3.3). At this temperature, however, the vapor pressure of MoO_3 becomes significant, causing most of MoO_3 to be removed. Therefore, the formation of the SiO_2 scale starts at 800 °C, protecting the $MoSi_2$ and Mo_5Si_3 phases.

$$5\ MoSi_2\ (s) + 7\ O_2\ (g) \rightarrow Mo5Si_3\ (s) + 7\ SiO_2\ (s)\ (>800\ ^{o}C) \qquad (2)$$

$$Mo5Si_3\ (s) + 10.5\ O_2\ (g) \rightarrow 5\ MoO_3\ (g) + 3\ SiO_2\ (s)\ (>800\ ^{o}C) \qquad (3)$$

Porosity in the formed scale due to the significant formation of MoO_3 below 800 °C occurs as a phenomenon referred to the oxidation of $MoSi_2$, which prevents a protective coating formation. If no initial protective coating is formed, oxidation of $MoSi_2$ continues at high rates, which is a challenge in bulk $MoSi_2$ applications. However, a protective coating is needed for particles due to the required thickness of the SiO_2 coatings in several µm, which is already mentioned in the theory section [109]. Therefore, the consumption of a significant part of the healing particle to form this coating is necessary.

Attempts have been made to alloy $MoSi_2$ with boron and aluminum, due to its interesting high-temperature properties and intermetallic nature [110]. Mao found that boron stabilizes the amorphous phase of SiO_2. On the contrary, $MoSi_2$ tends to form separate phases with molybdenum. However, in the presence of molybdenum, no borides are formed from the reaction of boron and silicon [111].

The results indicate that only boron may form a separate phase with molybdenum, which mainly depends on the applied processing conditions for the production of $MoSi_2$. As most of the molybdenum borides have a significant high hardness, boron may increase $MoSi_2$ hardness [112]. In the structure of $MoSi_2$, Al can easily substitute B, although it stabilizes the metastable $MoSi_2$ hexagonal phase [113]. As a result, a single phase of $MoSi_xAl_y$ or a two-phase system with both the hexagonal and tetragonal phase of $MoSi_xAl_y$ coexists, depending on the molar ratios of the present elements.

However, the main effect of the presence of aluminum is on its oxidation behavior. In fact, aluminum is preferentially oxidized and reduces SiO_2, according to reaction 3.4. This is due to lower ΔG of Al_2O_3 per mole of oxygen than that of either Mo or Si [114]. As a result, pest oxidation is limited and the Al_2O_3 scale is formed instead of the SiO_2 scale [115], depending on the local Si, Al and, O activities.

$$4\ Al\ (s) + 3\ SiO_2\ (s) \rightarrow 2\ Al_2O_3\ (s) + 3\ Si\ (s) \qquad (4)$$

The oxidation of components in $MoSi_2$ and subsequent formation of

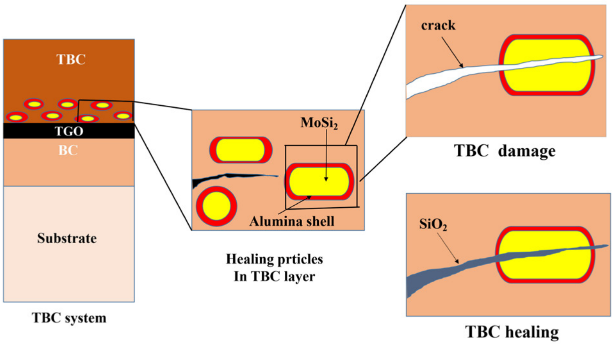

Fig. 3. Preparation of self-healing TBCs using SPS.

ternary oxides lead to significant changes in molar volume and help to fill and close cracks that are desired for the self-healing process. Premature oxidation also results in the accumulation of stress and subsequently coating fracture, as mentioned in the theory section [116].

8. Application of self-healing composites in TBCs

The material chosen as a healing agent for an autonomous self-healing TBC must fulfill criteria as follows: (i) the healing material should have a melting temperature higher than 1000 °C (maximum TBC operating temperature), and its TEC should match the TBC materials, (ii) it should be oxidized and transformed into a liquid to fill cracks and provide direct contact with the surfaces of cracks, (iii) it should be able to wet the crack faces and form a load-bearing material through a solid-state chemical reaction between the TBC material and the liquid [79].

Nozahic et al. [64] embedded encapsulated MoSi$_2$ (B) particles in the YSZ coating to prepare a self-healing TBC. The composite coating deposition on a Ni-based superalloy was carried out using spark plasma sintering (SPS). The coating process is shown in Fig. 3. According to the results, no cracks resulting from thermally induced stresses appeared in the SPS-sintered TBC. This is the result of the CTE difference of the YSZ matrix and MoSi$_2$-based particles.

Ouyang et al. [75] showed that the self-healing agent TiC in YSZ/Al$_2$O$_3$/TiC composite coatings was able to release TiO$_2$ to heal the pores and cracks in the coatings. Pre-oxidation treatment of the self-healing coating based on TiC in the furnace at 600^{o}C may form a self-healing layer with low-porosity at the interface between TC and BC, and as a result, it could prevent the formation and growth of the detrimental oxide materials. Hence, the oxidation resistance of the coating was improved by the self-healing process. Nevertheless, according to the thermal cycle test, a thick layer of the TiC-self-healing coating induced the stress above the stress limit in ceramic coatings.

Ouyang et al. [117] used APS to fabricate self-healing TBCs based on YSZ/SiC-self-healing (SAZ) structure. They demonstrated that the self-healing occurred during SAZ coating after oxidation at the temperature of 720°C, which resulted in filling the remaining cracks/pores in the SAZ coating. Moreover, due to the comprised oxidation resisting materials, Al$_2$O$_3$ in the SAZ coating and its dense structure, the oxidation resistance of TBCs was improved after coating with SAZ. Consequently, the resistance against spallation in the YSZ/SAZ also increased, which was verified using an ideal mode assessing the TBC stress intensity. They also applied a cyclic high-temperature oxidation test on YSZ and YSZ/SAZ coatings. The results showed that the spallation resistance was increased in the YSZ/SAZ coatings by a thoughening effect occurred after high-temperature oxidation.

Nguyen et al. [118] developed a self-healing material based on a composite of Ni and Y$_2$Ti$_2$O$_7$. In order to study the crack-healing behavior, Vickers indenter was employed to intentionally generate the cracks on the surface of the composite, followed by an annealing process in an oxidizing atmosphere. They suggest that the depositing of NiO into the cracks is the main crack-healing mechanism. In fact, the oxidation of the Ni fillers led to the formation of NiO during annealing. According to XRD and SEM results, the complete healing of the cracks was obtained using 10 vol% Ni filler.

Kulczyk-Malecka et al. [119] established Yttria–partially stabilized zirconia (YPSZ)/MoSi$_2$ composites to render self-healing ability and enhance the thermal stability of the matrix. In this method, decomposition of MoSi$_2$ at the elevated temperatures results in the volumetrically expanding product which heals the cracks. Furthermore, they focused on the comparison between the conventional YPSZ and the composites containing MoSi$_2$ particles in terms of the TEC and the fracture toughness. It was found that the produced MoSi$_2$ composites have a similar TEC and fracture toughness to the conventional YPSZ, indicating small mismatch stresses induced by elevated temperature. The cracks introduced by indentation have shown such a composite system is able to independently perform the self-healing reaction.

Kurniadi et al. [120] encapsulate MoSi$_2$B particles in YSZ coatings using a novel approach for in situ shell formation. The healing particles were alloyed with Al. The results showed that the addition of 12 wt% of Al resulted in a homogeneous distribution of Mo(Si$_{1-x}$,Al$_x$)$_2$ and the formation of exclusive alumina through selective oxidation of aluminum at 1100˚C. In comparison with pure Argon, oxidation in lower O$_2$ pressure using CO/CO$_2$ led to a more exclusive alumina formation. But, composite oxidation in the CO/CO$_2$ exhibited the simultaneous formation of Al oxide, Si oxide, and mixed alumina-silica. This shows that partial reduction of YSZ plays a role in particle oxidizing. However, the shell provided protection for particles was observed in microcapsule stability test in laboratory air and at 1100˚C for 100 h. The crack-gap filling experiment demonstrated no significant difference in the healing behavior of in situ encapsulated MoSi$_2$B and pre-encapsulated when the composites were exposed to the temperature of 1100 °C for 16 h.

Wang et al. [77] developed YSZ-La-Mo-Si coatings (YSZ-LMS) using the plasma spraying method for protecting carbon/carbon (C/C) composites. Raw materials for the production of the coating were YSZ, MoSi$_2$, and LaB$_6$. The results showed that the YSZ-LMS coating protected the composites at 1500 °C for 50 h. A denser oxide glass layer of Zr-Y-La-Si-O was formed due to the formation of La$_2$O$_3$, Y$_2$SiO$_5$, ZrSiO$_4$, and SiO$_2$, which leads to the solid phase volume expansion and a decrease in the SiO$_2$ volatilization. As a result of the volume expansion at high temperatures, compressive stress is generated within the coating restraining the crack initiation and propagation, leading to the improvement of the oxidation resistance of the coatings. The activation energy of high-temperature oxidation for the coated C/C composites was obtained to be 74.466 kJ mol^{-1} at 1300-1500 °C.

To prepare TBCs with the self-healing ability, Carnicer et al. [121] used an aqueous suspension of Al$_2$O$_3$ and SiCY-TZP. To prevent the SiC oxidation as a self-healing agent, suspension plasma spraying was utilized for the deposition of the coating. The results demonstrated that the SiC particles were oxidized during the PS process and the dispersion of the unmelted particles was observed in a partially melted Al$_2$O$_3$/Y-TZP matrix. This reveals the potential self-healing ability of the prepared coating.

Using embedded MoSi$_2$(B) healing particle oxidation, Derelioglu et al. [79] developed a new method for the fabrication of self-healing TBCs. The oxidative decomposition of the healing agents resulted in the amorphous SiO$_2$ formation which flowed into created cracks and wetted the crack faces. Thereafter, solid ZrSiO$_4$ was formed due to the reaction between SiO$_2$ and ZrO$_2$ based TBC coating establishing a strong bond between the matrix material and the healing agent causing a complete filling of cracks. Even when cracks are not present in the coating, the decomposition reaction can occur resulting from the oxygen transparency of the ZrO_2-based matrix. This led to premature decomposition and undesirable pore filling of the coatings.

In general, the self-healing TBC samples made by SPS indicate an enhanced resistance against thermal cycling in the air at the temperature of 1100 °C. The results show that the borosilicate or silicate phase partially fills some cracks and there is a zircon phase that connects both surfaces of the crack. The intended self-healing effect of partially yttria-stabilized zirconia-based TBCs reinforced with $MoSi_2(B)$-based particles was confirmed by the observations [64, 122, 123].

9. Conclusions and future insights

Thermal barrier coatings have been offered for several applications in the industry to improve the efficiency of advanced gas-turbine engines. SiC, $MoSi_2$, TiC, etc. have been shown to act as a self-healing agent and are able to heal the cracks/pores in the coatings. The good resistance of self-healing TBC samples against thermal cycling at high temperatures in the air indicates the feasibility and the good performance of these coatings in-service conditions. It has been deduced that the borosilicate or silicate phase partially fills some cracks and there is a zircon phase that connects the surfaces of cracks. In the near future, hopefully, other composite materials will be tested for self-healing applications in TBCs and a further improvement in the physical and thermal properties of the barrier coatings will be investigated.

REFERENCES

[1] B. Zhou, S. Yang, C. Wang, X. Hu, W. Song, J. Cai, Q. Xu, N. Sang, The characterization of free radical reaction in coal low-temperature oxidation with different oxygen concentration, Fuel 262 (2020) 116524.

[2] I. Tajzad, E. Ghasali, Production methods of CNT-reinforced Al matrix composites: a review, Journal of Composites and Compounds 2(1) (2020) 1-9.

[3] J. Daraei, Production and characterization of PCL (Polycaprolactone) coated TCP/nanoBG composite scaffolds by sponge foam method for orthopedic applications, Journal of Composites and Compounds 2(1) (2020) 45-50.

[4] Z. Goudarzi, A. Ijadi, A. Bakhtiari, S. Eskandarinezhad, N. Azizabadi, M.A. Jazi, Sr-doped bioactive glasses for biological applications, Journal of Composites and Compounds 2(3) (2020) 105-109.

[5] H. Ullah, K.A. M Azizli, Z.B. Man, M.B.C. Ismail, M.I. Khan, The Potential of Microencapsulated Self-healing Materials for Microcracks Recovery in Self-healing Composite Systems: A Review, Polymer Reviews 56(3) (2016) 429-485.

[6] S.O. Omid, Z. Goudarzi, L.M. Kangarshahi, A. Mokhtarzade, F. Bahrami, Self-expanding stents based on shape memory alloys and shape memory polymers, Journal of Composites and Compounds 2(3) (2020) 92-98.

[7] M. Arefian, M. Hojjati, I. Tajzad, A. Mokhtarzade, M. Mazhar, A. Jamavari, A review of Polyvinyl alcohol/Carboxiy methyl cellulose (PVA/CMC) composites for various applications, Journal of Composites and Compounds 2(3) (2020) 69-76.

[8] F. Nozahic, D. Monceau, C. Estournès, Thermal cycling and reactivity of a $MoSi_2/ZrO_2$ composite designed for self-healing thermal barrier coatings, Materials & Design 94 (2016) 444-448.

[9] Z. Derelioglu, S. Ponnusami, S. Turteltaub, S. Van der Zwaag, W. Sloof, Healing particles in self-healing thermal barrier coatings, (2013).

[10] S. Nasibi, K. Alimohammadi, L. Bazli, S. Eskandarinezhad, A. Mohammadi, N. Sheysi, TZNT alloy for surgical implant applications: A systematic review, Journal of Composites and Compounds 2(3) (2020) 62-68.

[11] M.D. Hager, Self-healing materials, Handbook of Solid State Chemistry (2017) 201-225.

[12] K. Zhang, H.W. Jang, Q. Van Le, Production methods of ceramic-reinforced Al-Li matrix composites: A review, Journal of Composites and Compounds 2(3) (2020) 77-84.

[13] L.-Y. Yu, R.-L. Li, H.-L. Wu, S.-F. Zhang, M.-W. Chai, X.-X. Shen, M. Hong, H. Lin, Selective Removal of Cu^{2+} Ion in Aqueous Solution by Poly (Acrylic Acid/Acrylamide) Hydrogel, Chinese Journal of Analytical Chemistry 48(8) (2020) e20098-e20106.

[14] C. Chen, S. Chen, Z. Guo, W. Hu, Z. Chen, J. Wang, J. Hu, J. Guo, L. Yang, Highly efficient self-healing materials with excellent shape memory and unprecedented mechanical properties, Journal of Materials Chemistry A (2020).

[15] Z.-Y. Wei, B. Cheng, J. Wang, M.-J. Liu, H.-N. Cai, Extend the thermal cyclic lifetime of $La_2Zr_2O_7$/YSZ DCL TBCs by reducing modulus design on a toughening ceramic surface, Surface and Coatings Technology 374 (2019) 134-143.

[16] H. Xia, C. Li, H. Chen, Green preparation of CuI particles in dielectric barrier discharge for colorimetric determination of trace mercury in comparison with atomic fluorescence spectrometric determination, Microchemical Journal 146 (2019) 1169-1172.

[17] A.L. Carabat, M.J. Meijerink, J.C. Brouwer, E.M. Kelder, J.R. van Ommen, S. van der Zwaag, W.G. Sloof, Protecting the $MoSi_2$ healing particles for thermal barrier coatings using a sol-gel produced Al_2O_3 coating, Journal of the European Ceramic Society 38(7) (2018) 2728-2734.

[18] M. Belmonte, Advanced Ceramic Materials for High Temperature Applications, Advanced Engineering Materials 8(8) (2006) 693-703.

[19] F. Cernuschi, P. Bison, A. Moscatelli, Microstructural characterization of porous thermal barrier coatings by laser flash technique, Acta Materialia 57(12) (2009) 3460-3471.

[20] M. Dietrich, V. Verlotski, R. Vassen, D. Stöver, Metal-Glass Based Composites for Novel TBC-Systems, Materialwissenschaft und Werkstofftechnik: Materials Science and Engineering Technology 32(8) (2001) 669-672.

[21] T. Ouyang, X. Fang, Y. Zhang, D. Liu, Y. Wang, S. Feng, T. Zhou, S. Cai, J. Suo, Enhancement of high temperature oxidation resistance and spallation resistance of SiC-self-healing thermal barrier coatings, Surface and Coatings Technology 286 (2016) 365-375.

[22] C. Yu, H. Liu, C. Jiang, Z. Bao, S. Zhu, F. Wang, Modification of NiCoCrAlY with Pt: Part II. Application in TBC with pure metastable tetragonal (t′) phase YSZ and thermal cycling behavior, Journal of materials science & technology 35(3) (2019) 350-359.

[23] G. Pulci, J. Tirillò, F. Marra, F. Sarasini, A. Bellucci, T. Valente, C. Bartuli, High temperature oxidation of MCrAlY coatings modified by Al_2O_3 PVD overlay, Surface and Coatings Technology 268 (2015) 198-204.

[24] K.M. Doleker, Y. Ozgurluk, A.C. Karaoglanli, Isothermal oxidation and thermal cyclic behaviors of YSZ and double-layered YSZ/$La_2Zr_2O_7$ thermal barrier coatings (TBCs), Surface and Coatings Technology 351 (2018) 78-88.

[25] M. Mohammadi, A. Kobayashi, S. Javadpour, S. Jahromi, Evaluation of hot corrosion behaviors of Al_2O_3-YSZ composite TBC on gradient MCrAlY coatings in the presence of Na_2SO_4-$NaVO_3$ salt, Vacuum 167 (2019) 547-553.

[26] S. Mahade, D. Zhou, N. Curry, N. Markocsan, P. Nylén, R. Vaßen, Tailored microstructures of gadolinium zirconate/YSZ multi-layered thermal barrier coatings produced by suspension plasma spray: Durability and erosion testing, Journal of Materials Processing Technology 264 (2019) 283-294.

[27] M. Bahamirian, S. Hadavi, M. Farvizi, A. Keyvani, M. Rahimipour, Thermal Durability of YSZ/Nanostructured $Gd_2Zr_2O_7$ TBC Undergoing Thermal Cycling, Oxidation of Metals 92(5-6) (2019) 401-421.

[28] J. Wang, J. Sun, Q. Jing, B. Liu, H. Zhang, Y. Yongsheng, J. Yuan, S. Dong, X. Zhou, X. Cao, Phase stability and thermo-physical properties of ZrO_2-CeO_2-TiO_2 ceramics for thermal barrier coatings, Journal of the European Ceramic Society 38(7) (2018) 2841-2850.

[29] N. Ejaz, L. Ali, A. Ahmad, M. Mansoor, M.M. Asim, A. Rauf, K. Mehmood, Thermo-Physical Properties Measurement of Advanced TBC Materials with Pyrochlore and Perovskite Structures, Key Engineering Materials, Trans Tech Publ, 2018, pp. 236-244.

[30] A.A. Abubakar, A.F.M. Arif, S.S. Akhtar, Evolution of internal cracks and residual stress during deposition of TBC, Ceramics International (2020).

[31] A. Ghoshal, M. Murugan, M.J. Walock, A. Nieto, L. Bravo, B. Barnett, M. Pepi, C. Hoffmeister Mock, J. Swab, S. Hirsch, Sandphobic coatings and surface modification of hot section components of next generation VTOL engines: current and future research efforts, 2018 Joint Propulsion Conference, 2018, p. 4831.

[32] O.P. Golim, N. Prastomo, H. Izzudin, S. Hastuty, R. Sundawa, E. Sugiarti, K.A.Z. Thosin, Synthesis of alumina ceramic encapsulation for self-healing materials on thermal barrier coating, Journal of Physics: Conference Series 985 (2018) 012036.

[33] L. Lim, S. Meguid, Modeling and characterisation of depletion of aluminium in bond coat and growth of mixed oxides in thermal barrier coatings, International Journal of Mechanics and Materials in Design (2019) 1-17.

[34] A.H. Pakseresht, Production, Properties, and Applications of High Temperature Coatings, IGI Global2018.

[35] J. Jiang, L. Jiang, Z. Cai, W. Wang, X. Zhao, Y. Liu, Z. Cao, Numerical stress analysis of the TBC-film cooling system under operating conditions considering the effects of thermal gradient and TGO growth, Surface and Coatings Technology 357 (2019) 433-444.

[36] R. Takahashi, J. Assis, F.P. Neto, D. Reis, Heat treatment for TGO growth on NiCrAlY for TBC application, Materials Research Express 6(12) (2020) 126442.

[37] X. Zhang, K. Zhou, M. Liu, C. Deng, C. Deng, J. Mao, Z. Deng, Mechanisms governing the thermal shock and tensile fracture of PS-PVD 7YSZ TBC, Ceramics International 44(4) (2018) 3973-3980.

[38] J. Kulczyk-Malecka, X. Zhang, J. Carr, F. Nozahic, C. Estournès, D. Monceau, A.L. Carabat, W.G. Sloof, S. van der Zwaag, P.J. Withers, P. Xiao, Thermo – mechanical properties of SPS produced self-healing thermal barrier coatings containing pure and alloyed $MoSi_2$ particles, Journal of the European Ceramic Society 38(12) (2018) 4268-4275.

[39] J. Mitrić, J. Križan, J. Trajić, G. Križan, M. Romčević, N. Paunović, B. Vasić, N. Romčević, Structural properties of Eu^{3+} doped $Gd_2Zr_2O_7$ nanopowders: Far-infrared spectroscopy, Optical Materials 75 (2018) 662-665.

[40] G. Moskal, A. Jasik, M. Mikuśkiewicz, S. Jucha, Thermal resistance determination of $Sm_2Zr_2O_7$ + 8YSZ composite type of TBC, Applied Surface Science 515 (2020) 145998.

[41] M. Gupta, N. Markocsan, X.-H. Li, R.L. Peng, Improving the lifetime of suspension plasma sprayed thermal barrier coatings, Surface and Coatings Technology 332 (2017) 550-559.

[42] Y. Fukushima, M. Arai, K. Ito, T. Suidzu, Fusion and TBC Penetration Characteristics of Volcanic Ash Collected from Active Volcano, Journal of Thermal Spray Technology (2020) 1-15.

[43] S. Budinovskii, D. Chubarov, P. Matveev, A. Smirnov, Deposition and Properties of the Ceramic TBC Layer Prepared by Magnetron Sputtering, Russian Metallurgy (Metally) 2019(12) (2019) 1280-1284.

[44] X. Cao, R. Vassen, W. Fischer, F. Tietz, W. Jungen, D. Stöver, Lanthanum–Cerium Oxide as a Thermal Barrier-Coating Material for High-Temperature Applications, Advanced Materials 15(17) (2003) 1438-1442.

[45] H. Zhang, J. Zeng, J. Yuan, P. Liang, X. Zhou, S. Chen, S. Duo, S. Dong, J. Jiang, L. Deng, Spray power-governed microstructure and composition, and their effects on properties of lanthanum-cerium-tantalum-oxide thermal barrier coating, Ceramics International (2020).

[46] Y. Bai, W. Fan, K. Liu, Y. Kang, Y. Gao, F. Ma, Gradient $La_2Ce_2O_7$/YSZ thermal barrier coatings tailored by synchronous dual powder feeding system, Materials Letters 219 (2018) 55-58.

[47] R. Vaßen, M.O. Jarligo, T. Steinke, D.E. Mack, D. Stöver, Overview on advanced thermal barrier coatings, Surface and Coatings Technology 205(4) (2010) 938-942.

[48] G. Moskal, Microstructure and thermal properties of Sm.

[49] K.M. Doleker, Y. Ozgurluk, H. Ahlatci, A.C. Karaoglanli, Evaluation of oxidation and thermal cyclic behavior of YSZ, $Gd_2Zr_2O_7$ and YSZ/$Gd_2Zr_2O_7$ TBCs, Surface and Coatings Technology 371 (2019) 262-275.

[50] R. Ianoş, P. Barvinschi, Solution combustion synthesis of calcium zirconate, $CaZrO_3$, powders, Journal of solid state chemistry 183(3) (2010) 491-496.

[51] K. Neufuss, J. Dubsky, P. Rohan, B. Kolman, P. Chraska, L.-M. Berger, R. Zieris, S. Thiele, M. Nebelung, Structure and properties of $CaZrO_3$ coatings prepared by WSP and APS spraying, ITSC 2003: International Thermal Spray Conference 2003: Advancing the Science and Applying the Technology, 2003, pp. 1541-1546.

[52] M. Pollet, S. Marinel, G. Desgardin, $CaZrO_3$, a Ni-co-sinterable dielectric material for base metal-multilayer ceramic capacitor applications, Journal of the European Ceramic Society 24(1) (2004) 119-127.

[53] G. Di Girolamo, F. Marra, M. Schioppa, C. Blasi, G. Pulci, T. Valente, Evolution of microstructural and mechanical properties of lanthanum zirconate thermal barrier coatings at high temperature, Surface and Coatings Technology 268 (2015) 298-302.

[54] L.A. Noveed Ejaz*, Akhlaq Ahmad, Muhammad Mansoor, Muhammad Muneeb Asim, Abdul Rauf, Khalid Mehmood, Thermo-Physical Properties Measurement of Advanced TBC Materials with Pyrochlore and Perovskite Structures, 778 (2018).

[55] Z. Yang, P. Zhang, W. Pan, Y. Han, M. Huang, H. Chen, Q. Gong, C. Wan, Thermal and oxygen transport properties of complex pyrochlore RE_2InTaO_7 for thermal barrier coating applications, Journal of the European Ceramic Society (2020).

[56] H. Xu, H. Guo, Thermal barrier coatings, Elsevier2011.

[57] H. Lau, Influence of yttria on the cyclic lifetime of YSZ TBC deposited on EB-PVD NiCoCrAlY bondcoats and its contribution to a modified TBC adhesion mechanism, Surface and Coatings Technology 235 (2013) 121-126.

[58] S. Nouri, S. Sahmani, M. Asayesh, M. Aghdam, Improvement of high-temperature oxidation resistance of γ-TiAl intermetallic alloy by YSZ-NiCoCrAlY coating using APS process, Materials Research Express 6(12) (2019) 126541.

[59] J. Shi, T. Zhang, B. Sun, B. Wang, X. Zhang, L. Song, Isothermal oxidation and TGO growth behavior of NiCoCrAlY-YSZ thermal barrier coatings on a Ni-based superalloy, Journal of Alloys and Compounds 844 (2020) 156093.

[60] M. Peters, C. Leyens, U. Schulz, W.A. Kaysser, EB-PVD thermal barrier coatings for aeroengines and gas turbines, Advanced engineering materials 3(4) (2001) 193-204.

[61] L.B. Chen, Yttria-stabilized zirconia thermal barrier coatings-a review, Surface Review and Letters 13(05) (2006) 535-544.

[62] B.R. Lawn, N.P. Padture, H. Cait, F. Guiberteau, Making ceramics" ductile", Science 263(5150) (1994) 1114-1116.

[63] A.H. Pakseresht, A.H. Javadi, M. Bahrami, F. Khodabakhshi, A. Simchi, Spark plasma sintering of a multilayer thermal barrier coating on Inconel 738 superalloy: Microstructural development and hot corrosion behavior, Ceramics International 42(2, Part A) (2016) 2770-2779.

[64] F. Nozahic, C. Estournès, A.L. Carabat, W.G. Sloof, S. van der Zwaag, D. Monceau, Self-healing thermal barrier coating systems fabricated by spark plasma sintering, Materials & Design 143 (2018) 204-213.

[65] S.-J. Park, M.-K. Seo, T.-J. Ma, D.-R. Lee, Effect of chemical treatment of Kevlar fibers on mechanical interfacial properties of composites, Journal of colloid and interface science 252(1) (2002) 249-255.

[66] A.H. Pakseresht, A.H. Javadi, E. Ghasali, A. Shahbazkhan, S. Shakhesi, Evaluation of hot corrosion behavior of plasma sprayed thermal barrier coatings with graded intermediate layer and double ceramic top layer, Surface and Coatings Technology 288 (2016) 36-45.

[67] N.P. Padture, M. Gell, E.H. Jordan, Thermal barrier coatings for gas-turbine engine applications, Science 296(5566) (2002) 280-284.

[68] A. Aygun, A.L. Vasiliev, N.P. Padture, X. Ma, Novel thermal barrier coatings that are resistant to high-temperature attack by glassy deposits, Acta Materialia 55(20) (2007) 6734-6745.

[69] B. Ercan, K.J. Bowman, R.W. Trice, H. Wang, W. Porter, Effect of initial powder morphology on thermal and mechanical properties of stand-alone plasma-sprayed 7 wt.% Y_2O_3–ZrO_2 coatings, Materials Science and Engineering: A 435 (2006) 212-220.

[70] L. Xie, D. Chen, E.H. Jordan, A. Ozturk, F. Wu, X. Ma, B.M. Cetegen, M. Gell, Formation of vertical cracks in solution-precursor plasma-sprayed thermal barrier coatings, Surface and Coatings Technology 201(3-4) (2006) 1058-1064.

[71] G. Shanmugavelayutham, A. Kobayashi, Mechanical properties and oxidation behaviour of plasma sprayed functionally graded zirconia–alumina thermal barrier coatings, Materials chemistry and physics 103(2-3) (2007) 283-289.

[72] B.-K. Jang, H. Matsubara, Influence of porosity on thermophysical properties of nano-porous zirconia coatings grown by electron beam-physical vapor deposition, Scripta materialia 54(9) (2006) 1655-1659.

[73] R. Lima, B. Marple, Nanostructured YSZ thermal barrier coatings engineered to counteract sintering effects, Materials Science and Engineering: A 485(1-2) (2008) 182-193.

[74] H. Chen, X. Zhou, C. Ding, Investigation of the thermomechanical properties of a plasma-sprayed nanostructured zirconia coating, Journal of the European Ceramic Society 23(9) (2003) 1449-1455.

[75] T. Ouyang, J. Wu, M. Yasir, T. Zhou, X. Fang, Y. Wang, D. Liu, J. Suo, Effect of TiC self-healing coatings on the cyclic oxidation resistance and lifetime of thermal barrier coatings, Journal of Alloys and Compounds 656 (2016) 992-1003.

[76] W.G. Sloof, Self healing in coatings at high temperatures, Self healing materials, Springer2007, pp. 309-321.

[77] C. Wang, K. Li, X. Shi, J. Sun, Q. He, C. Huo, Self-healing YSZ-La-Mo-Si heterogeneous coating fabricated by plasma spraying to protect carbon/carbon composites from oxidation, Composites Part B: Engineering 125 (2017) 181-194.

[78] S.T. Nguyen, T. Nakayama, M. Takeda, N.N. Hieu, T. Takahashi, Development of Yttrium Titanate/Nickel Nanocomposites with Self Crack-Healing Ability and Potential Application as Thermal Barrier Coating Material, MATERIALS TRANSACTIONS (2020) MT-MN2019006.

[79] Z. Derelioglu, A.L. Carabat, G.M. Song, S.v.d. Zwaag, W.G. Sloof, On the use of B-alloyed $MoSi_2$ particles as crack healing agents in yttria stabilized zirconia thermal barrier coatings, Journal of the European Ceramic Society 35(16) (2015) 4507-4511.

[80] H.E. Eaton, G.D. Linsey, E.Y. Sun, K.L. More, J.B. Kimmel, J.R. Price, N. Miriyala, EBC protection of SiC/SiC composites in the gas turbine combustion environment: continuing evaluation and refurbishment considerations, Turbo Expo: Power for Land, Sea, and Air, American Society of Mechanical Engineers, 2001, p. V004T02A010.

[81] S.C. Singhal, Advances in solid oxide fuel cell technology, Solid state ionics 135(1-4) (2000) 305-313.

[82] M.J. Meijerink, Coating of $MoSi_2$ healing particles for self-healing thermal barrier coatings, Chemical Engineering Materials Science and Engineering (2015).

[83] R. Dutton, R. Wheeler, K. Ravichandran, K. An, Effect of heat treatment on the thermal conductivity of plasma-sprayed thermal barrier coatings, Journal of

Thermal Spray Technology 9(2) (2000) 204-209.

[84] S. Maria Jose, C.T. Mathew, J. K.Thomas, Fabrication of Dysprosium doped Y_2O_3 infrared transparent ceramic materials by a microwave sintering technique, Materials Today: Proceedings 24 (2020) 2383-2393.

[85] M. Pavić-Čolić, Multi-velocity and multi-temperature model of the mixture of polyatomic gases issuing from kinetic theory, Physics Letters A 383(24) (2019) 2829-2835.

[86] N. Avci, I. Cimieri, P.F. Smet, D. Poelman, Stability improvement of moisture sensitive CaS: Eu^{2+} micro-particles by coating with sol–gel alumina, Optical Materials 33(7) (2011) 1032-1035.

[87] J.J. Gibson, Y. Yi, S.J. Birks, Watershed, climate, and stable isotope data (oxygen-18 and deuterium) for 50 boreal lakes in the oil sands region, northeastern Alberta, Canada, 2002–2017, Data in Brief 29 (2020) 105308.

[88] P. Benda, A. Kalendová, Anticorrosion Properties of Pigments based on Ferrite Coated Zinc Particles, Physics Procedia 44 (2013) 185-194.

[89] S. Rabadzhiyska, L. Kolaklieva, V. Chitanov, T. Cholakova, R. Kakanakov, N. Dimcheva, K. Balashev, Mechanical, wear and corrosion behavior of CrN/TiN multilayer coatings deposited by low temperature unbalanced magnetron sputtering for biomedical applications, Materials Today: Proceedings 5(8, Part 2) (2018) 16012-16021.

[90] L.W. Martin, Y.H. Chu, R. Ramesh, Advances in the growth and characterization of magnetic, ferroelectric, and multiferroic oxide thin films, Materials Science and Engineering: R: Reports 68(4) (2010) 89-133.

[91] R. Mateos, G. Baeza, B. Sarriá, L. Bravo, Improved LC-MSn characterization of hydroxycinnamic acid derivatives and flavonols in different commercial mate (Ilex paraguariensis) brands. Quantification of polyphenols, methylxanthines, and antioxidant activity, Food Chemistry 241 (2018) 232-241.

[92] M. Tomczyk, A. Mahajan, A. Tkach, P.M. Vilarinho, Interface-based reduced coercivity and leakage currents of $BiFeO_3$ thin films: A comparative study, Materials & Design 160 (2018) 1322-1334.

[93] S. Bhattacharya, K. Mo, Z. Mei, D. Seidman, B. Stepnik, M.J. Pellin, A.M. Yacout, Improving stability of ALD ZrN thin film coatings over U-Mo dispersion fuel, Applied Surface Science (2020) 147378.

[94] L. Chen, Yttria-stabilized zirconia thermal barrier coatings—a review, Surface Review and Letters 13(05) (2006) 535-544.

[95] F. Yao, K. Ando, M.C. Chu, S. Sato, Static and cyclic fatigue behaviour of crack-healed Si_3N_4/SiC composite ceramics, Journal of the European Ceramic Society 21(7) (2001) 991-997.

[96] K. Takahashi, M. Yokouchi, S.-K. Lee, K. Ando, Crack-Healing Behavior of Al_2O_3 Toughened by SiC Whiskers, Journal of the American Ceramic Society 86(12) (2003) 2143-2147.

[97] M. Chu, S. Sato, Y. Kobayashi, K. Ando, Damage healing and strengthening behaviour in intelligent mullite/SiC ceramics, Fatigue & Fracture of Engineering Materials & Structures 18(9) (1995) 1019-1029.

[98] W. Sloof, S. Turteltaub, A. Carabat, Z. Derelioglu, S. Ponnusami, G. Song, 219 Crack healing in yttria stabilized zirconia thermal barrier coatings, Self Healing Materials: Pioneering Research in the Netherlands (2015) 219.

[99] M.E. Smith, Recent progress in solid-state NMR of low-γ nuclei, Annual Reports on NMR Spectroscopy, Academic Press2001, pp. 121-175.

[100] S.C. Singhal, Advances in solid oxide fuel cell technology, Solid State Ionics 135(1) (2000) 305-313.

[101] X. Fan, W. Huang, X. Zhou, B. Zou, Preparation and characterization of NiAl–TiC–TiB_2 intermetallic matrix composite coatings by atmospheric plasma spraying of SHS powders, Ceramics International (2020).

[102] A.H. Heuer, Oxygen and aluminum diffusion in α-Al_2O_3: How much do we really understand?, Journal of the European Ceramic Society 28(7) (2008) 1495-1507.

[103] Y. Oishi, W.D. Kingery, Self-Diffusion of Oxygen in Single Crystal and Polycrystalline Aluminum Oxide, The Journal of Chemical Physics 33(2) (1960) 480-486.

[104] M. MUNRO, Evaluated material properties for a sintered alpha-alumina, Journal of the American Ceramic Society 80(8) (1997) 1919-1928.

[105] S. Xie, C. Song, Z. Yu, S. Liu, F. Lapostolle, D. Klein, C. Deng, M. Liu, H. Liao, Effect of environmental pressure on the microstructure of YSZ thermal barrier coating via suspension plasma spraying, Journal of the European Ceramic Society (2020).

[106] Y. Heng, N. Feng, Y. Liang, D. Hu, Lignin-retaining porous bamboo-based reversible thermochromic phase change energy storage composite material, International Journal of Energy Research 44(7) (2020) 5441-5454.

[107] B. Mazères, C. Desgranges, C. Toffolon-Masclet, D. Monceau, Experimental study and numerical simulation of high temperature (1100–1250°C) oxidation of prior-oxidized zirconium alloy, Corrosion Science 103 (2016) 10-19.

[108] D. Seo, M. Sayar, K. Ogawa, SiO_2 and $MoSi_2$ formation on Inconel 625 surface via SiC coating deposited by cold spray, Surface and Coatings Technology 206(11-12) (2012) 2851-2858.

[109] Y. Xu, X. Liu, L. Gu, J. Wang, P. Schützendübe, Y. Huang, Y. Liu, Z. Wang, Natural oxidation of amorphous Cu_xZr_{1-x} alloys, Applied Surface Science 457 (2018) 396-402.

[110] K.R. Lim, W.T. Kim, E.-S. Lee, S.S. Jee, S.Y. Kim, D.H. Kim, A. Gebert, J. Eckert, Oxidation resistance of the supercooled liquid in $Cu_{50}Zr_{50}$ and $Cu_{46}Zr_{46}Al_8$ metallic glasses, Journal of Materials Research 27(8) (2012) 1178.

[111] B. Wang, D. Huang, N. Prud'Homme, Z. Chen, F. Jomard, T. Zhang, V. Ji, Diffusion mechanism of Zr-based metallic glass during oxidation under dry air, Intermetallics 28 (2012) 102-107.

[112] H. Over, A. Seitsonen, Oxidation of metal surfaces, Science 297(5589) (2002) 2003-2005.

[113] S. Aygün, S. Klinge, Continuum mechanical modeling of strain-induced crystallization in polymers, International Journal of Solids and Structures 196-197 (2020) 129-139.

[114] Y. Wang, D. Su, H. Ji, X. Li, Z. Zhao, H. Tang, Gradient structure high emissivity $MoSi_2$-SiO_2-SiOC coating for thermal protective application, Journal of Alloys and Compounds 703 (2017) 437-447.

[115] X. Jing, H.-Y. Mi, X.-F. Peng, L.-S. Turng, Biocompatible, self-healing, highly stretchable polyacrylic acid/reduced graphene oxide nanocomposite hydrogel sensors via mussel-inspired chemistry, Carbon 136 (2018) 63-72.

[116] T. Ouyang, S. Xiong, Y. Zhang, D. Liu, X. Fang, Y. Wang, S. Feng, T. Zhou, J. Suo, Cyclic oxidation behavior of SiC-containing self-healing TBC systems fabricated by APS, Journal of Alloys and Compounds 691 (2017) 811-821.

[117] T.N. Son Thanh Nguyen, Masatoshi Takeda, Nguyen Ngoc Hieu, Tsuyoshi Takahashi, Development of Yttrium Titanate/Nickel Nanocomposites with Self Crack-Healing Ability and Potential Application as Thermal Barrier Coating Material, (2020).

[118] I.I. Kurniadi Isnu, On the in situ encapsulation of MoSi2B healing particles in YSZ TBCs: Self-healing of thermal barrier coatings (TBCs), (2016).

[119] V. Carnicer Cervera, E. Cañas-Recacha, M.J. Orts Tarí, R. Moreno, M.D. Salvador Moya, P. Carpio Cobo, L. Navarro, E. Sánchez-Vilches, Characterization of thermal barriers coatings of Y-TZP/Al_2O_3/SiC composite obtained by suspension plasma spraying, (2017).

[120] B. Xiao, X. Huang, T. Robertson, Z. Tang, R. Kearsey, Sintering resistance of suspension plasma sprayed 7YSZ TBC under isothermal and cyclic oxidation, Journal of the European Ceramic Society 40(5) (2020) 2030-2041.

[121] F. Nozahic, A.L. Carabat, W. Mao, D. Monceau, C. Estournès, C. Kwakernaak, S. Van Der Zwaag, W.G. Sloof, Kinetics of zircon formation in yttria partially stabilized zirconia as a result of oxidation of embedded molybdenum disilicide, Acta Materialia 174 (2019) 206-216.

Journal of Composites and Compounds 2 (2020) 155-162

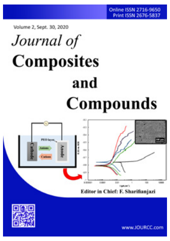

Available online at www.jourcc.com

Journal homepage: www.JOURCC.com

Journal of Composites and Compounds

Concrete filled FRP–PVC tubular columns used in the construction sector: A review

Milad Bazli[a]*, *Leila Bazli*[b], *Roozbeh Rahmani*[c], *Sohail Mansoor*[d], *Mohammad Ahmadi*[d], *Rasul Pouriamanesh*[e]

[a] *Department of Civil Engineering, Monash University, Clayton, Victoria, Australia*
[b] *School of Metallurgy and Materials Engineering, Iran University of Science and Technology, Tehran*
[c] *Department of civil engineering,Faculty of civil engineering, University of Tabriz, Tabriz, Iran*
[d] *Faculty of Engineering, Christian-Albrechts-University Kiel, Germany*
[e] *Mahshahr Pipe Mill Co. (MPM), Iran*

ABSTRACT

In recent years, fiber-reinforced polymer-polyvinyl chloride (FRP-PVC) tubular columns have been used increasingly in civil engineering applications. Concrete-filled RP-PVC tubes possess high durability, high strengthening performance, satisfactory bond strength, and compressive behavior. It has been observed that these cost-effective tubular columns are promising materials for enhancing strain capacities, strength, and stiffness of structures containing reinforced concrete (RC). These composite tubular columns are composed of FRP and PVC and are used for strengthening concrete. FRP enhances strength capacity while PVC improves the corrosion resistance of concrete piles in harsh environments. This review focuses on the properties of FRP-PVC tubular columns, their application in civil engineering, and the recent advancements in this field.

ARTICLE INFORMATION

Article history:
Received 18 August 2020
Received in revised form 3 September 2020
Accepted 26 September 2020

Keywords:
Reinforced concrete
FRP–PVC
Tubular columns
Strengthening
Durability

Table of contents

1. Introduction

Since its emergence in 1850, concrete has fulfilled various needs in construction technology. Concrete is extensively used in the construction of bridges, buildings, roads, dams, walls, etc. [1, 2]. It is known that in harsh environments, such as seawater and acidic areas, due to the high amount of chloride and chemical attacks, corrosion of traditional carbon steel reinforcement will be a serious issue if the concrete is reinforced with such reinforcement [3, 4]. Therefore, using corrosion-resistant materials, especially in coastal areas, such as FRP and PVC has been recently proposed to be used together with concrete to address the

---

* *Corresponding author: Milad Bazli; E-mail: milad.bazli@monash.edu*

https://doi.org/10.29252/jcc.2.3.7

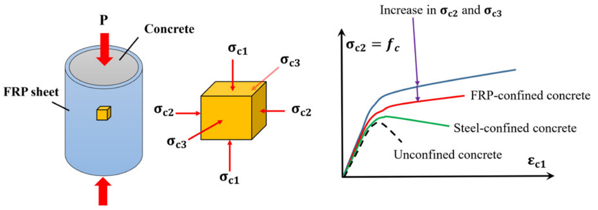

Fig. 1. Stress-strain relationship in concrete confined with FRP.

corrosion problem of traditional steel reinforcement [5-7].

It has been reported that the lateral active or passive confinement by a confining jacket can enhance the mechanical performance and durability of concrete structures [8, 9]. Different confining jackets in terms of forms and material have been widely investigated to strengthen/rehabilitate new constructions or existing structures [10-12]. These include steel spirals, steel stirrups, pre-stressing strands, hollow tubes/prisms, pre/post-tensioned FRP shells, FRP tubes, FRP composite stirrups, FRP rings, composite ropes, shape memory alloy wraps, and hybrid confining jackets (passive and active) [13-16].

Polymer and polymer composites are gaining increasing attention in various applications [9, 17-22]. This is due to the possibility to benefit from the combination of properties related to contributing constituents [23-28]. Due to high stiffness, full usage of materials and high strength composite columns have been increasingly used recently [29-31]. However, the durability of large sophisticated structures in special environments such as acidic environments and seawater conditions have attracted more attention. Numerous studies in the field of confined concrete columns using different materials showed that using composite material confinement could enhance the ultimate strength by 3 times and the ultimate strain by 15 times. Over the last decades, the replacement of steel bars with FRP rods has been shown to yield better corrosion resistance for structural concrete [5, 32-34].

There are many applications, in which FRP composites can be used in construction and specifically in corrosive environments. Concrete-filled FRP tubes can be used as drilling platforms, bridge, piers, etc. [35-37]. In this regard, many studies have focused on concrete-filled FRP tubes, and mainly on their short-term mechanical properties [38-54].

As a result of stable service performance, low price, and high production volume, PVC has also been used as concrete molds or pipes in the construction industry [55-57]. PVC materials exhibit some advantages such a low creep deformation, low diffusion for humidity, high electrical insulation, large ultimate strain, excellent corrosion resistance and durability, smooth surface, good mechanical stability, great consistency with other materials such as water, acids, and concrete, and easy machining, gluing, and cutting for fabrication versatility [58-60]. Therefore, FRP-PVC composite members offer both corrosion resistance of PVC and high strength capacity of FRP and they are promising materials for the application in special environments [5, 61-63].

Table 1.
Common characteristics of FRP materials

Material	Fiber strength (MPa)	Laminate density (g/cc)	Laminated Strength (MPa)	Young's modulus (GPa)	Strength to weight ratio
Epoxy	-	1-1.15	12-40	3	28
CFRP	4127	1.9-2.1	1600	125-181	1013
BFRP	3792	2.6-2.8	1100	70-90	1000
GFRP	3450	2.4-2.5	1500	30-40	564
AFRP (Kevlar)	2757	1.44	1430	70.5-112.4	993

Due to the properties of FRP–PVC composites such as high durability and strength, they are expected to have a reinforcing effect on concrete. Therefore, this paper aims to review the studies on FRP–PVC composites as tubular columns and their potential application in concrete structures.

2. Mechanism of concrete confinement

The ultimate compressive strength of a concrete element is remarkably enhanced in the third direction when it is confined in two mutually perpendicular directions. Generally, lateral confinement to concrete is provided by passive confinement or active confinement, e.g. hydraulic pressure. Passive confinement, such as steel stirrups, cause compressive stresses in the element by the imposed elongation on steel stirrups generated by the expansion of concrete. Nevertheless, the element is provided with constant confinement and thereby active confinement after yielding of the steel stirrups. FRP has attracted attention in various structural applications due to its promising properties. Some characteristics of FRP materials are listed in Table 1. For concrete confined with FRP, while the concrete lateral expansion increases, the inward radial pressure is enhanced because of the linear elastic behavior of FRP until failure. Therefore, it is not valid to assume that the presence of a constant confining pressure, and FRP jackets are considered as passive confinement to columns [64].

Moreover, the outer FRP jackets in the form of additional closed hoops effectively improve the shear strength of substandard columns. This enhancement is the result of extra shear reinforcement provided in the jackets. Considering the flexural performance, the concrete columns confined with FRP are provided with the lateral expansion prevention of the core concrete and the longitudinal reinforcement support when axial compressive loading or both lateral and axial compressive loadings are applied on the concrete columns. As a result, compression concrete can bear higher strains before failure, as shown in Fig. 1. Additionally, the concrete compression strength is enhanced by concrete confinement resulting in the improvement of post-cracking behavior i.e. the enhancement of the flexural strength. The application of the external FRP jacket can also enhance the short lap-splice reinforcement behavior. This is caused by the bond stress increase along the splice to delay the splitting onset and alleviate the subsequent deterioration severity and improve the lap-splice performance of defective columns [64]. Richart et al. [65] suggested a simple equation for the determination of hydrostatic fluid pressure-confined concrete (active confinement) as follows:

$$f'_{cc} = f'_{co} + k_1 . f_{lu} \qquad (1)$$

where f'_{cc} denotes the confined concrete ultimate strength and f'_{co} represents the compressive strength of unconfined concrete under f_{lu} (maximum lateral pressure).

3. Concrete-filled FRP tubes

Owing to excellent anti-corrosion behavior, high durability, as well as high strength-to-weight ratio, FRP has been increasingly utilized in the field of civil engineering [32, 67-72]. FRP-strengthened concrete piles and columns are able to decrease the cost remarkably compared to concrete piles and columns reinforced by steel, particularly in harsh marine environments [36, 73-76]. It has been reported that the USA spends more than $1 billion every year for maintaining waterfront piling systems and about $2 billion for the replacement and repairing reinforced concrete piers because of the corrosion of steel reinforcement. The replacement of steel with FRP is regarded as a promising approach for overcoming this problem [8, 77, 78].

FRP grids, FRP helixes, FRP stirrups, FRP rings, and FRP tubes are different forms of FRP lateral confinement for strengthening the concrete columns. Additionally, it has been proven that the externally bonded FRP systems can effectively strengthen the concrete girders or beams. Furthermore, owing to the higher anticorrosion ability and durability of FRP materials, confining with these materials is superior to steel materials for piles in marine environments [79-82].

Concrete filled tubular (CFT) columns, especially the so-called tubed concrete columns are mainly used in construction industries. In these columns, steel bars act as longitudinal reinforcement for the core concrete, and the tube is used for transverse reinforcement. There exists a gap at the end of the tube column to suppress the axial stress transfer into the tube. In typical CFT columns, the tubes are mainly utilized as both longitudinal and transverse reinforcements to bear bending moment and axial forces. The “tubed column” concept was primarily presented by Tomii et al. [83, 84]. They showed the capabilities of steel tube concrete columns by experiments. The definition concept of FRP-tubed and steel-tubed columns concrete is the same. Similar to the results of steel-tubed columns, the excellent properties of FRP-tubed columns have been demonstrated in some studies [85, 86].

4. Mechanical properties of Concrete-filled FRP tubes

4.1. Compressive strength

Ozbakkaloglu et al. [87] studied the axial compressive property of 83 monotonically-loaded high-strength circular concrete-filled FRP tubes (CFFTs) experimentally. The height-to-diameter ratio of the samples was 2. The parameters affecting the compressive behavior of CFFTs including manufacturing method, concrete strength, fiber type, and specimen size were also investigated. According to the results, the compressive behavior of CFFTs was not noticeably affected by the specimen size. The confinement strength ratio (f'_{cc}/f'_{co}) was obtained in the range of 1.01-2.44. In addition, the strength enhancement ratio (f'_{cc}/f'_{co}) decreased at a specific nominal confinement ratio (f'_{lu}/f'_{co}) owing to an increment in concrete compressive strength (f'_{co}). Li et al. [88] reported the ratio of the confined concrete strength to unconfined concrete strength (f_{cc}/f_c) of sea sand and seawater concrete (SWSSC)-filled carbon/glass / basalt-FRP (CFRP/GFRP/BFRP) tubes in the range of 2.08 to 6.86.

4.2. Ductility

Ozbakkaloglu et al. [87] found a correlation between the ultimate axial strain (ε_{cu}) of CFFTs and the ultimate tensile strain (ε_{fu}) of the fibers. The strain enhancement ratio ($\varepsilon_{cu}/\varepsilon_{co}$) was obtained in the range of 1.34 to 15.31 depending on the manufacturing method, specimen size, concrete strength, and fiber type. They explained that highly ductile behavior was obtained by sufficiently confined high-strength CFFTs. It can be deduced that the level of confinement significantly influences the behavior of the CFFTs, and after the initial peak of strengths, the load-carrying capacity may not be preserved in lightly confined CFFTs.

4.3. Durability

The durability is defined as the ability to resist a specific loading or environmental condition for a specific time under a suitable load and environmental condition [89]. Li et al. [88] studied the durability of SWSSC-filled GFRP/CFRP/BFRP tubes during six months by exposing the specimens to artificial seawater containing 3.5% salt solution at the temperature of 40 ˚C. Based on the results, the SWSSC compressive strength showed no changes after exposure to seawater, however, in BFRP and GFRP, an evident hoop strength degradation was exhibited. Mechanical properties of SWSSC-filled FRP tubes, such as ultimate axial strain and strength decreased as a result of environmental aging and the hoop strength deterioration of FRP was considered as the major mechanism. The ratio of f_{cc}/f_c was obtained for exposed and unexposed samples and exposed-to-unexposed ratios of f_{cc}/f_c ranged from 0.47 to 0.77.

5. Concrete-filled PVC tubes

The aims of using PVC tubes in concrete columns are the improvement of the deformation capacity of concrete and accommodation of the electrical wiring, wastewater, and rain. Kurt [90] experimentally and theoretically studied commercial PVC tubes filled with a concrete core. The results exhibited that the PVC tubes enhanced the concrete core strength to approximately 3.2 times the pipe burst pressure. The encasement holds the circular shape of the flexible tube and also supports most of the external loads [8]. It can be mentioned that tube ring compression stress should be below the yield strength. PVC inner-steel outer tubes as well as double-skin tubes filled with concrete were analyzed under axial load. As the results demonstrated, under moderate load conditions, the PVC tube can be considered as a good alternative material for steel one [91]. Xue et al. [92] investigated seismic performance as well as the deformation capacity of PVC tube-filled high-strength concrete short columns (PVC-RHC) under quasi-static loadings and test variables including shear span ratio, axial compression ratio, and PVC tube diameter. The ductility factor between 3.35 and 4.61 was obtained for PVC-RHC columns, in comparison with 1.94 for RHC. With an increase in the diameter/height ratio of PVC tube, ultimate capacity, and ductility increase.

6. Mechanical properties of concrete-filled PVC tubes

6.1. Compressive strength

The concrete confinement with PVC tubes improves the damage characteristics and the bearing capacity of the concrete core. According to Xue et al. [92], the average of confinement strength ratios for concrete-filled PVC tubes with an h/D ratio of 2 was obtained in the range of 1.0-3.04 [8, 93]. Different parameters contribute to the variation of the two values such as testing conditions, concrete infill strength, PVC tube geometry, and the size of specimens. Furthermore, the analyses showed that at the D/t ratio in the range of 20–35, optimum f_{cc}/f_{uc} values were obtained.

6.2. Ductility

The PVC tube is described through a combination of two contradictions; a ductile plastic or a type of rigid elastic material. Some studies showed that the variation of the confined to the unconfined strain ratio was between 1.415 and 5.54 for concrete-filled PVC tubes with the *h/D* ratio of 2 (Table 2). In addition, the range of 2000-3945 kJ/m3 was reported for the energy absorption capacity [94, 95]. Generally, PVC tubular specimens with low wall thicknesses showed the improvement of the deformation capacity and energy dissipating of concrete columns and as the thickness of PVC tube increases, ductility improvement is obtained [92, 94].

6.3. Durability

Commercially available thermoplastic pipes, like PVC pipes, have shown the ability to enhance the durability of reinforced concrete (RC) structures [90, 94, 96, 97]. No deterioration was observed in PVC pipes

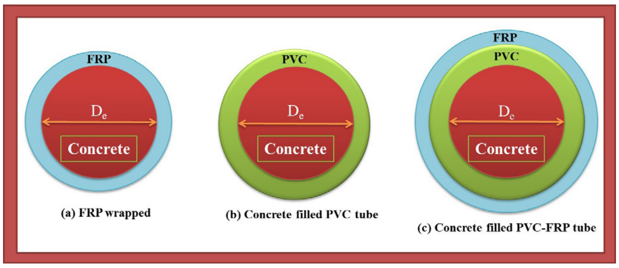

Fig. 2. Concrete pile confined with a) FRP wrap, b) PVC tube, and c) PVC-FRP composite tube.

buried in the soil after 60 years and they showed extended life of 50 years [98]. The thermal conductivity of PVC is around 0.45~0.6% of steel tubes providing a stable condition for core concrete curing, which leads to high durability together with high performance [97]. A study by Gupta et al. [99] indicated that there is no strength degradation ductility for RC-filled PVC specimens exposed to harsh environments. Based on the test results, no significant changes in the chemical composition and microstructure of the PVC jackets were observed after 6 months for RC-filled-PVC tubes immersed in saturated seawater. The improvement of PVC durability provides a system with potential applications for many different structures that are exposed to saline and marine environmental conditions.

A study on natural aging and accelerated aging of PVC by Jakubowicz et al. [100] revealed no evident changes in elongation at fracture and mechanical properties of PVC material after eight weeks of aging in the air at 80˚C. Due to the PVC great anti-corrosion behavior, FRP jackets can compensate the relatively poor confining effect of PVC tubes and provide significant durability and mechanical strength for the confined concrete-filled PVC tubes.

7. FRP–PVC confinement

There are many research works on applying plastic pipes such as PVC to overcome the relative low ultimate strain and ductility of FPR [102]. It is a widely used polymer in various products including medical devices, pipes, flooring, and profiles for windows and doors. As a result of excellent physical, mechanical, and chemical properties, PVC is considered a “natural” fire-resistant material [103]. A hybrid column system for new constructions is proposed by Toutanji et al. [104], in which PVC tubes are filled with concrete and the external confinement is provided by continuous impregnated FRP hoops that may have various spacing. It has been proposed that FRP-PVC tubes are effective confinements for improving both failure strains and the strength of concrete. Fakharifar et al. [8] studied the mechanical behavior of concrete confined with PVC, FRP, and FRP-PVC. The FRP-PVC confined concrete indicated higher ultimate strain and strength compared to the FRP and PVC ones [77].

Table 2.
Confinement ratio (f_{cc}/f_{uc}) and ductility of concrete-filled PVC tubes

Ref.	h/D (mm)	f_{cc}/f_{uc}	$\varepsilon_{cu}/\varepsilon_{uc}$	t (mm)
Kurt [90]	2	1.718	-	6.4
Wang and Yang [94]	2	1.011-2.345	1.415-5.540	3.7-8.5
Saadoon [101]	2	1.118-1.688	1.686-2.473	3.2-5.3
Fakharifar and Chen [8]	1.8	0.966-1.050	1.81-4.07	7.1
Oyawa et al. [93]	2	1.180-3.040	-	2.5-3.0

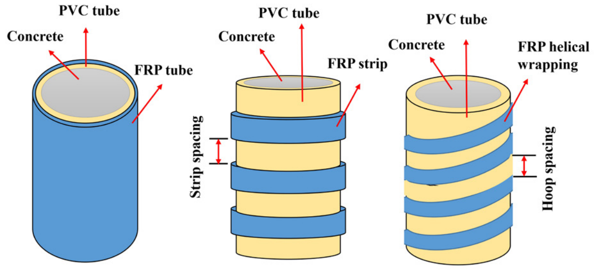

Fig. 3. Schematic of the placement of FRP-PVC tube

The FRP-PVC-confined concrete system is shown in Fig. 2 and different FRP-PVC-confined concrete systems are shown in Fig. 3.

8. Mechanical properties of concrete-filled FRP-PVC tubes

8.1. Compressive strength

There are numerous studies conducted regarding the compressive properties of FRP-PVC tubular columns. Several parameters, including the concrete characteristics and FRP-PVC properties, were investigated [8, 56, 58-62, 104-114]. In a study by Toutanji and Saafi [96], it was reported that the strength of PVC–FRP confined concrete (with h/D of 3) was high. The FRP-PVC tubes provided lateral confinement and created triaxial stress in the concrete, which constrained concrete during dilation and consequently, enhanced its capacity of load bearing. The compressive strength enhancement ratio ($(f_{cu}-f_{co})/f_{co}$) was reported to range from 0 to 1.9 depending on the fiber type and hoop spacing. In a study by Mammen and Antony [109], concrete-filled PVC tubes (h/D=2.1) with various thicknesses were wrapped with GFRP and CFRP. They confined concrete with two different patterns of circular and helical wrapping with two different hoop spacing in a way to decrease the amount of required FRP. Higher-strength was achieved for carbon fiber circular wrapping and larger PVC thickness (ultimate strength of 33.5 MPa).

Fakharifar et al. [115] provided confinement using a PVC tube (with h/D of 2) and FRP wrappings or FRP containing a layer of foam to reduce impact energy resulting from the potential rupture of FRP and fracture of PVC. The results showed that the contribution of the PVC tube to the axial strength of concrete was insignificant, however, the strength of the columns enhanced more significantly when FRP wraps in which fibers oriented in hoop direction were used. The strength enhancement ratios (f_{cu}/f_{co}) were obtained between 1.08 and 2.29 for the samples.

The improvement of the ductility as well as the strength of FRP-PVC tube-confined recycled aggregate concrete was studied by Gao et al. [58]. As the results demonstrated, the compressive strength enhancement of the samples confined with the FRP-PVC hybrid system ranged from 4.5% to 39.6%. Moreover, a thicker FRP tube or strip led to a higher improvement in deformation and strength.

8.2. Ductility

Toutanji and Saafi [96] also reported the ductility enhancement of PVC–FRP confined concrete. The ductility increase ($(\varepsilon_{cu}-\varepsilon_{co})/\varepsilon_{co}$) for the samples with different fiber types and hoop spacing was between 0-9. In the research by Fakharifar et al. [115], it was stated that the addition of FRP wraps with hoop-directed fibers around PVC tubes increased the ductility of the columns significantly. The strain enhancement ratios

Table 3.

Confinement ratio (f_{cc}/f_{uc}) and ductility of concrete-filled FRP-PVC tubes

Ref.	h/D (mm)	f_{cc}/f_{uc}	$\varepsilon_{cu}/\varepsilon_{uc}$
Fakharifar [8]	2	1.08-2.29	2.14-12.21
Gao [58]	2	0.2-1.13	3.95-14.2
Toutanji [111]	3	1.31-2.81	1.55-9

$(\varepsilon_{cu}/\varepsilon_{co})$ of the specimens were obtained from 2.14 to 12.21. After the rupture of the FRP wraps, the interior PVC tube fractured immediately leading to an instant drop in load-carrying capacity. The authors proposed that by placing a layer of foam between the FRP wraps and PVC tube as an energy absorber, this brittle failure mode could be avoided. The use of this layer causes a gradual reduction of the strength in steps. Therefore, the foam layer proved to have a significant effect on the reduction of brittleness providing a relatively ductile response upon the rupture of FRP.

Yu et al. [116] reported that by an increase in the ratio of shear span or axial compression, elastic-plastic displacement angles and the displacement ductility coefficient of RC columns confined with CFRP-PVC under low cyclic loading were reduced gradually. Furthermore, the angles of elastic-plastic displacement together with the displacement ductility coefficient of the samples were gradually enhanced by the decrease in the hoop spacing of FRP strips. Fang et al. [107] conducted an experimental investigation on the concrete stub columns confined with CFRP-PVC under the axial compression condition. They investigated the influence of CFRP strip spacing on the mechanical properties of the confined stub columns. The obtained values of $\varepsilon_{cu}/\varepsilon_{co}$ were reported to be between 6.3 and 9.1, indicating the provision of significant confinement on core concrete by the CFRP-PVC tubes. Apparently, by an increase in the spacing of CFRP strips, this ratio is gradually reduced. The mechanical properties of concrete-filled FRP-PVC tubes are summarized in Table 3.

8.3. Durability

Despite the outstanding characteristics of FRP/PVC composites, their durability under harsh environmental conditions is still a serious concern [117]. There are numerous studies available on the short-term and long-term durability of different FRP/PVC composites as the main element and reinforcing members under various environmental conditions [95, 118-122]. In this regard, previous studies conducted on the durability of the mechanical properties of FRP composites under alkaline environment (i.e. when using FRP/PVC with concrete), have shown that such condition is detrimental to some types of FRP/PVC composites [119]. Therefore, the durability of composite-reinforced concrete structures in harsh environmental conditions (e.g. alkaline, acidic, and marine environments as well as elevated temperatures) has always been a major concern [33, 96, 118, 123-128]. The U.S. allocates more than $1 billion annually for repairing and replacing waterfront piling systems [8].

Toutanji and Saafi [96] fabricated composite columns composed of a hybrid FRP-PVC tube with a concrete core and studied the performance of these concrete columns in various environmental conditions including ambient temperature, wet and dry, as well as freezing and thawing conditions. According to the durability results, confining concrete with CFRP-PVC composite resulted in good performance under the severe exposures, however, a decrease in both ductility and strength was observed in the AFRP-PVC (aramid FRP) and concrete filled-GFRP-PVC samples. Upon 400 freezing/thawing cycles, AFRP-PVC specimens exhibited around l0% strength reduction while l0% reduction was observed for the AFRP-PVC specimens.

In another study by Toutanji et al. [129], the durability performance of concrete filled-FRP-PVC under freezing/thawing and wet/dry conditions was studied. According to the results, there was an insignificant influence on ductility as well as the strength of all samples. No reduction of strength was observed after wet/dry cycles (200 and 400 cycles) in PVC-CFRP confined concrete. However, due to the reduction of axial strain after 400 wet/dry cycles, the ductility of the samples decreased. GFRP-PVC and AFRP-PVC confined concrete underwent the reduction of axial strain and the strength only after wet/dry cycles of 400. Additionally, a noticeable decrement in the axial strain of the AFRP-PVC and GFRP-PVC confined samples occurred after 400 cycles of freezing/thawing. Generally, the CFRP-PVC concrete specimens showed lower strain reduction compared to other samples.

9. Conclusions and future insights

In recent decades, researchers have focused on using new materials to confine concrete members laterally for construction applications. The improvement of the existing knowledge along with the exploration of other beneficial and inexpensive alternatives to confining concrete members will provide a viable solution for sustainable construction. This article deals with an overview of the application of FRP–PVC tubular columns strengthening method for concrete structure reinforcement. According to previous investigations, concrete columns confined with FRP–PVC render excellent ductility, high bearing capacity, timesaving convenient construction, and outstanding applicability in normal conditions together with aggressive environments, good durability characteristics, as well as being lightweight. This system is suitable for harsh environments and offshore marine structures due to the corrosion resistance of PVC. However, further laboratory studies, field investigations, as well as detailed information from experimental and analytical investigations are needed to develop proper design guidelines. By applying the established measures, introducing practical composite-based systems in civil construction works will be facilitated.

REFERENCES

[1] S. Hemavathi, A. Sumil Kumaran, R. Sindhu, An experimental investigation on properties of concrete by using silica fume and glass fibre as admixture, Materials Today: Proceedings 21 (2020) 456-459.

[2] M. Gunavel, S. Aishwarya, K. Indhumathi, N. Jalapriya, M.K. Priya, Proportioning of Lightweight Concrete by the Inclusion of Expanded Polystyrene (EPS), International Journal of Engineering Research & Technology 9(2) (2020).

[3] L. Wang, Z. Yang, Y. Cui, B. Wei, S. Xu, J. Sheng, M. Wang, Y. Zhu, W. Fei, Graphene-copper composite with micro-layered grains and ultrahigh strength, Scientific Reports 7(1) (2017) 41896.

[4] M. Bazli, X.-L. Zhao, R.S. Raman, Y. Bai, S. Al-Saadi, Bond performance between FRP tubes and seawater sea sand concrete after exposure to seawater condition, Construction and Building Materials 265 (2020) 120342.

[5] S.-F. Jiang, S.-L. Ma, Z.-Q. Wu, Experimental study and theoretical analysis on slender concrete-filled CFRP–PVC tubular columns, Construction and Building Materials 53 (2014) 475-487.

[6] J. Teng, T. Yu, J. Dai, G. Chen, FRP composites in new construction: current status and opportunities, Proceedings of 7th National Conference on FRP Composites in Infrastructure (Supplementary Issue of Industrial Construction), keynote presentation, Hangzhou, China, 2011.

[7] M. Bazli, X.-L. Zhao, A. Jafari, H. Ashrafi, Y. Bai, R.S. Raman, H. Khezrzadeh, Mechanical properties of pultruded GFRP profiles under seawater sea sand concrete environment coupled with UV radiation and moisture, Construction and Building Materials (2020) 120369.

[8] M. Fakharifar, G. Chen, Compressive behavior of FRP-confined concrete-filled PVC tubular columns, Composite Structures 141 (2016) 91-109.

[9] S. Saadi, B. Nazari, Recent developments and applications of nanocomposites in solar cells: a review, Journal of Composites and Compounds 1(1) (2019) 48-58.

[10] Z. Yan, C.P. Pantelides, L.D. Reaveley, Posttensioned FRP composite shells for concrete confinement, Journal of Composites for Construction 11(1) (2007) 81-90.

[11] K.N. Nesheli, K. Meguro, Seismic retrofitting of earthquake-damaged concrete columns by lateral pre-tensioning of FRP belts, Proc., 8th US National Conf.

on Earthquake Engineering, Earthquake Engineering Research Institute (EERI) El Cerrito, CA, 2006.

[12] B. Wang, E.V. Bachtiar, L. Yan, B. Kasal, V. Fiore, Flax, Basalt, E-Glass FRP and Their Hybrid FRP Strengthened Wood Beams: An Experimental Study, Polymers 11(8) (2019) 1255.

[13] T.C. Rousakis, I.S. Tourtouras, RC columns of square section–passive and active confinement with composite ropes, Composites Part B: Engineering 58 (2014) 573-581.

[14] M. Shin, B. Andrawes, Experimental investigation of actively confined concrete using shape memory alloys, Engineering Structures 32(3) (2010) 656-664.

[15] E. Choi, B.-S. Cho, S. Lee, Seismic retrofit of circular RC columns through using tensioned GFRP wires winding, Composites Part B: Engineering 83 (2015) 216-225.

[16] A.U. Al-saadi, T. Aravinthan, W. Lokuge, Structural applications of fibre reinforced polymer (FRP) composite tubes: A review of columns members, Composite Structures 204 (2018) 513-524.

[17] M. Arefian, M. Hojjati, I. Tajzad, A. Mokhtarzade, M. Mazhar, A. Jamavari, A review of Polyvinyl alcohol/Carboxiy methyl cellulose (PVA/CMC) composites for various applications, Journal of Composites and Compounds 2(3) (2020) 69-76.

[18] A. Abuchenari, K. Hardani, S. Abazari, F. Naghdi, M.A. Keleshteri, A. Jamavari, A.M. Chahardehi, Clay-reinforced nanocomposites for the slow release of chemical fertilizers and water retention, Journal of Composites and Compounds 2(3) (2020) 85-91.

[19] S.O. Omid, Z. Goudarzi, L.M. Kangarshahi, A. Mokhtarzade, F. Bahrami, Self-expanding stents based on shape memory alloys and shape memory polymers, Journal of Composites and Compounds 2(3) (2020) 92-98.

[20] H.W. Jang, A. Zareidoost, M. Moradi, A. Abuchenari, A. Bakhtiari, R. Pouriamanesh, B. Malekpouri, A.J. Rad, D. Rahban, Photosensitive nanocomposites: environmental and biological applications, Journal of Composites and Compounds 2(1) (2020) 50-60.

[21] A. Kazemzadeh, H. Kazemzadeh, Determination of Hg^{2+} by Diphenylcarbazone Compound in Polymer Film, Journal of Composites and Compounds 1(1) (2019) 30-35.

[22] L. Bazli, M.H. Bagherian, M. Karrabi, F. Abbassi-Sourki, H. Azizi, Effect of starch ratio and compatibilization on the viscoelastic behavior of POE/starch blends, Journal of Applied Polymer Science 137(29) (2020) 48877.

[23] P. Abasian, M. Radmansouri, M.H. Jouybari, M.V. Ghasemi, A. Mohammadi, M. Irani, F.S. Jazi, Incorporation of magnetic NaX zeolite/DOX into the PLA/chitosan nanofibers for sustained release of doxorubicin against carcinoma cells death in vitro, International journal of biological macromolecules 121 (2019) 398-406.

[24] M. Radmansouri, E. Bahmani, E. Sarikhani, K. Rahmani, F. Sharifianjazi, M. Irani, Doxorubicin hydrochloride-Loaded electrospun chitosan/cobalt ferrite/titanium oxide nanofibers for hyperthermic tumor cell treatment and controlled drug release, International journal of biological macromolecules 116 (2018) 378-384.

[25] B.F. Dizaji, M.H. Azerbaijan, N. Sheisi, P. Goleij, T. Mirmajidi, F. Chogan, M. Irani, F. Sharafian, Synthesis of PLGA/chitosan/zeolites and PLGA/chitosan/metal organic frameworks nanofibers for targeted delivery of Paclitaxel toward prostate cancer cells death, International Journal of Biological Macromolecules (2020).

[26] L. Bazli, A. Khavandi, M.A. Boutorabi, M. Karrabi, Morphology and viscoelastic behavior of silicone rubber/EPDM/Cloisite 15A nanocomposites based on Maxwell model, Iranian Polymer Journal 25(11) (2016) 907-918.

[27] L. Bazli, A. Khavandi, M.A. Boutorabi, M. Karrabi, Correlation between viscoelastic behavior and morphology of nanocomposites based on SR/EPDM blends compatibilized by maleic anhydride, Polymer 113 (2017) 156-166.

[28] A. Kazemzadeh, M.A. Meshkat, H. Kazemzadeh, M. Moradi, R. Bahrami, R. Pouriamanesh, Preparation of graphene nanolayers through surfactant-assisted pure shear milling method, Journal of Composites and Compounds 1(1) (2019) 25-30.

[29] M. Bazli, X.-L. Zhao, A. Jafari, H. Ashrafi, R.S. Raman, Y. Bai, H. Khezrzadeh, Durability of glass-fibre-reinforced polymer composites under seawater and sea-sand concrete coupled with harsh outdoor environments, Advances in Structural Engineering (2020) 1369433220947897.

[30] Z. Huang, D. Li, B. Uy, H.-T. Thai, C. Hou, Local and post-local buckling of fabricated high-strength steel and composite columns, Journal of Constructional Steel Research 154 (2019) 235-249.

[31] D. Li, Z. Huang, B. Uy, H.-T. Thai, C. Hou, Slenderness limits for fabricated S960 ultra-high-strength steel and composite columns, Journal of Constructional Steel Research 159 (2019) 109-121.

[32] H. Ashrafi, M. Bazli, A.V. Oskouei, Enhancement of bond characteristics of ribbed-surface GFRP bars with concrete by using carbon fiber mat anchorage, Construction and Building Materials 134 (2017) 507-519.

[33] M. Bazli, H. Ashrafi, A.V. Oskouei, Experiments and probabilistic models of bond strength between GFRP bar and different types of concrete under aggressive environments, Construction and Building Materials 148 (2017) 429-443.

[34] M. Bazli, Y.L. Li, X.L. Zhao, R.S. Raman, Y. Bai, S. Al-Saadi, A. Haque, Durability of seawater and sea sand concrete filled filament wound FRP tubes under seawater environments, Composites Part B: Engineering (2020) 108409.

[35] J. Wang, P. Feng, T. Hao, Q. Yue, Axial compressive behavior of seawater coral aggregate concrete-filled FRP tubes, Construction and Building Materials 147 (2017) 272-285.

[36] M. Bazli, X.-L. Zhao, Y. Bai, R.S. Raman, S. Al-Saadi, A. Haque, Durability of pultruded GFRP tubes subjected to seawater sea sand concrete and seawater environments, Construction and Building Materials 245 (2020) 118399.

[37] M. Bazli, X.-L. Zhao, Y. Bai, R.S. Raman, S. Al-Saadi, Bond-slip behaviour between FRP tubes and seawater sea sand concrete, Engineering Structures 197 (2019) 109421.

[38] Y.L. Li, X.L. Zhao, R.K. Raman Singh , S. Al-Saadi, Tests on seawater and sea sand concrete-filled CFRP, BFRP and stainless steel tubular stub columns, Thin-Walled Structures 108 (2016) 163-184.

[39] Y.L. Li, X.L. Zhao, R.K. Raman Singh , S. Al-Saadi, Experimental study on seawater and sea sand concrete filled GFRP and stainless steel tubular stub columns, Thin-Walled Structures 106 (2016) 390-406.

[40] G.M. Chen, Z.B. He, T. Jiang, J.F. Chen, J.G. Teng, Axial compression tests on FRP-confined seawater/sea-sand concrete, 6th Asia-Pacific Conference on FRP in Structures, 2017.

[41] Y.L. Li, J.G. Teng, X.L. Zhao, R.K. Singh Raman, Theoretical model for seawater and sea sand concrete-filled circular FRP tubular stub columns under axial compression, Engineering Structures 160 (2018) 71-84.

[42] C. Lu, A. Fam, The effect of tube damage on flexural strength of±55° angle-ply concrete-filled FRP tubes, Construction and Building Materials 240 (2020) 117948.

[43] H. Tian, Z. Zhou, Y. Wei, J. Lu, Behavior and Modeling of Ultra-High Performance Concrete-Filled FRP Tubes Under Cyclic Axial Compression, Journal of Composites for Construction 24(5) (2020) 04020045.

[44] A.M. Ali, R. Masmoudi, Composite Action Assessment of Concrete-Filled FRP Tubes Subjected to Flexural Cyclic Load, Engineering Structures 203 (2020) 109889.

[45] H. Lee, H. Jang, W. Chung, Effect of Recycled Concrete on the Flexural Behavior of Concrete-Filled FRP Tubes, International Journal of Concrete Structures and Materials 13(1) (2019) 12.

[46] A.F. Pour, A. Gholampour, J. Zheng, T. Ozbakkaloglu, Behavior of FRP-confined high-strength concrete under eccentric compression: tests on concrete-filled FRP tube columns, Composite Structures 220 (2019) 261-272.

[47] Z. Chen, J. Wang, J. Chen, H. GangaRao, R. Liang, W. Liu, Responses of concrete-filled FRP tubular and concrete-filled FRP-steel double skin tubular columns under horizontal impact, Thin-Walled Structures 155 (2020) 106941.

[48] H. Tian, Z. Zhou, Y. Wei, Y. Wang, J. Lu, Experimental investigation on axial compressive behavior of ultra-high performance concrete (UHPC) filled glass FRP tubes, Construction and Building Materials 225 (2019) 678-691.

[49] Y. Zhang, Y. Wei, J. Bai, Y. Zhang, Stress-strain model of an FRP-confined concrete filled steel tube under axial compression, Thin-Walled Structures 142 (2019) 149-159.

[50] Y.-L. Li, X.-L. Zhao, R.S. Raman, Behaviour of seawater and sea sand concrete filled FRP square hollow sections, Thin-Walled Structures 148 (2020) 106596.

[51] A.M. Ali, R. Masmoudi, Experimental and analytical investigation of new concrete filled FRP tube beam-column connections, Engineering Structures 191 (2019) 311-322.

[52] Y. Zhang, Y. Wei, J. Bai, G. Wu, Z. Dong, A novel seawater and sea sand concrete filled FRP-carbon steel composite tube column: Concept and behaviour, Composite Structures (2020) 112421.

[53] P. Xie, G. Lin, J. Teng, T. Jiang, Modelling of concrete-filled filament-wound FRP confining tubes considering nonlinear biaxial tube behavior, Engineering Structures 218 (2020) 110762.

[54] M.J. Abyaneh, H. El Naggar, P. Sadeghian, Numerical Modeling of the Lateral Behavior of Concrete-Filled FRP Tube Piles in Sand, International Journal of Geomechanics 20(8) (2020) 04020108.

[55] K. Gonnade, R. Khapre, Experimental and Computational Study on Concrete Filled PVC Plastic Tubes Placed In Columns, Helix 10(01) (2020) 165-169.

[56] S.M. Askari, A. Khaloo, M.H. Borhani, M.S.T. Masoule, Performance of polypropylene fiber reinforced concrete-filled UPVC tube columns under axial compression, Construction and Building Materials 231 (2020) 117049.

[57] Ö.B. Ceran, B. Şimşek, T. Uygunoğlu, O.N. Şara, PVC concrete composites:

comparative study with other polymer concrete in terms of mechanical, thermal and electrical properties, Journal of Material Cycles and Waste Management 21(4) (2019) 818-828.

[58] C. Gao, L. Huang, L. Yan, R. Jin, B. Kasal, Strength and ductility improvement of recycled aggregate concrete by polyester FRP-PVC tube confinement, Composites Part B: Engineering 162 (2019) 178-197.

[59] F. Yu, D. Li, D. Niu, D. Zhu, Z. Kong, N. Zhang, Y. Fang, A model for ultimate bearing capacity of PVC-CFRP confined concrete column with reinforced concrete beam joint under axial compression, Construction and Building Materials 214 (2019) 668-676.

[60] F. Yu, Z. Song, I. Mansouri, J. Liu, Y. Fang, Experimental study and finite element analysis of PVC-CFRP confined concrete column–Ring beam joint subjected to eccentric compression, Construction and Building Materials 254 (2020) 119081.

[61] H. Zhang, M.N. Hadi, Geogrid-confined pervious geopolymer concrete piles with FRP-PVC-confined concrete core: Analytical models, Structures, Elsevier, 2020, pp. 731-738.

[62] F. Yu, N. Zhang, Y. Fang, J. Liu, G. Xiang, Stress-strain model of weak PVC-FRP confined concrete column and strong RC ring beam joint under eccentric compression, Steel and Composite Structures 35(1) (2020) 13-27.

[63] Y.-C. Guo, S.-H. Xiao, S.-W. Shi, J.-J. Zeng, W.-Q. Wang, H.-C. Zhao, Axial Compressive Behavior of Concrete-Filled FRP-Steel Wire Reinforced Thermoplastics Pipe Hybrid Columns, Composite Structures (2020) 112237.

[64] Z. Wu, Y. Wu, M.F.M. Fahmy, 6 - FRP strengthening of concrete columns, in: Z. Wu, Y. Wu, M.F.M. Fahmy (Eds.), Structures Strengthened with Bonded Composites, Woodhead Publishing2020, pp. 387-480.

[65] F.E. Richart, A. Brandtzæg, R.L. Brown, A study of the failure of concrete under combined compressive stresses, University of Illinois at Urbana Champaign, College of Engineering …, 1928.

[66] Y.M. Amran, R. Alyousef, R.S. Rashid, H. Alabduljabbar, C.-C. Hung, Properties and applications of FRP in strengthening RC structures: A review, Structures, Elsevier, 2018, pp. 208-238.

[67] M.H. Khaneghahi, E.P. Najafabadi, M. Bazli, A.V. Oskouei, X.-L. Zhao, The effect of elevated temperatures on the compressive section capacity of pultruded GFRP profiles, Construction and Building Materials 249 (2020) 118725.

[68] H. Ashrafi, M. Bazli, A. Jafari, T. Ozbakkaloglu, Tensile properties of GFRP laminates after exposure to elevated temperatures: Effect of fiber configuration, sample thickness, and time of exposure, Composite Structures 238 (2020) 111971.

[69] E.P. Najafabadi, M. Bazli, H. Ashrafi, A.V. Oskouei, Effect of applied stress and bar characteristics on the short-term creep behavior of FRP bars, Construction and Building Materials 171 (2018) 960-968.

[70] A.V. Oskouei, A. Jafari, M. Bazli, R. Ghahri, Effect of different retrofitting techniques on in-plane behavior of masonry wallettes, Construction and Building Materials 169 (2018) 578-590.

[71] A.V. Oskouei, M.P. Kivi, H. Araghi, M. Bazli, Experimental study of the punching behavior of GFRP reinforced lightweight concrete footing, Materials and Structures 50(6) (2017) 256.

[72] A. Jafari, A.V. Oskouei, M. Bazli, R. Ghahri, Effect of the FRP sheet's arrays and NSM FRP bars on in-plane behavior of URM walls, Journal of Building Engineering 20 (2018) 679-695.

[73] M.N.S. Hadi, Q.S. Khan, M.N. Sheikh, Axial and flexural behavior of unreinforced and FRP bar reinforced circular concrete filled FRP tube columns, Construction and Building Materials 122 (2016) 43-53.

[74] A.D. Mai, M.N. Sheikh, M.N.S. Hadi, Investigation on the behaviour of partial wrapping in comparison with full wrapping of square RC columns under different loading conditions, Construction and Building Materials 168 (2018) 153-168.

[75] A. Kashi, A.A. Ramezanianpour, F. Moodi, Durability evaluation of retrofitted corroded reinforced concrete columns with FRP sheets in marine environmental conditions, Construction and Building Materials 151 (2017) 520-533.

[76] A.N. Ababneh, R.Z. Al-Rousan, I.M. Ghaith, Experimental study on anchoring of FRP-strengthened concrete beams, Structures, Elsevier, 2020, pp. 26-33.

[77] H. Zhang, M.N.S. Hadi, Geogrid-confined pervious geopolymer concrete piles with FRP-PVC-confined concrete core: Analytical models, Structures 23 (2020) 731-738.

[78] F. Micelli, R. Mazzotta, M. Leone, M.A. Aiello, Review Study on the Durability of FRP-Confined Concrete, Journal of Composites for Construction 19(3) (2015) 04014056.

[79] H. Zhang, M.N. Hadi, Geogrid-confined pervious geopolymer concrete piles with FRP-PVC-confined concrete core: Concept and behaviour, Construction and Building Materials 211 (2019) 12-25.

[80] X. Yang, W.-Y. Gao, J.-G. Dai, Z.-D. Lu, Shear strengthening of RC beams with FRP grid-reinforced ECC matrix, Composite Structures (2020) 112120.

[81] Y. Wang, G. Chen, B. Wan, G. Cai, Y. Zhang, Behavior of circular ice-filled self-luminous FRP tubular stub columns under axial compression, Construction and Building Materials 232 (2020) 117287.

[82] M. Lindner, K. Vanselow, S. Gelbrich, L. Kroll, Fibre-reinforced polymer stirrup for reinforcing concrete structures.

[83] M. Tomii, Lateral Load Capacity of Reinforced Concrete Short Columns Confined by Stell Tube-Experimental Results of Preliminary Research, Proceedings of the International Specialty Confernce on Concrete-Filled Steel Tubular Structures (1985) 19-26.

[84] M. Tomii, K. Sakino, Y. Xiao, K. Watanabe, Earthquake resisting hysteretic behavior of reinforced concrete short columns confined by steel tube, Proceedings of the International Speciality Conference on Concrete Filled Steel Tubular Structures, Harbin, China, 1985, pp. 119-25.

[85] Y. Xiao, Applications of FRP composites in concrete columns, Advances in Structural Engineering 7(4) (2004) 335-343.

[86] A. Raza, A. ur Rehman, B. Masood, I. Hussain, Finite element modelling and theoretical predictions of FRP-reinforced concrete columns confined with various FRP-tubes, Structures, Elsevier, 2020, pp. 626-638.

[87] T. Ozbakkaloglu, T. Vincent, Axial compressive behavior of circular high-strength concrete-filled FRP tubes, Journal of composites for construction 18(2) (2014) 04013037.

[88] Y.L. Li, X.L. Zhao, R.K. Singh Raman, Mechanical properties of seawater and sea sand concrete-filled FRP tubes in artificial seawater, Construction and Building Materials 191 (2018) 977-993.

[89] A. Parghi, M.S. Alam, A review on the application of sprayed-FRP composites for strengthening of concrete and masonry structures in the construction sector, Composite Structures 187 (2018) 518-534.

[90] C.E. Kurt, Concrete filled structural plastic columns, Journal of the Structural Division 104(ASCE 13478 Proceeding) (1978).

[91] R.K. Watkins, Buried pipe encased in concrete, Pipeline Engineering and Construction: What's on the Horizon?2004, pp. 1-10.

[92] J. Xue, H. Li, L. Zhai, X. Ke, W. Zheng, B. Men, Analysis on influence parameters and mechanical behaviors of embedded PVC pipe confined with reinforced high-strength concrete columns under cyclic reversed loading, Xi'an University of Arch. & Tech.(natural science edition) 48(1) (2016).

[93] W.O. Oyawa, N.K. Gathimba, N. Geoffrey, Innovative composite concrete filled plastic tubes in compression, 2015 World Congress on Advances in Structural Engineering and Mechanics (ASEM15), 2015, pp. 1-15.

[94] J.-Y. Wang, Q.-B. Yang, Investigation on compressive behaviors of thermoplastic pipe confined concrete, Construction and Building Materials 35 (2012) 578-585.

[95] N.A. Abdulla, Concrete filled PVC tube: A review, Construction and Building Materials 156 (2017) 321-329.

[96] H. Toutanji, M. Saafi, Durability studies on concrete columns encased in PVC–FRP composite tubes, Composite structures 54(1) (2001) 27-35.

[97] J. Wang, Q. Yang, Experimental study on mechanical properties of concrete confined with plastic pipe, ACI Materials Journal 107(2) (2010) 132.

[98] R. Nowack, O.I. Otto, E.W. Braun, 60 Jahre Erfahrungen mit Rohrleitungen aus weichmacherfreiem Polyvinylchlorid (PVC-U), KRV Nachrichten (1995) 1-95.

[99] P.K. Gupta, V.K. Verma, Study of concrete-filled unplasticized poly-vinyl chloride tubes in marine environment, Proceedings of the Institution of Mechanical Engineers, Part M: Journal of Engineering for the Maritime Environment 230(2) (2016) 229-240.

[100] I. Jakubowicz, N. Yarahmadi, T. Gevert, Effects of accelerated and natural ageing on plasticized polyvinyl chloride (PVC), Polymer degradation and stability 66(3) (1999) 415-421.

[101] A.S. Saadoon, Experimental and Theoretical Investigation of PVC Concrete composite Columns, University of Basrah (2010).

[102] H. Zhang, M.N.S. Hadi, Geogrid-confined pervious geopolymer concrete piles with FRP-PVC-confined concrete core: Concept and behaviour, Construction and Building Materials 211 (2019) 12-25.

[103] G. Zong, J. Hao, X. Hao, Y. Fang, Y. Song, H. Wang, R. Ou, Q. Wang, Enhancing the flame retardancy and mechanical properties of veneered wood flour/polyvinyl chloride composites, Polymer Composites 41(3) (2020) 848-857.

[104] H. Toutanji, M. Saafi, Stress-strain behavior of concrete columns confined with hybrid composite materials, Materials and structures 35(6) (2002) 338.

[105] M. Marzouck, K. Sennah, Concrete-filled PVC tubes as compression members, Composite Materials in Concrete Construction: Proceedings of the International Seminar held at the University of Dundee, Scotland, UK on 5–6 September 2002, Thomas Telford Publishing, 2002, pp. 31-37.

[106] F. Yu, D. Niu, Stress-strain model of PVC-FRP confined concrete column subjected to axial compression, Academic Journals, 2010.

[107] Y. Fang, F. Yu, Y. Guan, Z. Wang, C. Feng, D. Li, A model for predicting the stress–strain relation of PVC-CFRP confined concrete stub columns under axial compression, Structures, Elsevier, 2020, pp. 259-270.

[108] S.-F. Jiang, S.-L. Ma, C.-L. Liang, Z.-Q. Wu, Axial Behavior of CFRP-PVC-Confined Concrete Stubs, Advanced Science Letters 9(1) (2012) 197-203.

[109] A.M. Mammen, M. Antony, Experimental Study On Frp-Pvc Confined Circular Columns, International Research Journal of Engineering and Technology (IRJET) 4(5) (2017).

[110] Y. Yu, Z. Wu, H. Guan, Experimental Study On The Axial Compression Of GRP-Concrete-PVC Tube Composite Column, IOP Conference Series: Earth and Environmental Science, IOP Publishing, 2019, p. 042013.

[111] H. Toutanji, Design equations for concrete columns confined with hybrid composite materials, Advanced Composite Materials 10(2-3) (2001) 127-138.

[112] A.M. Woldemariam, W.O. Oyawa, T. Nyomboi, The Behavior of Concrete-Filled Single and Double-Skin uPVC Tubular Columns Under Axial Compression Loads, The Open Construction & Building Technology Journal 13(1) (2019).

[113] F. Hong-bo, Mechanics behavior of FRP-PVC concrete column [j], Low Temperature Architecture Technology 5 (2009).

[114] Y. Qi-bin, New progress on the study of a new type of hybrid columns based on FRP and PVC [J], Journal of Changchun Institute of Technology (Natural Sciences Edition) 1 (2011).

[115] M. Fakharifar, G. Chen, FRP-confined concrete filled PVC tubes: A new design concept for ductile column construction in seismic regions, Construction and Building Materials 130 (2017) 1-10.

[116] F. Yu, G. Xu, D. Niu, A. Cheng, P. Wu, Z. Kong, Experimental study on PVC-CFRP confined concrete columns under low cyclic loading, Construction and Building Materials 177 (2018) 287-302.

[117] M. Bazli, A. Jafari, H. Ashrafi, X.-L. Zhao, Y. Bai, R.S. Raman, Effects of UV radiation, moisture and elevated temperature on mechanical properties of GFRP pultruded profiles, Construction and Building Materials 231 (2020) 117137.

[118] M. Bazli, H. Ashrafi, A.V. Oskouei, Effect of harsh environments on mechanical properties of GFRP pultruded profiles, Composites Part B: Engineering 99 (2016) 203-215.

[119] F. Micelli, A. Nanni, Durability of FRP rods for concrete structures, Construction and Building materials 18(7) (2004) 491-503.

[120] D. Lau, Q. Qiu, A. Zhou, C.L. Chow, Long term performance and fire safety aspect of FRP composites used in building structures, Construction and building materials 126 (2016) 573-585.

[121] G. Wu, X. Wang, Z. Wu, Z. Dong, G. Zhang, Durability of basalt fibers and composites in corrosive environments, Journal of Composite Materials 49(7) (2015) 873-887.

[122] M. Bazli, H. Ashrafi, A. Jafari, X.-L. Zhao, R. Raman, Y. Bai, Effect of fibers configuration and thickness on tensile behavior of GFRP laminates exposed to harsh environment, Polymers 11(9) (2019) 1401.

[123] H. Ashrafi, M. Bazli, E.P. Najafabadi, A.V. Oskouei, The effect of mechanical and thermal properties of FRP bars on their tensile performance under elevated temperatures, Construction and Building Materials 157 (2017) 1001-1010.

[124] H. Ashrafi, M. Bazli, A. Vatani Oskouei, L. Bazli, Effect of sequential exposure to UV radiation and water vapor condensation and extreme temperatures on the mechanical properties of GFRP bars, Journal of Composites for Construction 22(1) (2018) 04017047.

[125] M. Bazli, H. Ashrafi, A. Jafari, X.-L. Zhao, H. Gholipour, A.V. Oskouei, Effect of thickness and reinforcement configuration on flexural and impact behaviour of GFRP laminates after exposure to elevated temperatures, Composites Part B: Engineering 157 (2019) 76-99.

[126] A.V. Oskouei, M. Bazli, H. Ashrafi, M. Imani, Flexural and web crippling properties of GFRP pultruded profiles subjected to wetting and drying cycles in different sea water conditions, Polymer Testing 69 (2018) 417-430.

[127] A. Jafari, M. Bazli, H. Ashrafi, A.V. Oskouei, S. Azhari, X.-L. Zhao, H. Gholipour, Effect of fibers configuration and thickness on tensile behavior of GFRP laminates subjected to elevated temperatures, Construction and Building Materials 202 (2019) 189-207.

[128] M. Bazli, X.L. Zhao, R.S. Raman, Y. Bai, S. Al-Saadi, Bond strength durability between FRP tubes and seawater sea sand concrete under sea water condition, Asia-Pacific Conference on FRP in Structures 2019, APFIS Conference Series, 2019.

[129] H.A. Toutanji, L. Zhao, G.J. Isaacs, Durability studies on concrete columns confined with advanced fibre composites, International Journal of materials and product technology 28(1-2) (2007) 8-28.